POLITECNICO DI TORINO
Dottorato di Ricerca in Energetica
XIV Ciclo

Paolo Ferracin

TESI DI DOTTORATO

MECHANICAL AND MAGNETIC ANALYSIS OF THE LARGE HADRON COLLIDER MAIN DIPOLE

Coordinator: Prof. Bruno Panella

Tutor: Prof. Giovanni Del Tin

Supervisors: Dr. Walter Scandale

Dr. Ezio Todesco

March 2002

Contents

Chapter 1

Introduction

1.1 Particle accelerators

Particle accelerators [1] are machines that accelerate charged elementary particles to high kinetic energy. Particles are usually electrons or positrons or ionised atoms. A beam of such particles is then smashed against other particles. The other particles may be stationary atomic nuclei in a fixed target or fast moving particles in another beam who is brought into a head-on collision with the first beam. Collisions with very high energy beams correspond to very high temperatures in the interactions. The study of matter in these extreme conditions can be related to the conditions prevailing in the Universe in the first moments after the so-called "Big Bang".

In circular accelerators the energy of the beam is increased into closed circular. Since the particles travel in a straight line if no external forces are acting on them, in these machines a magnetic field imparts a Lorentz force to them inducing a curved path. The amount of curvature of the orbit depends on the strength of the magnetic field and on the energy of the particle: the greater the magnetic field, the greater the curvature; the greater the energy, the less the curvature.

As particle energy and momentum increase with every pass around the track, the strength of the magnetic field is gradually augmented. The increase of energy and magnetic field are synchronised, ensuring that the particles circulate in the same path every time: we say that the field "ramps up" with particle energy increase. Circular accelerator producing a synchronised increase of energy and magnetic field are called synchrotrons.

1.2 Dipole magnets for accelerators

Dipole magnets for accelerators [1] fulfil the requirement of generating the magnetic field necessary to force the beam into a circular orbits. They have two poles producing field lines in the aperture of the magnet (where the beam passes) perpendicular to the plane of the particle beam orbit. They are in general electro-magnets, with

magnetic fields generated by the flow of electric current in the wire winding of their coils. The coils are encased in a ferromagnetic yoke which provides a return path to close the field lines and to increase the field in the aperture. Depending on the field strength several designs are possible :

- low field (up to 2 T) iron-dominated magnets;

- high-field rectangular magnets;

- high-field round magnets;

- very high-field magnets.

In the iron-dominated magnets the peak magnetic field is limited by the iron saturation at about 2 T. The field shape depends principally on the shape of the iron yoke, which determines the "good field" region where the beam can travel safely. In most of the cases, such magnets are resistive, although there are examples of iron-dominated superconducting magnets, where the yoke can remain either at ambient or at cryogenic temperature.

For fields above 2 T the magnets should be superconducting and the coil should produce the additional magnetic flux. The coil becomes larger and the placement of the conductors determines the shape and the quality of the field. Laminated steel spacers called collars are in general positioned around the coils and inside the yoke in order to confine the conductors and keep them in place. In many cases, the yoke itself is used to support the coils. These magnets, called high-field magnets, may be rectangular or circular. In the high-field rectangular magnets [2], the conductors are placed above and below the aperture and the coil features a rectangular shape. In the round magnet design, the coil is placed in a cylindrical shell around the magnet bore. This coil configuration is called the $\cos\theta$ configuration, since the current distribution in the cylindrical shell approximately varies as the cosine of the angle from the mid-plane. For a colliding beam accelerator in which counter rotating beams collide, a magnet design option is the "two-in-one" $\cos\theta$ design, where the two sets of coils for the two beams are combined in a single iron yoke [3]. The $\cos\theta$ configuration is predominantly used for magnet in the 3 to 10 T range with NbTi superconductors and up to 13 T with Nb_3Sn superconductors. Dipoles with the $\cos\theta$ configuration and NbTi superconductors have been built for the following accelerators:

- Tevatron at Fermilab, Chicago, USA: 4.4 T at 4.6 K;

- HERA at DESY, Hamburg, Germany: 4.7 T at 4.6 K;

- RHIC at Brookhaven, New York, USA: 3.5 T at 4.6 K;

- SSC (project cancelled in October 1993) at SSCL, Texas, USA: 6.6 T at 4.4 K;

- LHC (completion date 2006) at CERN, Geneva, Switzerland: 8.3 T at 1.9 K.

For very high-field magnets, i.e. for field higher than 10 T, two new designs have been proposed: the common coil design [4] and the block magnet design [5]. Both use the two-in-one configuration with Nb_3Sn superconductors.

1.3   Definition of the problem

In the superconducting magnets the conductors are placed close to the bore in order to reach an high magnetic field in the region where the beam passes. The main consequence of this feature, compared to the resistive magnets where the conductors are distant and the iron yoke extends towards the beam tube, is that the shape and the quality of the magnetic field strongly depends on the position of the conductors. In a circular accelerator, in order to guarantee a beam stable during the operation, the magnetic field errors must be controlled at levels of the order of less than 10^{-4} of the main field. This means that the position of the conductors must be controlled with a precision greater than 0.1 mm.

Another important issue of the superconducting magnets is that the conductors must be constrained during the ramp-up of the magnetic field. In fact, the high magnetic field provokes strong Lorentz forces. These forces act on the conductors and may determine dangerous conductor movements. If these movements produce a release of energy due to friction, the consequent warm-up of the cables may cause the transition to the normal state of the conductors and the so-called quench of the magnet, inducing a rapid shut-off of the dipolar field. For this reason the coil is assembled inside a mechanical structure, composed by the collars and the yoke, which compresses the coil and confines it in a rigid cavity. The value of the compression stress exerted on the coil by the mechanical components is carefully chosen so that the conductors are maintained under stress in the nominal conditions. To obtain this result, it must be taken into account the stress redistribution that occurs in each of the three phases preceding the nominal conditions, that is the assembly, the cool-down and the ramp-up. In particular the cool-down determines a significant modification of the stresses inside the magnet because of the different thermal contraction of the components.

The importance of conductor position for an optimised field quality and of coil stresses for quench performances are strongly linked. In fact, the stresses inside the magnet generate mechanical deformations of the components which surround the coil and define its shape. These deformations, and their variations during the assembly, the cool-down and the ramp-up, affect the coil geometry and the quality of the field. Thus, the mechanical and the magnetic behaviour in a superconducting magnet are correlated.

A superconducting magnet is therefore a complex mechanical-magnetic system, where both the stresses and the geometry of the coil must be precisely controlled in order to get, in the operational conditions, the nominal stresses and the design coil shape.

1.4   Aim of the work and tools

The aim of this work is the study of the mechanical and magnetic behaviour of the main superconducting dipole for the Large Hadron Collider, during the assembly and the cool-down phases. The mechanical analysis consists of the study of the stresses on the coil and on the collars, in order to check if the compression of the coil in cold conditions fits the target values.

The magnetic analysis is aimed to evaluate the effect on magnetic field shape of mechanical deformations. We study the magnetic measurements performed on the magnets, disentangling the contribution of the coil strains on magnetic errors. Moreover, possible corrective actions for the field errors are analysed, based on the shape modification of the mechanical structure surrounding the coil.

The analysis has been performed by means of:

- measurements of the thermo-mechanical properties of the coil;

- analysis of the stress measurements performed on the dipole at ambient and at cryogenic temperature;

- analysis of the magnetic measurements performed on the dipole at ambient and at cryogenic temperature;

- modeling of the behaviour by the magnet with a mechanical finite element model implemented in the code ANSYS^{TM} [6] and by a magneto-static model implemented in the code ROXIE [7];

1.5   Contents of the thesis

The knowledge of the properties of the superconducting coil is essential for the comprehension and for the modeling of the dipole mechanics. In particular, the elastic modulus and the integral thermal contraction coefficient play a fundamental role. We performed measurements of the coil elastic modulus at ambient temperature and at 77 K and we evaluated its thermal shrinkage. The coil of LHC dipole features a well-known non-linear stress-strain curve [8, 9, 10], with a different response to loads between the loading and the unloading phase (mechanical hysteresis). Our experimental procedure was focused on measurements of the stress-strain curves along different loading and unloading paths, to obtain the data necessary to a complete modeling of the elasticity of the coil. Then, we evaluated the coil integrated thermal contraction coefficient from 293 K to 77 K. We explored the ambiguities in its definition and we explained the rather large variation of thermal contraction values reported in the literature [11, 12, 13, 14, 15, 16].

The measured thermo-mechanical properties of the coil have been implemented in a finite element model of the dipole, used for the analysis of stresses and deformations [17]. We validated the modeling of the interfaces between the dipole

components and of the coil non-linear mechanical behaviour. The reliability of the FEM concerning these two critical aspects was never checked before. The validation was performed with a comparison between the results of the simulations and optical measurements of the conductor displacements.

The FEM was used to study stresses and deformations of the dipole at 293 K. We applied a new approach based on the implementation in the model of equivalent mechanical properties of the coil. These equivalent properties take into account both the measured mechanical properties and the stress path followed by the coil during the assembly. On the other hand, the properties implemented in the previous models were only related to the operational conditions and did not consider the coil stress history [18]. With this new approach, the deformations at ambient temperature of the dipole components, and in particular of the coil, were studied and the results of the numerical computations were compared to experimental measurements.

The same approach, i.e. the definition of equivalent mechanical properties, has been used to simulate with the FEM the stress variations during the cool-down. This method, used here for the first time in the literature, was implemented since the standard finite element model did not recover the significant coil stress losses measured in the dipole from 293 K to 1.9 K [19]. The effect of the cool-down was modelled also by an analytical model and we compared the results with the experimental measurements.

Then, we focused our analysis on the magnetic behaviour of the dipole. The study consists of simulations with two models: the finite element model, to compute the coil shape in the different phases preceding the ramp-up, and a magneto-static model, to evaluate the magnetic field generated by these different coil shapes. By this coupled mechanical-magnetic model the effect of the tolerances of fabrication on the magnetic field was analysed. Moreover, a study of the discrepancy of the measured field quality with respect to the expected values was carried out. To cure these discrepancies, we proposed a corrective action based on the modification of spacers inserted between the coil and the collars. We evaluated the effect of these spacers by the new mechanical modeling with the equivalent properties. A comparison with data obtained by previous models, which neglect the mechanical deformations [20], and with the measurements performed on a dedicated experiment was carried out.

Finally, we concluded the magnetic analysis with the study of the effect of the cool-down on the generated field, with a comparison between measurements and numerical computations.

1.6 Structure of the thesis

The thesis is composed by nine Chapters and six Appendixes. In Chapter 2 we present the main parameters of the Large Hadron Collider and of its superconducting main dipole. The components of the dipole are described in detail and their mechanical and magnetic functions are explained. Chapter 3 deals with mea-

surements that we have performed to evaluate the elastic modulus of coil and its thermal contraction coefficient. The calibration of the experimental apparatus is given in Appendix A and further considerations on the thermal shrinkage of the coil are presented in Appendix B. A description of the finite element model of the dipole and its validation with the optical measurements is given in Chapter 4. In Chapter 5 we study stresses and deformations inside the magnet at 293 K, we analyse the stress measurements (given in Appendix C) and we present the results of the finite element model. The variation of the stresses during the cool-down from ambient to cryogenic temperature is studied in Chapter 6. Chapter 7 and Chapter 8 are focused on the magnetic behaviour of the dipole, at ambient and after cool-down respectively. All the magnetic measurements are given in Appendix D, Appendix E and Appendix F.

Chapter 2

The Large Hadron Collider and its main dipole

2.1   The Large Hadron Collider

The Large Hadron Collider [3] is a circular accelerator under construction at CERN (European Laboratory for Particle Physics): the project has been approved by the CERN Council in December 1994 and it will be completed in 2006.

The machine will replace the LEP collider (Large Electron Positron Collider), inside the 27 km underground circular tunnel in the Geneva area, and will provide proton-proton collisions with a centre-of-mass energy of 14 TeV.

The particle beam will be pre-accelerated by three different machines (LINAC, PS and SPS) to 450 GeV and sent to the LHC. This phase is called the *injection*. The beam energy will be then increased up to the 7 TeV in the LHC itself. This phase is called the *acceleration*. The collisions will occur in four interaction points where four experiments (ALICE, CMS, LHC-b and ATLAS) are placed. This phase is called the *interaction*.

Inside the LHC, superconducting magnets aligned with a precision of a few tenth of mm are used to bend and focus the particle trajectories them [21]. Namely:

- dipoles create the main vertical magnetic field, perpendicular to the particle direction, used to deflect particle motions to circular trajectories;

- quadrupoles produce a field that is null in the centre of the vacuum chamber and linearly dependent from the distance to the centre, whose purpose is to focus the beam.

In the LHC tunnel, 1232 main dipoles and 386 main quadrupoles will be installed.

7

2.2   The superconducting main dipole

A vertical magnetic field of $8.3\,\text{T}$ is necessary to deflect a proton beam accelerated in the LHC tunnel to an energy of $7\,\text{TeV}$. This level of magnetic field requires the use of superconducting magnet technology. There are three large accelerators in operation based on superconducting magnets: the Tevatron (Fermilab, USA), the HERA (DESY, Germany) and the RHIC (Brookhaven, USA). They all make use of classical NbTi superconductors cooled with liquid helium at a temperature slightly above $4.2\,\text{K}$, and their operational fields are $4.4\,\text{T}$ for the Tevatron, $4.7\,\text{T}$ for HERA and $3.5\,\text{T}$ for RHIC. For the LHC it is mandatory to push the field significantly higher, still retaining the well-proven fabrication methods of cables and coils made of NbTi superconductors. The only way of obtaining fields of $8.3\,\text{T}$ is to cool the magnets at a temperature of $1.9\,\text{K}$. In fact, at this lower temperature, the critical field and current of the superconducting cables are considerably increased.

Below $2.17\,\text{K}$, helium takes the so-called superfluid state, with much lower viscosity and much greater heat transmission capacity than liquid helium. On the other hand, the enthalpy of all metallic parts and in particular of the superconducting cables is reduced by almost an order of magnitude between $4.2\,\text{K}$ and $1.8\,\text{K}$, with a consequent faster temperature rise for a given deposit of energy. This feature calls for particular care in limiting conductor motion. It should be noted that the electro-magnetic forces on the conductor increase with B^2 and so does the stored electro-magnetic energy, calling for a much stronger force-retaining structure than in the previous projects.

The main parameters of the dipole are listed in Tab. 2.1, while Fig. 2.1 shows the dipole mass and Fig. 2.2 its transverse cross-section.

Proton-proton colliders require two separate beam channels with fields equal in strength but opposite in directions. For the LHC, the compact "two-in-one" design is adopted, whereby the two beam channels (also called apertures) and their corresponding sets of coils are inserted in a unique structure $15\,\text{m}$ long (see Fig. 2.1) and in a single cryostat (see Fig. 2.2). In this arrangement a significant space saving and a cost reduction of $30\,\%$ can be made with respect to two separate structures.

The dipole is composed by two superconducting coils which generate the magnetic field inside the two beam pipes. The coil are surrounded by a containment structure that consists of coil clamping elements, the collars, the iron yoke and the shrinking cylinder, which all contribute to producing the necessary azimuthal precompression in the coils and to prevent tensile stresses arising in the coils under the action of the electro-magnetic forces. In operation, the assembly inside the shrinking cylinder, the so-called *cold mass*, is kept at $1.9\,\text{K}$. The cold mass is installed inside a cryostat whose main components are a radiation shield at $5\,\text{K}$, a thermal screen at $70\,\text{K}$, and the outer cylindrical wall of the vacuum vessel. All parts between the beam vacuum chamber walls and shrinking cylinder are immersed in superfluid helium at atmospheric pressure and cooled by means of a heat-exchanger tube, in which two-phase low-pressure helium is circulated and acts as a heat sink.
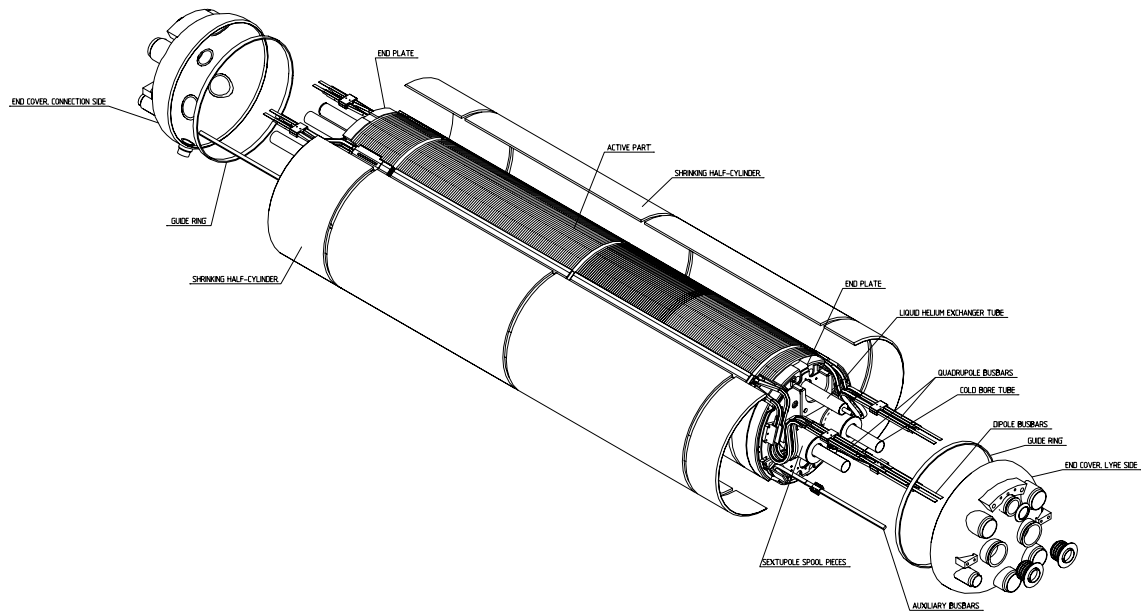
Figure 2.1: The dipole cold mass.
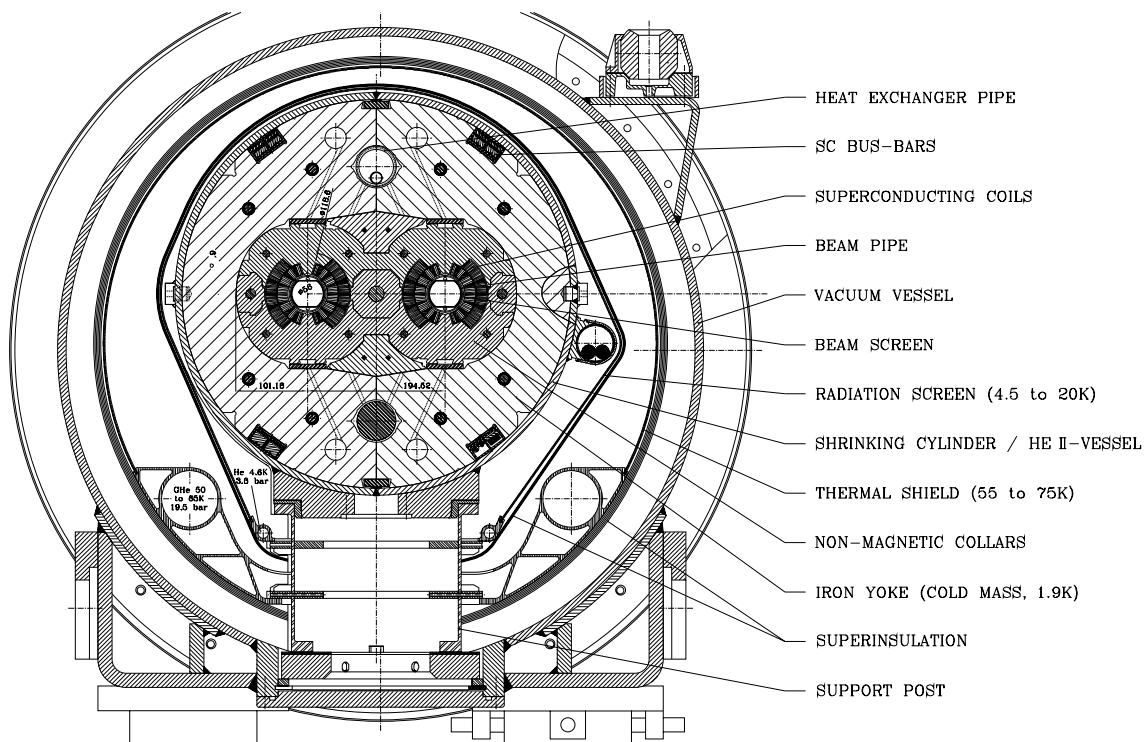
Figure 2.2: The dipole cryostat cross-section.

Table 2.1: Dipole parameters.

Operational field	(T)	8.3
Coil aperture	(mm)	56
Magnetic length	(mm)	14300
Current at injection ($B = 0.45\,\text{T}$)	(A)	740
Operating current	(A)	11800
Operating temperature	(K)	1.9
Coils (two-shells construction)		
Coil inner diameter	(mm)	56
Coil outer diameter (incl. insulation to ground)	(mm)	120.5
Coil length (incl. end pieces)	(mm)	14467
Thickness of perforated glass-epoxy	(mm)	0.5
Thickness of insulation to ground	(mm)	0.75
Structure		
Distance between aperture axes (at $293\,\text{K}$)	(mm)	194
Collar height	(mm)	192
Collar width	(mm)	396
Yoke outer diameter	(mm)	550
Shrinking cylinder outer diameter	(mm)	570
Length of active part (incl. end plates)	(mm)	14603
Overall length of cold mass	(mm)	15180
Mass of cold mass	(t)	23.8
Outer diameter of cryostat	(mm)	914
Overall mass of cryomagnet	(t)	27.5
Other characteristics		
Stored energy for both channels ($500\,\text{kJ/m}$)	(MJ)	7.1
Resultant of e.m. forces in the first coil quadrant: $\sum F_x$	[MN/m]	1.7
$\sum F_y$ (inner layer)	(MN/m)	-0.14
$\sum F_y$ (outer layer)	(MN/m)	-0.60
Axial e.m. force on magnet ends (for both channels)	(MN)	0.50

The cold mass is bent to a $2804\,\text{m}$ radius of curvature, with a horizontal sagitta of 9.7 mm in the centre, to match the beam paths.

We start now describing in detail the main components of the cold mass.

2.2.1   The cable

The transverse cross-section of the coils for the 56 mm aperture dipole magnet shows two layers of different cables of the Rutherford type (see Fig. 2.3), where strands composed by NbTi filament in a copper matrix are twisted and compressed into a

flat two-layer cable. The basic parameters of the two cables are given in Tab. 2.2. The cable used in the inner layer has 28 strands and the cable of the outer layer 36 strands. The NbTi filament size is of $7\,\mu$m for the inner layer strand and $6\,\mu$m for the outer layer strand.
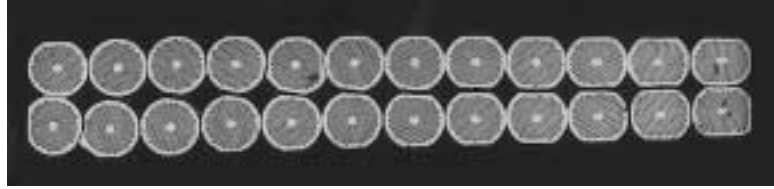
Figure 2.3: Cross-section of Rutherford type cable.
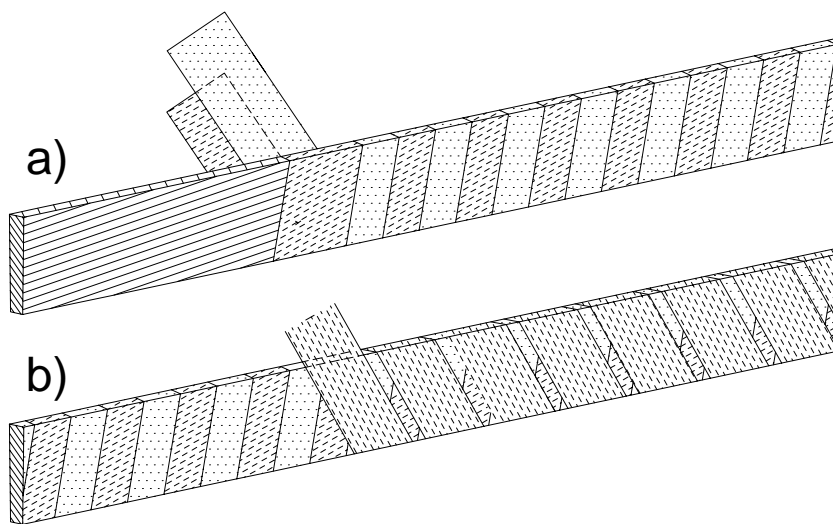
Figure 2.4: The cable insulation.

Cables have a trapezoidal shape, with angles between bases and oblique sides of 1.24 degrees for the inner layer and 0.90 degrees for the outer layer. These angles, called "keystoning" angles, are used to better obtain the arc shape of the coil.

During operation, the primary sources of heat to the coils are the lost particles and the synchrotron radiation. An additional dynamic heat load results from losses during magnet ramping. This heat increases the superconductor temperature, which reduces the magnet operating margin. Particular care has therefore to be taken to provide a cable insulation which not only withstands the voltage between turns but is also sufficiently porous to let the superfluid helium carry away the heat. The insulation must also be robust, in order not to break during winding and curing.

Table 2.2: Strand and cable characteristics.

	Inner layer	Outer layer
Strand		
Strand diameter (mm)	1.065	0.825
Copper to superconductor ratio	1.6	1.9
Filament size (mm)	0.007	0.006
Number of filaments	8900	6500
RRR	≥ 70	≥ 70
Twist pitch (after cabling) (mm)	25	25
Critical current (A) 10 T, 1.9 K	≥ 515	
9 T, 1.9 K		≥ 380
Cable		
Number of strands	28	36
Cable dimension: thin edge (mm)	1.736	1.362
thick edge (mm)	2.064	1.598
width (mm)	15.1	15.1
Transposition pitch (mm)	110	100
Keystone angle (degree)	1.24	0.90
Critical current (A) 10 T, 1.9 K	≥ 13750	
9 T, 1.9 K		≥ 12950
Cable insulation		
Thickness of 1st tape (50% overlapped) (mm)	0.025	0.025
Width of 1st tape (50% overlapped) (mm)	11	11
Thickness of 2nd tape (50% overlapped) (mm)	0.025	0.025
Width of 2nd tape (50% overlapped) (mm)	11	11
Thickness of 3rd tape (2 mm spacing) (mm)	0.069	0.069
Width of 3rd tape (2 mm spacing) (mm)	9	9
Insulated cable dimension: thin edge (mm)	1.973	1.620
thick edge (mm)	2.307	1.860
width (mm)	15.4	15.4

The basic cable insulation, which must safely withstand a turn-to-turn test voltage of 75 V, is composed of two polyimide layers wrapped around the cable, with 50 % overlapping (see Fig. 2.4 a), and another adhesive polyimide tape wrapped onto the cable and spaced by 2 mm (see Fig. 2.4 b). The resulting gap makes the coil porous by setting up channels for superfluid helium, without affecting the mechanical support between turns.

After winding, the adhesive is cured by heating each coil layer in a curing mould, which at the same time gives the final shape and size to the coil.

2.2.2 The superconducting coil

A charged particle q moving with velocity v through a magnetic field B is acted by a force called the Lorentz force, given by

$$\vec{F} = q\vec{v} \wedge \vec{B} \tag{2.1}$$

which is perpendicular to the direction of the magnetic field and of the particle motion. The Lorentz force on beam particles keeps them in the desired orbits through the accelerator.
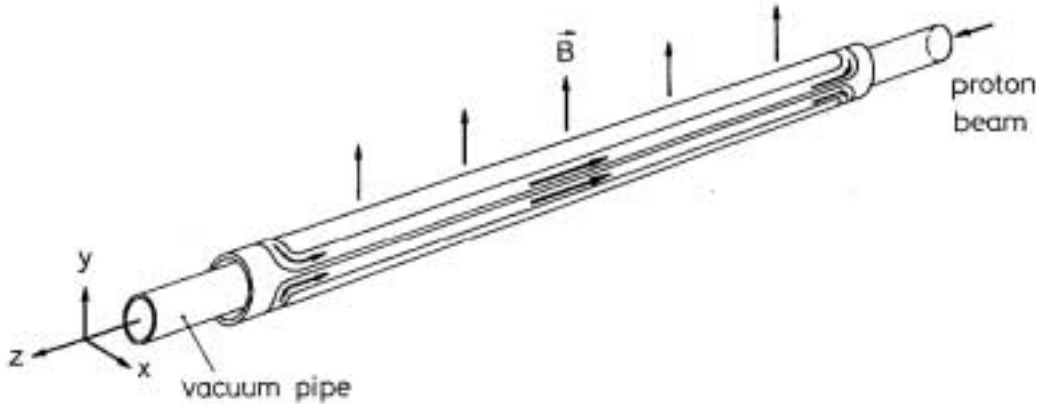
Figure 2.5: Schematic view of the superconducting dipole coil.

The coil of a dipole is designed to generate in the vacuum pipe a uniform vertical magnetic field, perpendicular to the proton beam, in order to steer the particles in a circular orbit. A schematic view of a superconducting coil is given in Fig. 2.5: the current conductors run parallel to the particle beam over the longest part of the magnet except for the parts on the extremities, so-called *coil heads*, where the conductors make their turn. The heads produce field perturbation; however their length is small compared to the length of the straight section and thus the effect is minimal: in the LHC dipole the heads are about half a meter long, while the total length of the coil is 14.5 m.

The coil cross-section is shaped to make the best use of a superconducting cable and to produce a dipole field of the best possible homogeneity over the whole range of its operational excitation. The conductor distribution selected in the LHC dipole is shown in Fig. 2.6. Conductors are placed on two layers and distributed on six blocks for each quadrant.

Wedge-shaped copper spacers (*copper wedges*) are inserted between blocks of conductors to produce the desired field quality and to approximate a quasi-circular coil geometry, compensating for the insufficient keystoning of the cables. In the next Section we describe how this kind of conductor distribution generates a dipole field.
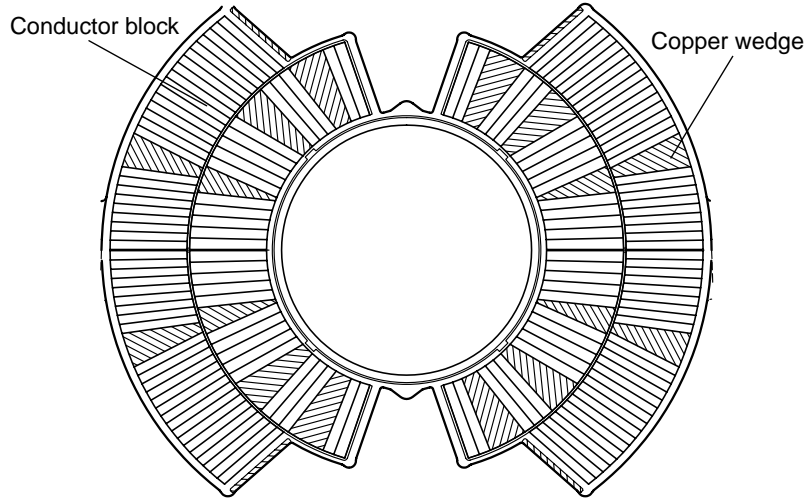
Figure 2.6: The superconducting dipole coil cross-section in the LHC dipole.

2.2.3   The magnetic field

It can be demonstrated [22] that if we consider the arrangement of current distribution represented in Fig. 2.7, where the currents, perpendicular to the sheet, are distributed as a function of the azimuthal angle θ with respect to the x axis, i.e

$$I(\theta) = I_0 \cos\theta, \tag{2.2}$$

the field obtained in the area between the two distribution is a pure and homogeneous dipole.
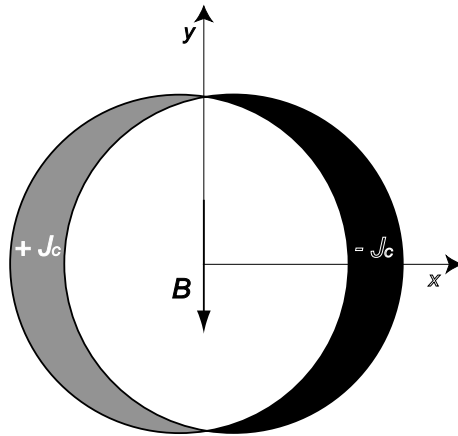
Figure 2.7: Generation of a pure dipole by a $\cos\theta$ current distribution.

Since we want to create inside the beam tube a dipole field as homogeneous as possible, the superconducting coil surrounding the tube should reproduce this current distribution, called $\cos\theta$ distribution. Such configuration is impossible to fabricate with a superconducting cable of constant cross-section as the Rutherford cable, but can be simulated with an arc geometry provided by the keystoning of the cables and by the copper wedges.

Indeed, the magnetic field generated by the superconducting coil is not a pure dipole, since it is affected also by higher order multipoles (quadrupole, sextupole, etc.). In order to express analytically the magnetic field inside the beam pipe, we remind that in a empty space, free of any currents and magnetised materials, the magnetic field fulfils the following two Maxwell equations

$$\vec{\nabla} \cdot \vec{B} = 0, \vec{\nabla} \times \vec{B} = 0. \tag{2.3}$$

In the central part of the dipole the conductors are parallel to the beam pipe. Under these circumstances one can consider the magnetic field essentially as two dimensional. If we define a complex magnetic field by the equation

$$\vec{B} = B_y + iB_x, \tag{2.4}$$

the Eqs. (2.3) are identical with the Cauchy-Riemann conditions and $\vec{B}$ can be expanded in a power series, obtaining

$$B_y(x,y) + iB_x(x,y) = B_1 \sum_{n=1}^{\infty} (b_n + ia_n) \left(\frac{x+iy}{R_{ref}} \right)^{n-1}, \tag{2.5}$$

where B_1 is the dipole field intensity and R_{ref} is the reference radius set to $17\,\text{mm}$ for the LHC dipole. The coordinate system (O, x, y, z) is defined so that the z axis is parallel to the beam line and the y is parallel to the dipole field. O is set at the center of the coil aperture. The coefficients b_1, b_2, ..., b_n are called the *normal multipole coefficients* and the coefficients a_1, a_2,..., a_n are called the *skew multipole coefficients*. The index $n = 1$ describes the dipolar field, $n = 2$ the quadrupolar field, $n = 3$ the sextupolar field, and so on.

We define the the normal (B_n) and skew (A_n) multipoles respectively as

$$B_2 = b_2 B_1, B_3 = b_3 B_1, ..., B_n = b_n B_1 \tag{2.6}$$

and

$$A_2 = a_2 B_1, A_3 = a_3 B_1, ..., a_n = a_n B_1. \tag{2.7}$$

A skew multipole A_n is given by a normal multipole B_n rotated by $\pi/(2m)$. A skew dipole, for instance, has an horizontal field. In Eq. (2.5), B_1 is in Tesla, and the dimensionless coefficients b_n and a_n are in so-called units, which are defined as 10^{-4} of the main field.

The multipolar components, describing the perturbations with respect to the ideal dipole field, can be classified in two groups. The odd normal multipoles b_1, b_3, b_5,... are called the *allowed multipoles*. They are generated by a current distribution which respects the dipole symmetry, i.e. even with respect to the x axis and odd with respect to the y axis. The even normal multipoles b_2, b_4, b_6,... and all the skew multipoles a_1, a_2, a_3,... are called the *unallowed multipoles*. They result in violation of the dipole symmetry: the even normal multipoles are due to asymmetries left-right and the skew multipoles to asymmetries top-bottom. In Tab. 2.3 we give the classification of the low order multipoles.

The allowed multipole can be tuned by changing the limiting angles of the two coil layers or the positions of the copper wedges. On the other hand, the minimisation of the unallowed multipoles, which are determined by manufacturing errors, requires great precision in the construction of the magnet components.

Table 2.3: Multipole classification.

Multipole		
b_2	unallowed	left-right asymmetry
a_2	unallowed	top-bottom asymmetry
b_3	allowed	dipole symmetry
a_3	unallowed	top-bottom asymmetry
b_4	unallowed	left-right asymmetry
a_4	unallowed	top-bottom asymmetry
b_5	allowed	dipole symmetry
a_5	unallowed	top-bottom asymmetry
b_6	unallowed	left-right asymmetry
a_6	unallowed	top-bottom asymmetry
b_7	allowed	dipole symmetry
a_7	unallowed	top-bottom asymmetry

2.2.4   The collars

The high currents and field in a typical $\cos\theta$ dipole produce very large Lorentz forces on the conductors. Considering the dipole cross-section, the Lorentz forces have two main components: an azimuthal component, which tends to squeeze the coil towards the mid-plane, and a radial component, which tends to bend the coil outwards, with a maximum displacement at the coil mid-plane.

These components may produce minute wire motions inside the coil. If the motions are purely elastic, no heat is dissipated and the coil remains superconducting. However, if the motions are frictional, the associated heat dissipation may be suf-
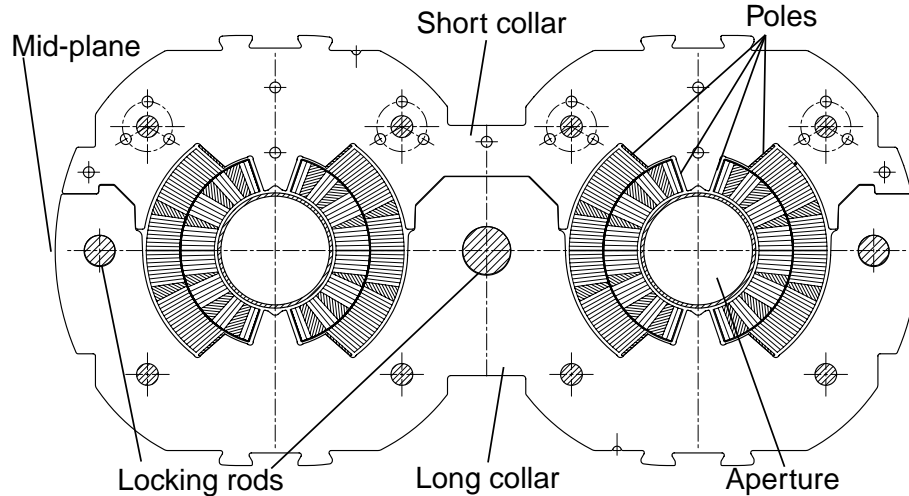
Figure 2.8: The collared coil.

ficient to produce a quench. The motions must therefore be prevented as much as possible by providing a rigid support to the coil: the collars (see Fig. 2.8).

The collars confine radially the coil inside a rigid cavity hence counteracting the the radial component of the Lorentz forces. Moreover, since the azimuthal component compresses the coil towards the mid-plane, at high field the coil turns close to the poles tend to move away from the collar poles (see Fig. 2.8). To prevent this phenomenon, the collars are assembled in order to produce an azimuthal pre-compression, called *pre-stress*, on the coils. The rule followed during assembly is to apply an azimuthal pre-stress to the collared coil so that the coil does not lose compression at the pole at full magnet current. Therefore, the coil pre-stress applied at room temperature by the collar must be sufficient to compensate for:

- insulation creep following the collaring procedure;

- differential thermal shrinkage between collars and coil during cool-down;

- stress redistribution due to the azimuthal component of the Lorentz forces at high current.

In the LHC dipole it has been chosen an azimuthal pre-stress at ambient temperature after collaring of 75 ± 15 MPa, which falls down to about 30 ± 7 MPa after the cool-down. The collars are made of 3 mm thick high-strength stainless steel sheet. They are closed around the two coils by means of three locking rods (see Fig. 2.8. Collars sheets are superposed one to the other to create packs, assembled using little pins. Each layer is composed of two different parts, the so-called "long-collar" and the "short-collar". The long-collar contains the holes where to put the locking
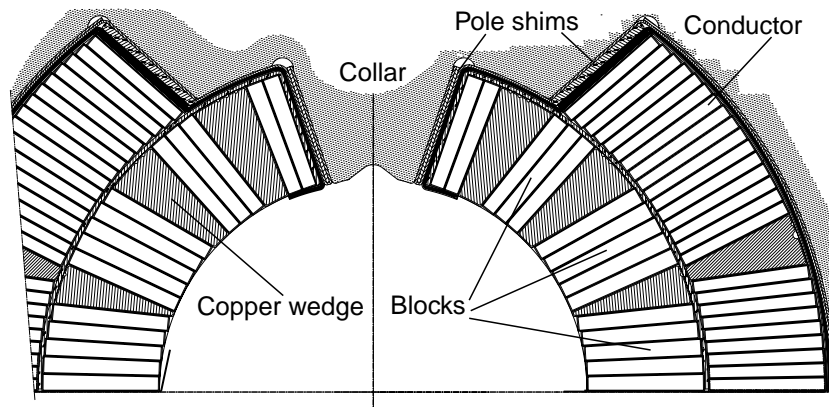
Figure 2.9: The pole shims.

rods. The short one has indeed a pure filling function. Different layers of collars are assembled putting alternatively the long collars on the upper part and on the lower part of the magnet.

The pole shims

Collaring shims, made of fiberglass, are located at the poles between the coil and the collar (see Fig. 2.9). They represent an effective way of changing the pre-stress and the azimuthal coil length, acting in turn on the multipolar contents of the magnetic field.

In fact, by modifying the pole shim size, it is possible to change the space available for the coil inside the collar cavity, thus varying the azimuthal pre-stress exerted by the collar on the coil. This means that the pole shims allow to compensate the possible difference of coil dimension during production with respect to the nominal design obtaining at the end of the collaring the nominal pre-stress. Moreover they can be used also for fine tuning the field quality during the magnet production. In fact, if the pre-stress is varied, also the total azimuthal coil lenght, and consequently the field quality, is modified.

2.2.5   The yoke and the shrinking cylinder

The ferromagnetic yoke (see Fig. 2.10) contributes to increase the magnetic field inside the aperture of about the 20 % and confines the field flux, so that very low field exits from the cold mass. Moreover, it represents an extra support for the collared coil against the radial component of the Lorentz forces. The yoke consists of two halves of low carbon steel laminations 5.8 mm thick. To ensure that the collar are in contact with the yoke at 1.9 K after the cool-down, the two halves are designed
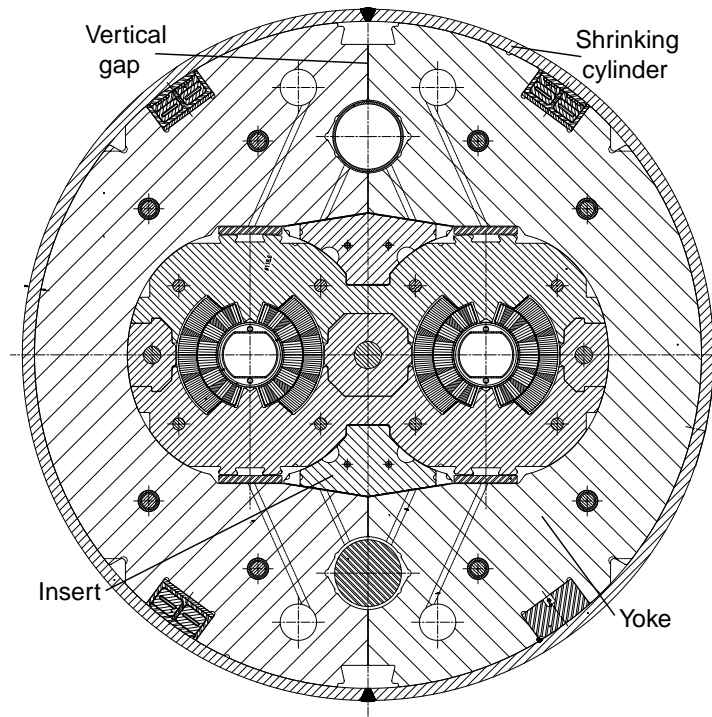
Figure 2.10: The cold mass.

with a vertical gap of about a tenth of mm, which corresponds to the differential shrinkage between the collars and the yoke.

The yoke lamination are contained by the shrinking cylinder, which is composed of two half shells about 15 m long. The two half shells are welded with interference around the iron yoke. The interference generates a tensile stress of about 150 MPa in the cylinder. The force exerted by the shrinking cylinder on the two yoke halves closes the gap at ambient temperature and it is transmitted to the collar horizontally on the mid-plane and vertically via the ferromagnetic insert (see Fig. 2.10). The collared coil is slightly deformed by the force exerted by the yoke and the cylinder, and a small increase of the coil azimuthal pre-stress (about 6 MPa) occurs.

After the cool-down, this deformation of the collared coil induced by the yoke disappears because of the differential thermal contraction between collars and yoke, leaving only a contact on the mid-plane which ensures a radial support to the collared coil during the excitation to the nominal field.

With respect to the single aperture design, the two-in-one geometry features a magnetic cross-talk between the two apertures [23]. In fact, the system consisting of two identical dipole coils, charged in opposite direction and with surrounding yoke, does not exhibit full symmetry with respect the vertical axes. Hence even normal field harmonics occur. Nevertheless, they can be optimise by the ferromagnetic

insert, which has a significant influence on the low order even harmonics.

2.2.6   The cold mass and the cryostat

The dipole cold mass is roughly 23.8 t weigh and about 15 m long. It is placed on three support posts each consisting of a low thermal conductivity composite tubular column. Inserted inside the vacuum vessel it forms the so-called dipole cryostat (see Fig. 2.2). The dipole cryostat runs at three temperature levels, 1.9 K for the cold mass, and at 4.5 - 20 K and 55 - 75 K for the two intermediate heat intercept levels. The two thermal shields are installed to minimize heat inleaks to the cold mass at 1.9 K. The radiation screen uses multilayer superinsulation enclosing the cold mass. The outer thermal shield, which intercepts the largest fraction of incoming heat at 55 - 75 K, consists of a self-supporting aluminium screen covered with multilayer superinsulation. A helium-gas-cooled aluminium pipe forms part of the screen, which is divided into several segments to decrease movements during cool-down and warm-up. The vacuum vessel contains insulation vacuum at a pressure below 10^{-6} mbar and is made of steel. It will itself be supported at three points, coincident with the support posts.

Chapter 3

Thermo-mechanical properties of the coil

The thermo-mechanical properties of the coil, in particular the stress-strain relation and the thermal shrinkage, play a fundamental role in the structural and magnetic behaviour of the superconducting dipole. In fact, the magnetic field is strongly dependent on the conductor positions, which is related to the stresses applied on the coil at ambient and at cryogenic temperature and on the induced coil deformations. For the analysis of the field quality in the superconducting dipole it is therefore mandatory to start with a precise definition of the mechanical properties of the coil.

Measurements of the thermo-mechanical properties of the coil have been carried out for most of the superconducting magnets for accelerators: the observed phenomena are rather unusual due to the composite structure of the involved material [24, 25, 26, 27, 28]. It is well known that the stress-strain relation is not linear [8, 9, 10]. Moreover, the unloading phase is considerably different from the loading one and varies according to the maximum load reached in the compression phase (mechanical hysteresis). As the superconducting coil is subjected to a loading-unloading cycle during magnet assembly, the final state of the coil at room temperature and its dimension [29, 30] is determined not only by its stress-strain relation, but also by the cycle used during the magnet assembly process.

The knowledge of the thermal contraction of the insulated cables [31, 32] is instead essential to explain why, during the cool-down, there is in general a non-negligible loss of azimuthal pre-stress. This loss is typically induced by the different thermal shrinkage between the coil and the collars. However, the measurement of the integrated thermal contraction coefficient of the coil is rather problematic. As stated in [11], "*with such a ill-behaved material, a direct measurement of the thermal-contraction integral [...], at zero stress, is not very meaningful*".

In this chapter we present measurements of stress-strain relation that we have performed on the two superconducting insulated cables of the coil at $293\,\mathrm{K}$ and at $77\,\mathrm{K}$. In particular, we focus on measurements of the stress-displacement curves along different loading and unloading paths, to obtain the data required to a com-

plete modeling of the elasticity of the coil [33, 34]. By measuring the stress loss of the cables inserted in a steel fixture, we compute the integrated thermal contraction coefficient from 293 K to 77 K, at which most of the thermal contraction takes place [35]. We also point out that the integral thermal contraction strongly depends on the selected operation procedure and in particular on the method to evaluate the strain. This explains the rather large variation of thermal contraction values reported in the literature [11, 12, 13, 14, 15, 16].

3.1 The samples

We measured two conductor stacks of 15.4×50 mm, one (22 conductors) with the cable used for the internal layer, and one (28 conductors) for the external layer. The cables are stacked alternately in order to have a parallel-side sample. As for magnet coils, the samples are submitted to the following sizing-bounding cycle:

- heating for 30 minutes at 130 °C under a moderate stress (about 10 MPa);

- compression to 80 MPa and heating up to 185 °C in a fixed volume for about 30 minutes;

- cool-down to room temperature in clamped fixture.

3.2 Elastic modulus at 293 K

3.2.1 Experimental set-up

The stress-displacement curves have been measured using an electro-mechanical apparatus for high precision compression tests (UTS 200.4). The load is applied perpendicularly to the flat face of the conductors, which corresponds to the azimuthal direction in the dipole coil. No loads or constraints are applied in the direction parallel to the flat face of the cable. The precision of the cross-head motion for the displacement measurements is $1\,\mu$m, while the error on the values of the force is of $\pm\,10$ N. The machine compresses the stacks with a constant cross-head speed of 0.05 mm/s: this value is similar to that used for clamping the dipole coils inside the collars [38]. A description of the calibration of the experimental apparatus using materials with known properties is given in Appendix A.

3.2.2 Experimental procedure and general features

In Fig. 3.1 and Fig. 3.2 we plot the stress versus the height of the conductor stacks (inner layer and outer layer respectively) measured by the electro-mechanical apparatus.
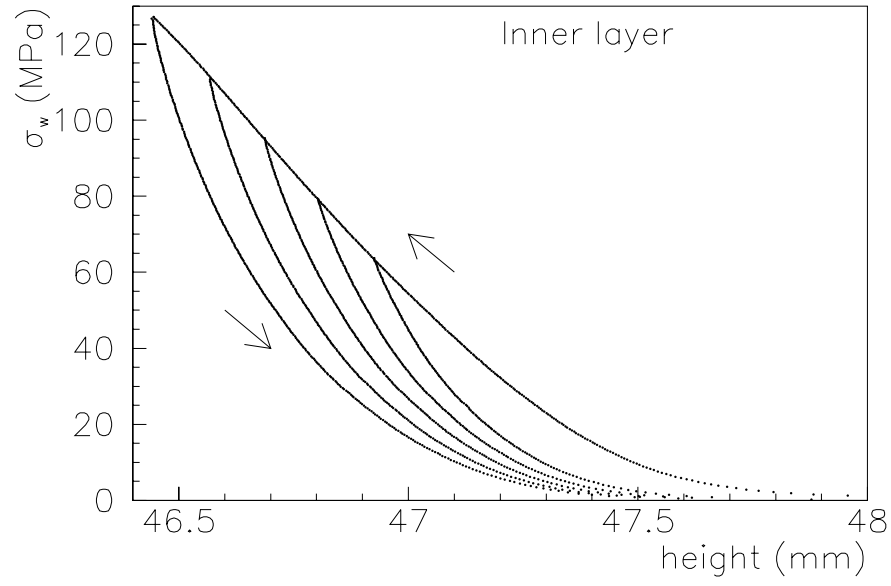
Figure 3.1: Stress σ_w (MPa) at 293 K versus total height l_w (mm) for the inner layer conductor stack, loading and unloading curves from different peak stresses (measured data).

Figure 3.2: Stress σ_w (MPa) at 293 K versus total height l_w (mm) for the outer layer conductor stack, loading and unloading curves from different peak stresses (measured data).

The compression force is increased until a given peak value, then reduced to zero. We performed five different loading cycles with decreasing peak stresses, respectively 127 MPa, 111 MPa, 95 MPa, 79 MPa and 63 MPa. After each cycle, when the stress on the stack is reduced to zero, the contact between the stack and the flat-plate fixtures of the electro-mechanical apparatus is deliberately lost: this allows the stack to relax completely. By letting the stack completely unloaded at the end of each cycle, we obtained an excellent reproducibility of the loading curve during the various cycles.

As it is well-known, the stacks feature a rather different mechanical behaviour in the loading and in the unloading branches. The loading phase is characterised by a smaller slope, whilst the loading-unloading cycle shows a hysteresis which depends on the peak stress reached during the compressive phase. On the other hand, the stress-displacement curves are non-linear, both in the loading and in the unloading phases: this indicates the stack rigidity increases with stress.

Different loading procedures

To better characterised the stack properties we performed two additional mechanical tests. Firstly, we compressed the stack with partial unloadings during the pressure rise (see Fig. 3.3): this is the procedure used during the collaring of the coil [38]. After partial unloading, the re-loading phase is almost identical to the unloading curve, until one reaches the maximum stress of the previous loading phase. Afterwards, the loading cycle continues along the standard loading curve. The total deformation at the end of the compression phase is given by the monotonic loading curve and it is not affected by the partial unloading applied to the stack. This phenomenon has been observed also for the impregnated Nb_3Sn composites [43, 44].

The results of the second test is shown in Fig. 3.4. We performe two consecutive cycles: the first one starts from a completely unloaded condition, and the second one is performed after the first cycle without a complete removal of the stress. In these conditions the stack shows some memory of the deformation of the first cycle during the loading curve, which has a slightly higher slope.

3.2.3   Definition of elastic modulus

At room temperature, the elastic modulus E_w is given by

$$E_w = \frac{d\sigma_w}{d\epsilon_w} = \frac{d\sigma_w}{dl_w}l_{w0} \tag{3.1}$$

where l_{w0} is the unloaded stack height and σ_w is the stress measured at ambient conditions. The stack is very soft at low stress, where small stress changes give rise to very large displacements (see Figs. 3.1 and 3.2). Following [11, 12], we define l_{w0} as the stack height for a small stress: to this purpose we conventionally selected a value of 0.4 MPa on the loading curve. We evaluate this parameter as the average
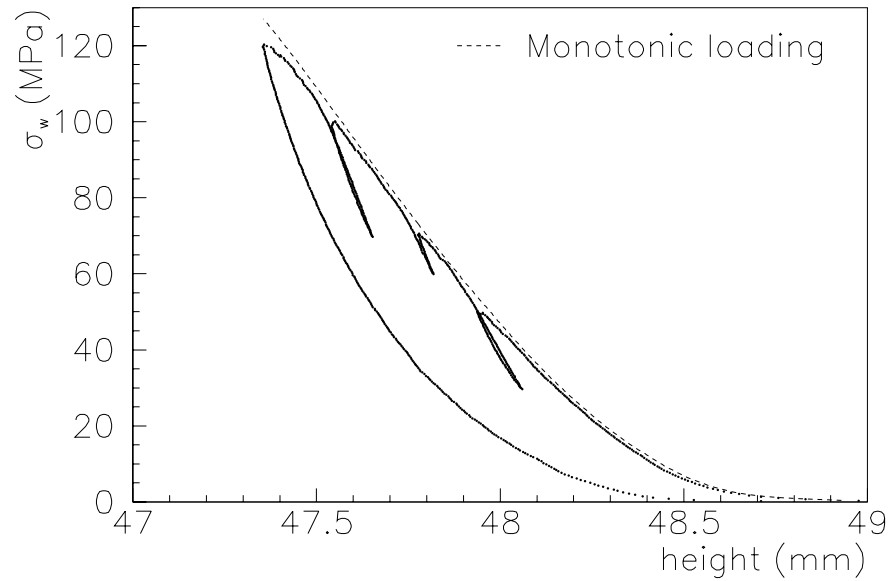
Figure 3.3: Stress σ_w (MPa) at 293 K versus total height l_w (mm) for the outer layer conductor stack, loading with three steps: measured data and comparison with the monotonic loading curve.
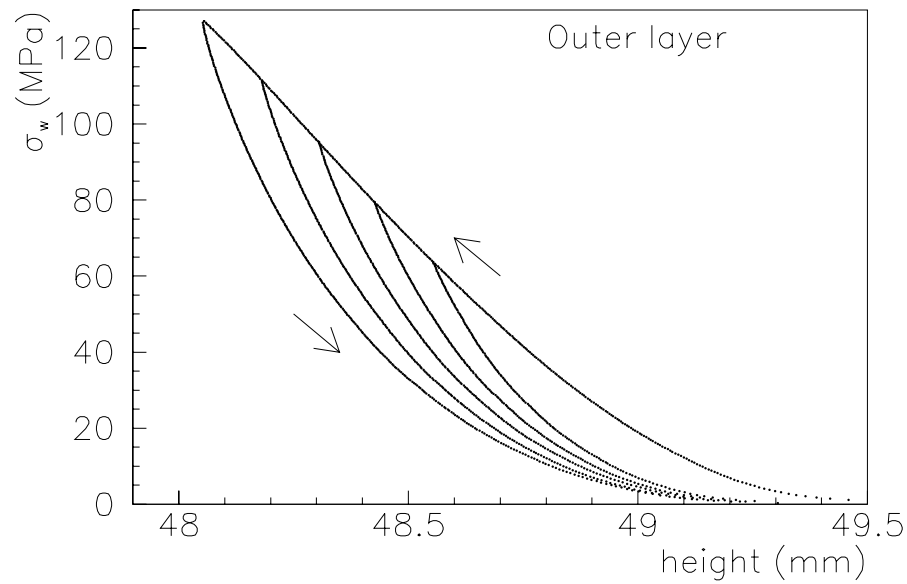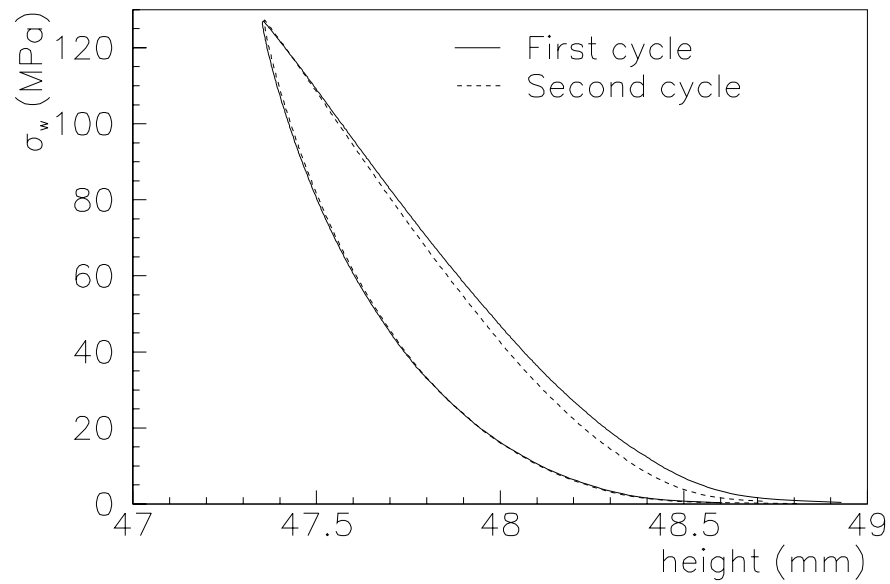

Figure 3.4: Stress σ_w (MPa) at 293 K versus total height l_w (mm) for the outer layer conductor stack: measured data in two consecutive cycles.

Figure 3.5: Elastic modulus E (GPa) at 293 K versus stress σ_w (MPa) for the conductor stacks, loading curves.

of the stack height over 15 different cycles and we assign to our final measurement a statistical error of $2 \times$ the standard deviation σ observed over the 15 cycles (giving a 95 % confidence level). We obtain an unloaded height of 48.16 ± 0.14 for the inner layer stack and 49.51 ± 0.08 for the outer layer stack. The relative error $\delta l_{w0}/l_{w0}$ of 0.3 % introduces a negligible error in the determination of the elastic modulus according to Eq. (3.1). To evaluate the tangent of the stress-displacement curves, we fitted the measured data with a fifth order polynomial and we analytically computed the derivative of the interpolating curve. This method provides more precise results with respect to a numerical evaluation of the derivative from the experimental data themselves.

3.2.4   Results

In Fig. 3.5 we plot the elastic modulus of the inner and outer stacks computed by the stress-displacement loading curves at 293 K: it features a large increase (from 0 MPa to 6 GPa) up to a stress of 70 MPa, and then it remains almost constant for higher stresses in the range from 70 MPa up to at least 100 MPa. No significant differences are observed between the two layers. In Tab. 3.1 we give the numerical values of the elastic modulus of the inner and the outer layer computed along the loading curve (an error of $2 \times \sigma$ is considered).

During the unloading phase the elastic modulus is much larger than the one

Figure 3.6: Elastic modulus E (GPa) at 293 K versus stress σ_w (MPa) for the inner layer conductor stack, unloading curve.

of the loading phase and it features an almost linear dependence on the stress, as already observed in [39], but, as shown in Fig. 3.6 and Fig. 3.7, it depends on the peak stress.

For the same load, the higher the peak stress of the cycle, the smaller the elastic modulus. For instance, at 75 MPa, i.e. the nominal stress chosen in the LHC dipoles at the end of the magnet assembly, the elastic modulus varies from 11 GPa to 14 GPa for the inner coil and from 10 GPa to 13 GPa for the outer coil for a peak stress of the compression cycle varying between 80 MPa and 130 MPa. Numerical examples are given in Tab. 3.2. Each value is reproducible within ± 5% with a level of confidence of 95 %.

Table 3.1: Elastic modulus (GPa) of the conductor stacks at different stresses (MPa) and at 293 K during the loading phase.

Stress	Inner layer	Outer layer
25	4.2 ± 0.2	4.3 ± 0.2
50	5.8 ± 0.3	5.7 ± 0.3
75	6.6 ± 0.4	6.4 ± 0.3
100	6.8 ± 0.5	6.6 ± 0.4

Figure 3.7: Elastic modulus E (GPa) at 293 K versus stress σ_w (MPa) for the outer layer conductor stack, unloading curve.

3.3   Elastic modulus at 77 K

3.3.1   Experimental set-up, procedure and general features

The measurements at 77 K have been performed in a cryostat filled with liquid nitrogen. The calibration of our experimental set-up obtained on materials with known properties is described in Appendix A. Also in this case, we performed five different loading cycles with decreasing peak stresses, respectively 100 MPa, 75 MPa, 60 MPa, 45 MPa and 30 MPa. In Fig. 3.8 and Fig. 3.9 we show the stress-displacement curves obtained at liquid nitrogen temperature for the inner and outer layer respectively. The curves feature two main differences with respect to the results at 293 K: firstly, the loading branch is characterised by a steeper slope than at room temperature. Secondly, the hysteresis between the loading and the unloading curves is considerably smaller.

3.3.2   Definition of elastic modulus

In order to compute the elastic modulus of the stacks, also at 77 K it is necessary to define its unloaded height. In analogy with the Eq. (3.1), the elastic modulus is defined as

$$E_c = \frac{d\sigma_c}{d\epsilon_c} = \frac{d\sigma_c}{dl_c}l_{c0} \qquad\qquad (3.2)$$
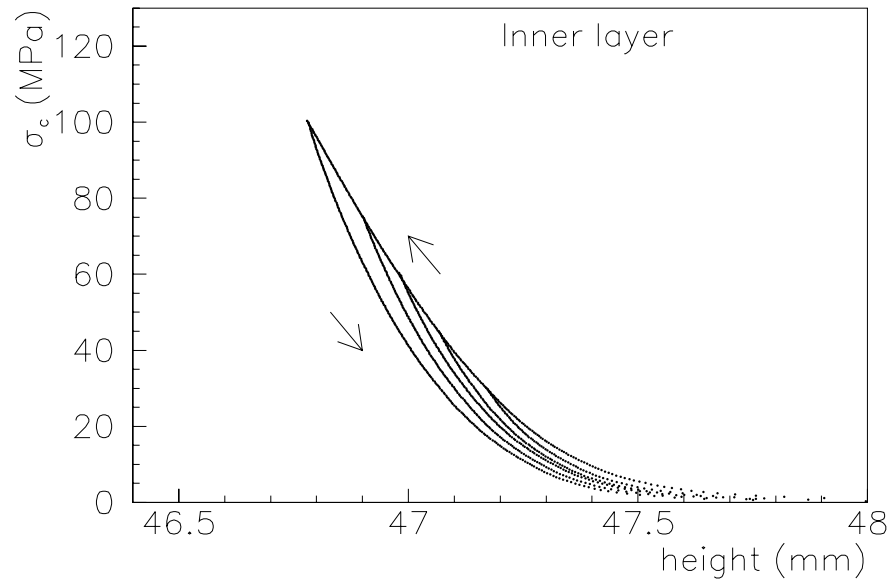
Figure 3.8: Stress σ_c (MPa) at 77 K versus total height l_c (mm) for the inner layer conductor stack, loading and unloading curves from different peak stresses (measured data).
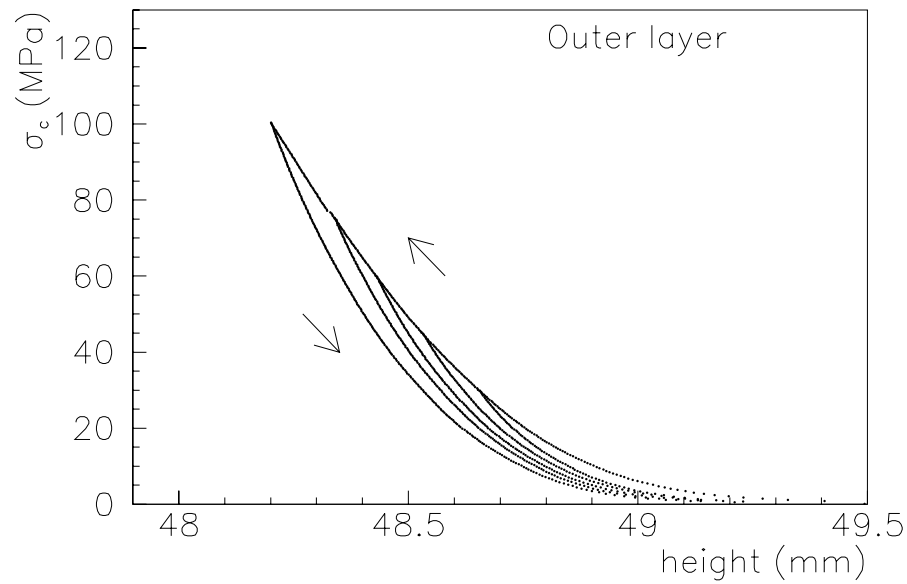
Figure 3.9: Stress σ_c (MPa) at 77 K versus total height l_c (mm) for the outer layer conductor stack, loading and unloading curves from different peak stress (measured data).

Table 3.2: Elastic modulus (GPa) of the conductor stacks at 293 K versus the stress (MPa) during the unloading phase starting from different peak stresses (MPa).

	Inner layer					Outer layer				
Peak	127	111	95	79	63	Peak	127	111	95	79	63
Stress		Elastic	modulus			Stress		Elastic	modulus		
25	4.9	5.2	5.4	5.7	5.8	25	4.5	4.9	5.1	5.4	5.7
50	8.0	8.7	9.4	10.2	11.1	50	7.2	7.9	8.6	9.4	10.4
75	12.2	13.2	14.2	–	–	75	10.7	11.8	12.8	–	–
100	17.0	18.1	–	–	–	100	14.8	16.1	–	–	–

where E_c, σ_c and l_{c0} are respectively the elastic modulus, the stress and the unloaded stack height at liquid nitrogen temperature.

Since our experimental apparatus for the stress-displacement measurements provides only relative displacements at nitrogen temperature and not absolute values of the stack height, it is impossible to detect the value of l_{c0}. To overcome this difficulty we propose to assume that $l_{c0} = l_{w0}$ for the numerical evaluation of the elastic modulus at 77 K. Indeed, the difference between l_{c0} and l_{w0}, that is the integrated thermal contraction, is of the order of 1 %. Therefore, by assuming $l_{c0} = l_{w0}$ in the computation of E_c, we introduce an error of 1 % which is negligible for our purposes.

3.3.3   Results

For stresses higher than 70 MPa the elastic modulus computed for the loading curve at 77 K (see Fig. 3.10) is about 50 % higher than the value at ambient temperature.

Table 3.3: Elastic modulus E (GPa) of the conductor stacks at different stress (MPa) and at 77 K during the loading phase.

Stress	Inner layer	Outer layer
25	5.4 ± 0.1	4.9 ± 0.3
50	8.2 ± 0.1	7.4 ± 0.3
75	9.8 ± 0.1	8.9 ± 0.3
100	10.2 ± 0.6	9.8 ± 0.3

On the other hand, in the unloading phase (see Fig. 3.11 and Fig. 3.12) the elastic moduli evaluated at 77 K are very similar to the ones at ambient temperature, but
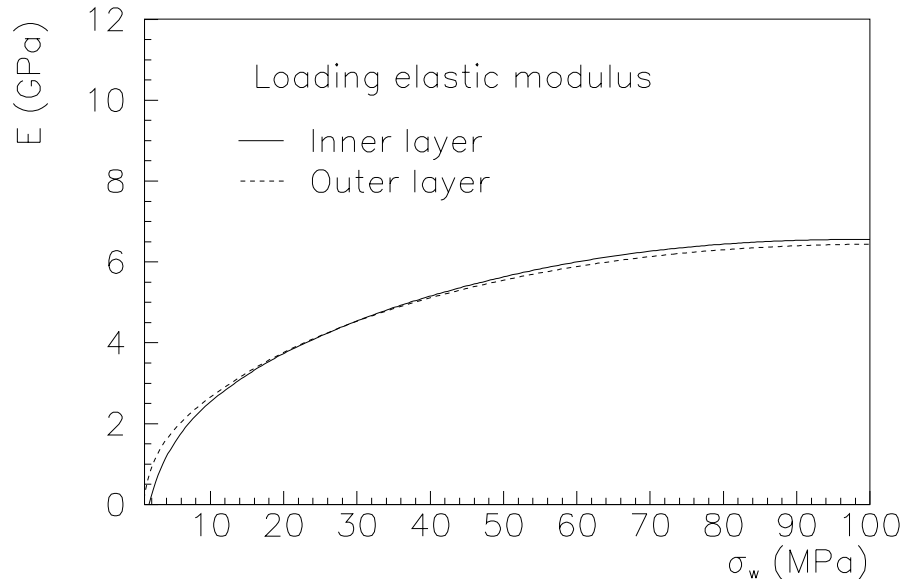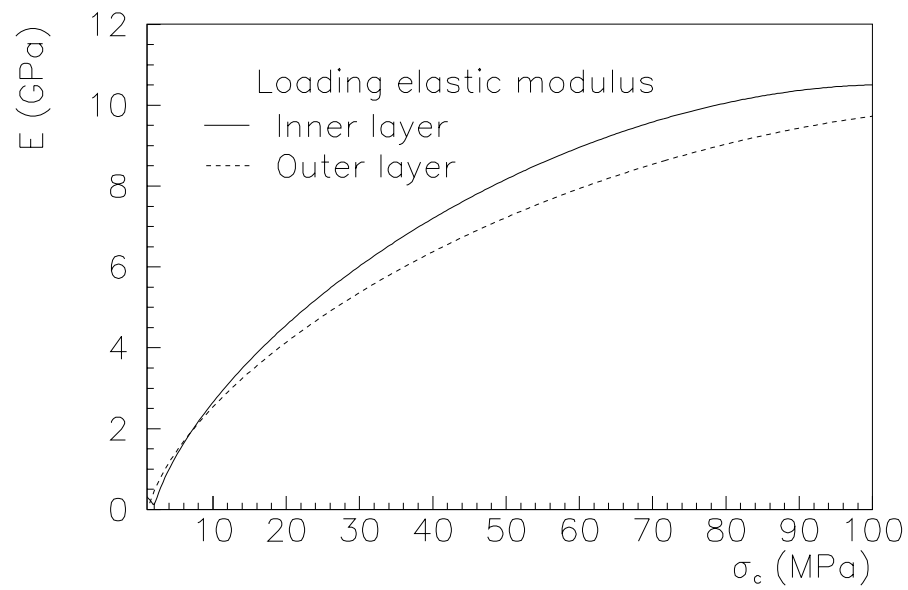
Figure 3.10: Elastic modulus E (GPa) at 77 K versus stress σ_c (MPa) for the conductor stacks, loading curve.
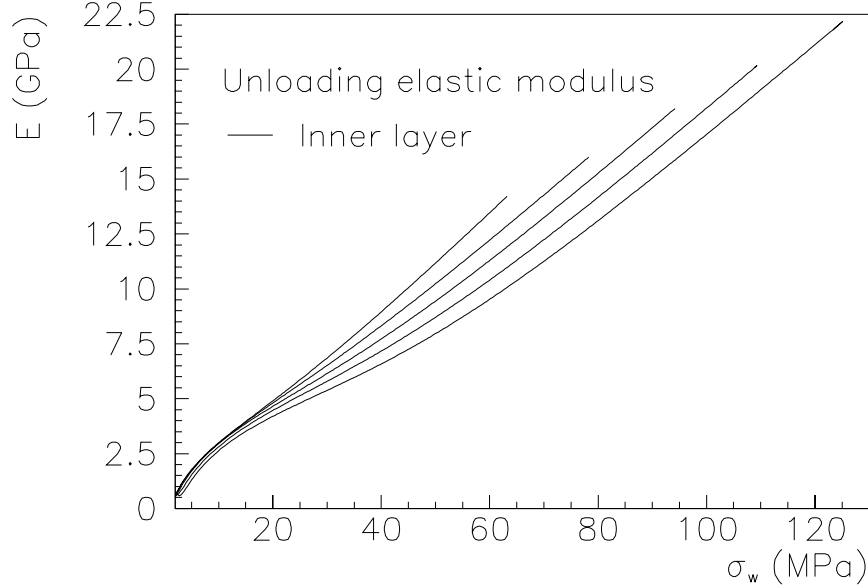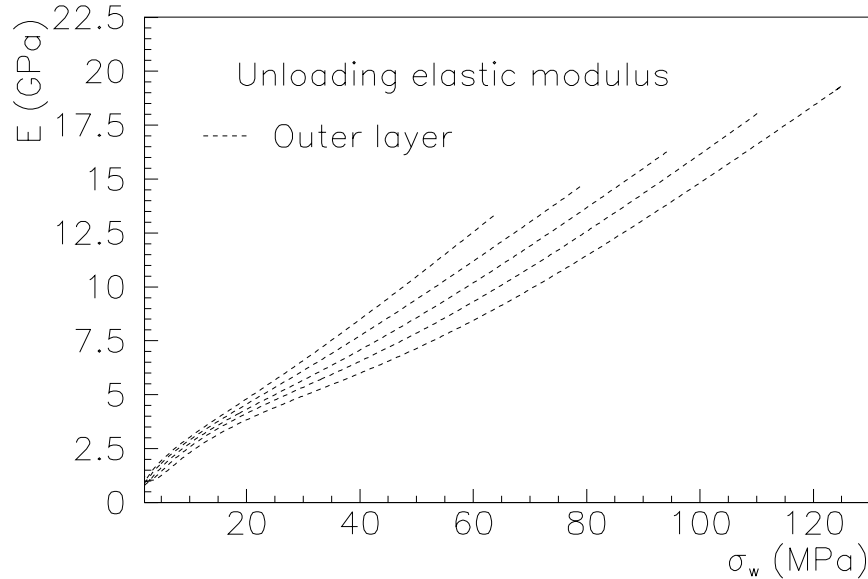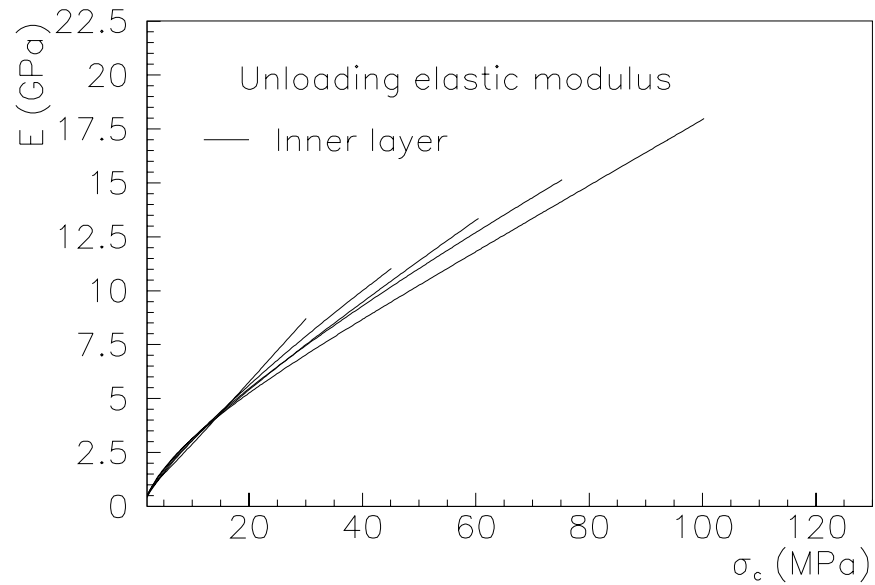

Figure 3.11: Elastic modulus E (GPa) at 77 K versus stress σ_c (MPa) for the inner layer conductor stack, unloading curve.
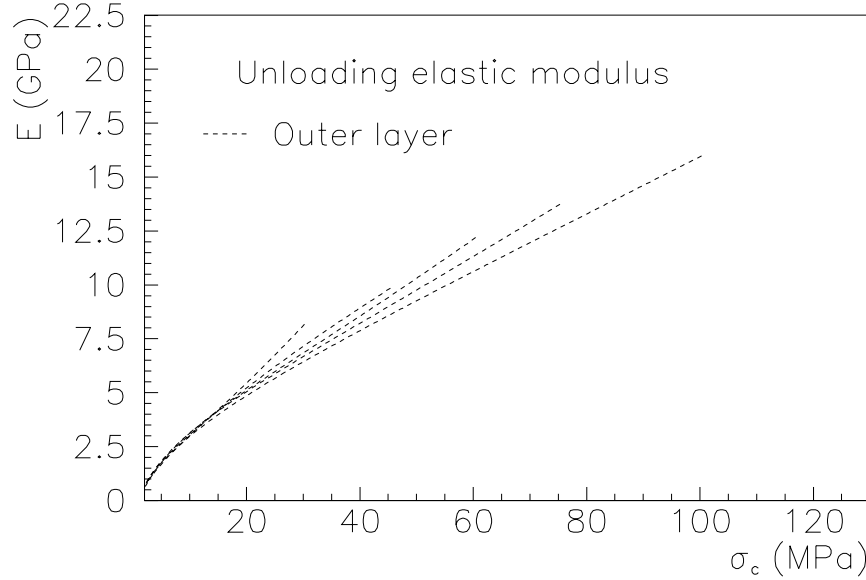
Figure 3.12: Elastic modulus E (GPa) at 77 K versus stress σ_c (MPa) for the outer layer conductor stack, unloading curve.

with a less pronounced dependence on the peak stress of the cycle. Numerical values are given in Tab. 3.3 and Tab.3.4.

3.4   Integrated thermal contraction

3.4.1   Measurement method

The integrated thermal contraction coefficient is defined as the relative difference of the unloaded heights between two temperatures [40], i.e.

$$\alpha = \frac{l_{w0} - l_{c0}}{l_{w0}}. \tag{3.3}$$

If one could measure the unloaded height at both temperatures, one could perform a direct estimate of α. In Sect. 3.2 we pointed out that the unloaded height of the stack is ill-defined: in fact, small variations of the load, say from 0 MPa to 1 MPa, induce large variation of the stack height of the order of 0.5 mm (see Fig. 3.1 and Fig. 3.2), i.e. 1 % of our sample height. This is the same order of magnitude of the integrated thermal contraction of the stack from ambient to cryogenic temperature [16, 13, 14, 15]. We also showed that, with a low stress of about 0.4 MPa, the stack height can be determined with a relative precision of about 0.3 %. This indetermination as well

Table 3.4: Elastic modulus (GPa) of the conductor stacks at $77\,$K versus the stress (MPa) during the unloading phase starting from different peak stresses (MPa).

	Inner layer						Outer layer				
Peak	100	75	60	45	30	Peak	100	75	60	45	30
Stress	Elastic modulus					Stress	Elastic modulus				
20	6.1	6.3	6.5	6.8	7.2	25	5.7	5.8	6	6.2	6.8
50	10.2	10.8	11.4	–	–	50	9.2	9.7	10.2	–	–
75	14.0	–	–	–	–	75	12.6	–	–	–	–
100	17.7	–	–	–	–	100	15.8	–	–	–	–

is comparable to the thermal shrinkage that we want to measure. Therefore, a direct measure of this quantity using Eq. (3.3) is not possible.

The thermal contraction can be also evaluated using the stress loss in a fixed cavity (see for instance [12]) and the stress-strain relation of the samples. In an infinitely rigid cavity of known integral thermal contraction coefficient α_f, the mechanical deformation of the sample is equal to the difference in thermal contraction:

$$\epsilon_w - \epsilon_c = \alpha_s - \alpha_f, \tag{3.4}$$

where α_s is the unknown thermal coefficient of the sample and ϵ_w and ϵ_c the deformations at ambient and cryogenic temperature. Here, we neglect terms of the order of $\epsilon\alpha$ with respect to ϵ and α. If the sample has a linear elastic behaviour, that is

$$\epsilon_w = \frac{\sigma_w}{E_{ws}} \qquad \epsilon_c = \frac{\sigma_c}{E_{cs}}, \tag{3.5}$$

one has

$$\alpha_s = \frac{\sigma_w}{E_{ws}} - \frac{\sigma_c}{E_{cs}} + \alpha_f. \tag{3.6}$$

In our case, we have a non-linear behaviour and therefore strain dependence on the stress has to be evaluated using experimental data. Eq. (3.6) can be generalised to include also the deformations of the mould. Let E_{wf} and E_{cf} be the elastic moduli of the cavity at warm and cold temperature respectively: then one has

$$\alpha_s = \epsilon_w(\sigma_w) + \frac{\sigma_w}{E_{wf}} - \epsilon_c(\sigma_c) - \frac{\sigma_c}{E_{cf}} + \alpha_f. \tag{3.7}$$

To deduce the thermal contraction from the measurement of the stress loss in a fixed cavity by Eq. (3.7), one must know strains, and therefore also in this case one has to make assumptions on the unloaded coil height. As already mentioned in the Sect. 3.3.2, an uncertainty on the unloaded stack height has a very little influence in

the definition of the elastic modulus, leading in our case to a maximum error of the order of 1%. On the other hand, different assumptions on the unloaded stack height lead to very large differences in the strains values $\epsilon_w(\sigma_w)$ and $\epsilon_c(\sigma_c)$ of Eq. (3.7) and consequently in α_s. Moreover, strains vary significantly according to the σ-ϵ relation assumed for the stacks: if we consider a linear behaviour, that is an elastic modulus independent on stress (see for instance [11, 12]), we will obtain a much lower strain value with respect to the case with the complete curve and therefore a different α_s. Finally, the hysteresis of the stress-strain curve at $77\,\mathrm{K}$ yields a further uncertainty to the problem. In fact, it is not clear how to evaluate $\epsilon_c(\sigma_c)$ in Eq. (3.7), since it is not known which curve is reached by the stacks at the end of the cool-down (loading or unloading).

One must conclude that the integral thermal contraction of a stack of film-insulated cables is not uniquely defined, as it depends on the scheme used to derive the strain from the displacements. Here, we propose the following scheme:

- We use the experimental non-linear stress-displacement relation to evaluate the strain from the stress:

$$\epsilon_{ws} = \frac{\Delta l_w}{l_{w0}} \qquad \epsilon_{cs} = \frac{\Delta l_c}{l_{c0}}. \tag{3.8}$$

  The influence of a linear stress-displacement relation on the evaluation of the strains and of the thermal contraction is discussed in Appendix B.

- We fix the unloaded coil height l_{w0} and l_{c0} as the height of the stack measured with the electro-mechanical apparatus at a stress of 0.4 MPa on the loading curve, as already explained in Sect. 3.2 and Sect. 3.3. The influence of the cut-stress on the evaluation of the strains and of the thermal contraction is discussed in Appendix B.

- At $77\,\mathrm{K}$, we compute the strain after the cool-down $\epsilon_c(\sigma_c)$ both on the loading curve and on the unloading curve, as represented in Fig. 3.13. In the latter path we consider the unloading curve starting from a peak stress $\sigma_c^p = \sigma_w$ (see Fig. 3.13). In this way we obtain two estimates of the integrated thermal contraction coefficient: the first describes the ideal case of a cool-down in absence of stress followed by the application of the stress up to σ_c on the loading curve. The second path instead describes another ideal case with a cool-down at constant stress σ_w followed by a reduction of the stress from σ_w to σ_c on the unloading curve. Analysing these two extreme cases, the obtained range of variation of the thermal contraction coefficient can be considered as an uncertainty associated to the hysteresis at $77\,\mathrm{K}$.
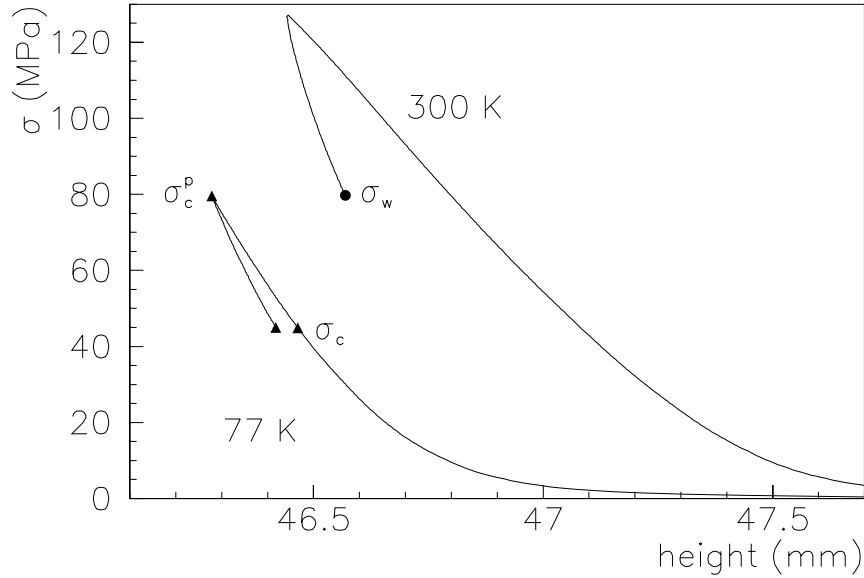
Figure 3.13: Representation of the cool-down in the stress-displacement plane.

3.4.2 Experimental set-up

We use a carbon steel mould (see Fig. A.1): the stress is applied by a screw, placed at the top of the mould, and is measured by two capacitive gauges [41], placed at the top and the bottom of the stack. The sensitivity of the capacitive gauges is 1 MPa. In order to measure the stress loss from warm to cold temperature, the device is submerged in liquid nitrogen in a cryostat. The integral thermal contraction coefficient from 293 K to 77 K is computed through Eq. (3.7) by the measurement of the stress loss (σ_w-σ_c) in the cavity. Tests of the apparatus on materials with known properties are presented in Appendix A.

3.4.3 Experimental procedure and results

We performed five different cool-downs with two stacks 100 mm high, one composed with inner layer conductors and one with outer layer conductors. At 293 K the stacks have been loaded to the peak stress and then unloaded to a value of stress σ_w equal to the 60 % of the peak stress. This procedure has been chosen to reproduce as much as possible the loading path followed by the coil during the magnet assembly before the cool-down [42]. For example, in the first measurement the stack has been loaded to 127 MPa and then unloaded to 80 MPa. The strain ϵ_{ws} has been computed as the difference between the stack height measured at 0.4 MPa on the loading curve and the height measured on the unloading curve at 80 MPa. At cryogenic temperature the strain ϵ_{cs} can be computed in the same way. Two estimates of the thermal

contraction coefficient are thus obtained by Eq.(3.7): the first one (α_l) by assuming that at 77 K the stack follows the loading curve, the second one (α_u) by considering that it follows the unloading curve whose peak stress at 77 K is σ_w. The estimated value of α is the average between α_l and α_u.

Table 3.5: Integral thermal contraction coefficient α (10^{-3}) of the stacks evaluated from 5 different stress losses.

Inner layer				Outer layer			
σ_w	σ_c	α_l	α_u	σ_w	σ_c	α_l	α_u
78	45	12.0	10.9	81	43	10.0	8.8
70	39	10.5	9.5	69	36	8.6	7.5
60	35	8.7	7.8	61	29	7.7	6.8
50	27	7.7	6.8	50	20	7.2	6.1
40	19	7.1	6.2	40	14	6.4	5.3

In Tab. 3.5 we present the results of the stress losses for the inner and outer layer. The dependence of α on the stress σ_w is very important: one observes a variation from 0.006 - 0.007 for $\sigma_w = 40$ MPa up to 0.009 - 0.012 for $\sigma_w = 80$ MPa. In Fig. 3.14 and Fig. 3.15 we plot α as a function of σ_w, the error bars being the difference between α_l and α_u. We can see that the error bars have non-negligible values of about 10^{-3}.

Modifications of thermal shrinkage of the mould

In order to check if the integral thermal contraction coefficient of the coil depends not only on the stress at 293 K, but also on the stress at 77 K, we made additional measurements on the outer layer stack, cooling down from the same stresses at warm, and changing the stresses at cold by modifying the thermal shrinkage of the mould. This can be realized by replacing half of the stack with a material with a known thermal shrinkage, different from that of the press. For such a filler piece, we used either aluminium or invar: in the first case the cavity has a lower thermal shrinkage, and the stress loss is increased; in the second case one has the opposite situation. In these specific experiments Eq. (3.7) becomes

$$\alpha_s = \epsilon_{ws} + \frac{\sigma_w}{E_{weq}} - \epsilon_{cs} - \frac{\sigma_w}{E_{ceq}} + \alpha_{eq}. \tag{3.9}$$

where

$$\frac{1}{E_{weq}} = \frac{R+1}{E_{wf}} + \frac{1}{E_{wm}}, \tag{3.10}$$
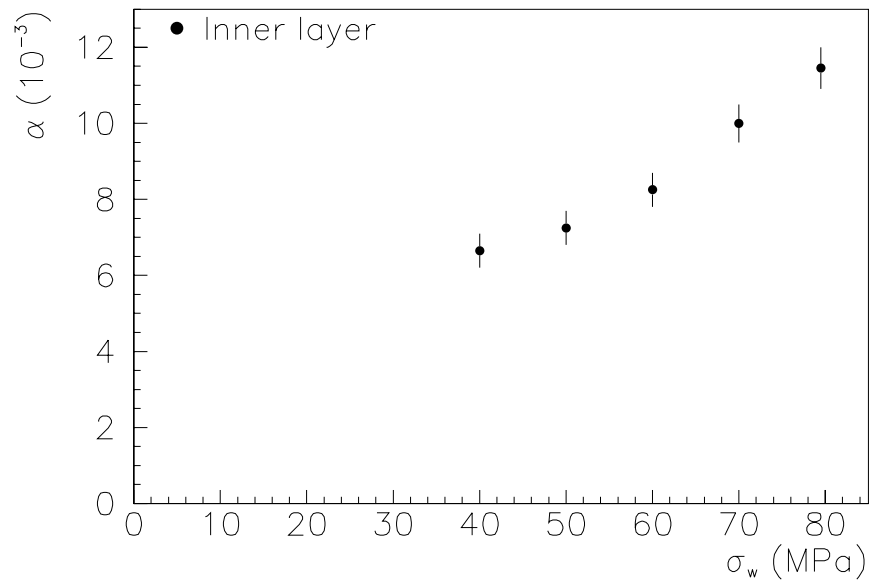
Figure 3.14: Integrated thermal contraction coefficient α versus stress σ_w at $293\,\mathrm{K}$ for the inner layer stack.
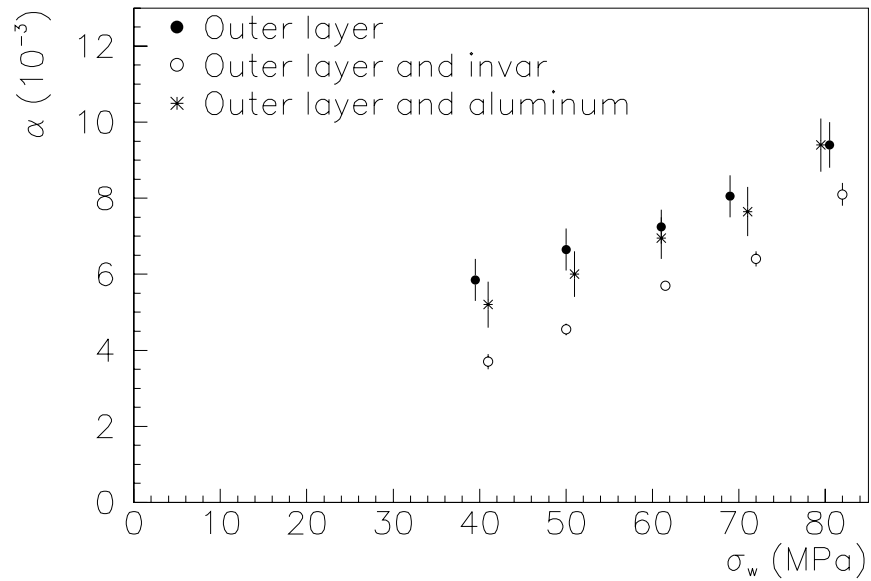
Figure 3.15: Integrated thermal contraction coefficient α versus stress σ_w at $293\,\mathrm{K}$ for the outer layer stack, with different equivalent thermal shrinkage of the mould.

$$\frac{1}{E_{ceq}} = \frac{R+1}{E_{cf}} + \frac{1}{E_{cm}} \tag{3.11}$$

and

$$\alpha_{eq} = \alpha_f - R(\alpha_m - \alpha_f). \tag{3.12}$$

In Eq. (3.10), Eq. (3.11) and Eq. (3.12) R is the ratio between the height of the filler and the height of the stack, E_{wm}, E_{cm} and α_m are respectively the elastic modulus at room temperature, the elastic modulus at 77 K and the integral thermal contraction coefficient of the filler piece.

In Tab. 3.6 and in Fig. 3.15 the results are shown. No significant difference is found between the case of the full stack and of the stack with a filler in aluminium, whose stress losses differ by less than 10 MPa. A decrease in the thermal contraction coefficient of around 0.002 is found for the cavity with a filler in invar, where the stress loss is reduced by 15 - 20 MPa. This decrease is approximately constant for the five considered cases, leading to an offset between the two σ_w-α curves. One can conclude that the integrated thermal contraction of a stack of film-insulated cable depends on the stress at warm before the cool-down and on the stress at cold after the cool-down.

Table 3.6: Integral thermal contraction coefficient α (10^{-3}) of the stack evaluated from 5 different stress losses.

Outer layer and alum.				Outer layer and invar			
σ_w	σ_c	α_l	α_u	σ_w	σ_c	α_l	α_u
80	36	10.1	8.7	82	66	8.4	7.8
71	32	8.3	7.0	72	60	6.6	6.2
61	24	7.5	6.4	62	49	5.8	5.6
51	17	6.6	5.4	50	39	4.7	4.4
41	12	5.8	4.6	41	31	3.9	3.5

Chapter 4

Finite element model of the dipole cross-section

The thermo-mechanical properties of the coil presented in Chapt. 3 have been implemented in a finite element model of the dipole cross-section. This model allows computing stresses and strains arising inside the dipole during assembly and cooldown, taking into account the material properties of the magnet components and the applied loads.

After a brief description of the main characteristics of the finite element model used to study the behaviour of the LHC dipole, we describe in this Chapter an experimental verification of the reliability and of the validity limits of the model itself. The displacements of a short sample of the dipole coil are measured using an optical device implemented at the EPFL (Ecole Polytechnique Fédérale de Lausanne) based on the Speckle Interferometry. Then, measurements are compared with the FEM results [45, 46].

4.1   Description of the FEM

Thermo-mechanical analysis by mean of finite element codes have been carried out for most of the superconducting magnet for accelerators [47, 17, 48, 49]. The 2D model of the LHC dipole cross-section (see Fig. 4.1) has been implemented in the commercial code ANSYS^{TM} [6]. This model is used to compute the field of deformations and the stresses at $293\,\mathrm{K}$ and at $1.9\,\mathrm{K}$: a detailed description of the model can be found in [50, 51].

Since the dipole features two planes of symmetry, only one quarter of the cross-section has been modelled and boundary conditions have been put on the symmetry axes. All the areas have been meshed with the same kind of structural solid elements, i.e. PLANE42. The plane strain option has been imposed to these elements, since dipoles are much longer than their transversal dimension.

The appropriate material properties, i.e. Young modulus, Poisson's ratio and
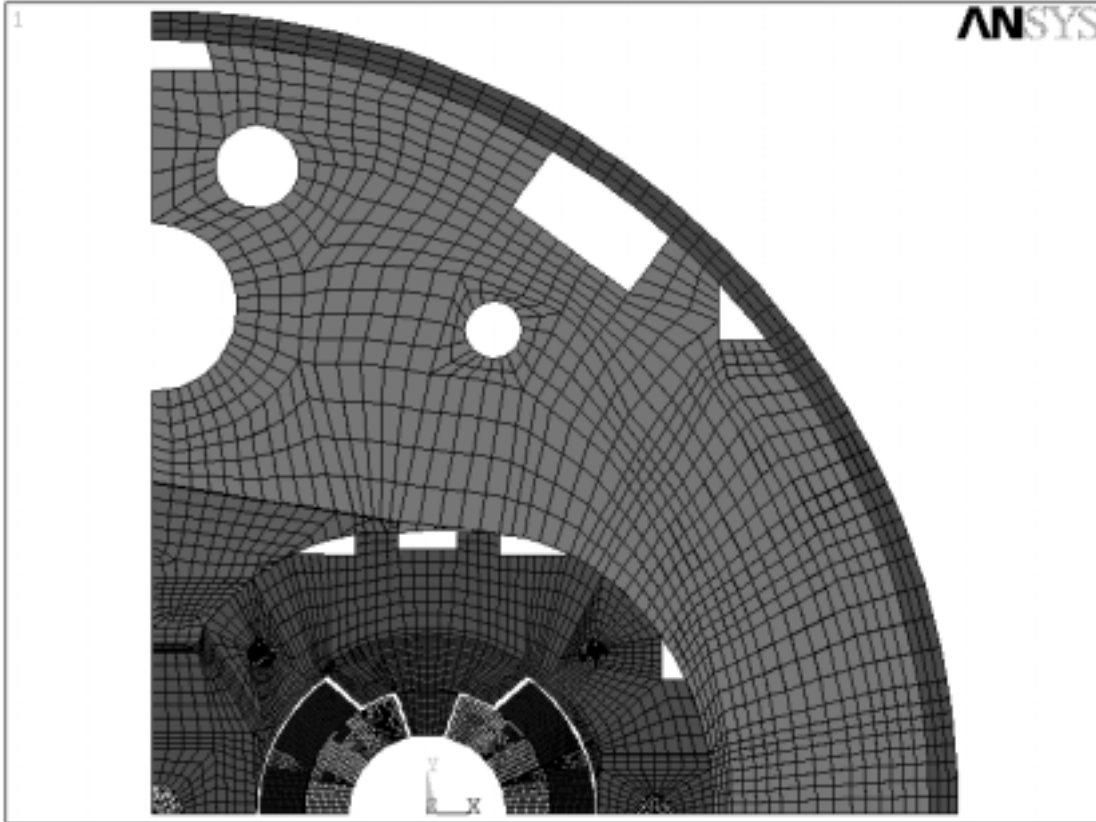
Figure 4.1: The finite element model of the dipole cross-section.

thermal expansion coefficient, for both room and low temperature have been associated to each area. Interface between surfaces of different components has been described using CONTACT52 elements, which also have the function of loading the model.

4.1.1 FEM of the coil

The coils are described only by their two principal components, i.e. block of superconducting cables and copper wedges. To reproduce the non-linear behaviour of the coils presented in Sect. 3, the elastic modulus of the blocks is not considered constant, but the loading part of the experimental curve described in Sect. 3.2 is inserted into the model [54]. We used the special "MELAS" properties, which create an isotropic material with elastic behaviour responding to the stress-strain curve inserted. Poisson's ratio is set at a value of 0.1, because of the influence of the polyimide insulation, which leads to some decrease respect to the 0.3 value typical for metallic materials.

Copper wedges areas are given the standard thermo-mechanical properties of the copper that can be found in literature, i.e. a Young modulus of 136000 MPa, a Poisson's ratio of 0.3 and an integrated thermal contraction coefficient of $3.3 \cdot 10^{-3}$.

4.1.2 FEM of the mechanical structure

In our model we have two superposed layers of meshed areas which represent the long-collar and the short-collar (see Sect. 2.2.4). Each collar layer is given a thickness of 0.5 mm, while all the other components of the dipole (as iron yoke, iron insert and shrinking cylinder) are modelled with PLANE42 elements 1 mm thick. In this way, the assembling effects of the two collars of the same layer and the presence of different layers are taken into account.

In Tab. 4.1 we give the material properties imposed to the structural components of the dipole.

Table 4.1: Material properties of the coil containment components.

Component	E at 300 K (MPa)	E at 1.9 K (MPa)	Poisson ν	α
Collar	190000	210000	0.3	$2.4 \cdot 10^{-3}$
Yoke	210000	225000	0.3	$2.0 \cdot 10^{-3}$
Insert	210000	225000	0.3	$2.0 \cdot 10^{-3}$
Cylind.	195000	209000	0.3	$3.0 \cdot 10^{-3}$

4.1.3 Modeling of the contact surfaces

As already mentioned, the interfaces between all the surfaces of the magnet components have been modelled using contact elements. The interaction between components which are not glued together but only assembled with pins is described using CONTAC52 elements (see [51] for a detailed description of their main characteristics). These elements react as springs in their normal direction, the response to loads being directly proportional to their deformation and to their normal stiffness.

By adjusting the normal stiffness we can simulate both direct and indirect contacts between two surfaces, i.e., contacts between two surfaces without any interlayer or with the presence of some filling material not explicitly modelled. In the first case contact elements have to transfer forces between the two surfaces and must avoid penetration between bodies. In the second case there is not a direct contact between two sliding surfaces, but contact elements are used to simulate the presence of thin layers of different materials as for instance the pole shims. In fact, this situation happens in all the zones between coils and collars and in the zone between the inner and the outer coil. The implicit modeling of all the thin layers reduces significantly

the time of computation. However, to model the deformations of the filling materials, one has to define an equivalent Young modulus for all the materials simulated, treating them as series springs.

Once defined the normal stiffness, the "initial status" of the elements must be imposed. In fact, contact elements can simulate three different situations: gap, contact and interference. In the first case, the force is transmitted between the two surfaces only when the gap imposed to the elements is closed. In the second situation, the contact elements avoid penetration between bodies. Finally, in the case of interference, the elements are initially pre-loaded in the normal direction and tend to push away one surface from the other.

The definition of the initial status of the contact elements allows also simulating a different dimension of the components. For instance, the interference imposed to the contact elements placed at the coil poles, between coil and collars, has been chosen to simulate the effect of the pole shims on the coil: this interference can be varied to model the effect of different pole shim thicknesses on the coil pre-stress.

Everywhere in our model, we choose not to model any friction, assuming that its effect is negligible.

4.2 Validation the model

The conductor displacements evaluated with the finite element model have been validated by comparing the results of the numerical computations with the optical measurement performed on a short model of the dipole coil at ambient temperature. In particular we checked the modeling of:

- the interface between coil and collar with the contact elements;

- non-linear mechanical behaviour of the coil.

These two items represent the most delicate and complex aspects of the finite element model of the dipole cross-section and their modeling has never been validated before. Previous similar works, related to the evaluation of the conductor positions, were mostly devoted to investigate quench risks. They based this evaluation on measurements of the induced electro-magnetic forces [52] or on tomographic images of the collared coil section [53].

4.2.1 Speckle Interferometry method

Speckle Interferometry is based on the coherent addition of the light scattered by the object surface with a reference wave, either plane or diffuse, and not necessarily originating from the object. The basic principle of the method resides in the cyclic correlation of the speckle patterns at the image plane of the CCD camera employed to detect the speckle irradiance. The phase change arising from object displacement

is coded by the reference beam under the assumption that the micro-structure of the surface is unaltered during the measurements. Only 2D displacements are investigated, on a plane perpendicular to the beam. The displacement undergone by the object is extracted by comparing speckle patterns, one taken before the object deformation and the other taken after. A variety of optical configurations have been reported to render the cyclic correlation directly dependent on the component of displacement one would wish to measure on the deformed object surface [55, 56].

Since the speckle technique allows to determine displacements along one axis at a time, for our purposes we have mostly focused our investigations to measuring displacement fields along the vertical axis. In fact, the vertical displacements are the main mode of deformation of the coils during assembly and their value is much higher compared to horizontal displacements. It is indeed in the vertical direction that the coils show a non-linear behaviour and they are also subject to the greatest stresses arising from assembly procedures.

4.2.2   Experimental set-up

The coil section and the hydraulic press

A 94 mm long segment of the dipole coils was assembled in a press to be analysed through optical measurements. The press is composed of two stainless steel blocks, molded as one collar aperture and kept together by two pistons (see Fig 4.2). The kind of loads applied by the press is somewhat different from the loads applied in the dipole during fabrication. First, the press is composed of uniform blocks, whilst collars are made of stainless steel lamination packets. Second, collars completely bound the coils, since they are assembled using locking rods (see Fig. 2.8), whilst the press blocks do not reach contact on the mid plane, since a certain gap remains also under pressure. The press is loaded using two hydraulic pistons, inserted within two holes in the press blocks.

Pistons are standard RWH-120, whose maximum applicable force is 124.6 kN each, with an 8 mm stroke. An hydraulic system composed by a pump controlled by a manometer gives power to them. The sensitivity of the manometer is 3 bars, which correspond to a stress of 0.2 MPa on the coil mid-plane. Given the maximum force applicable by the pistons and the coil surface (about 6000 mm^2), this apparatus permits to reach coil stresses up to a maximum of about 40 MPa on the coil poles (see Fig. 2.8). During the assembly of the LHC dipoles, the coils are loaded up to 120 MPa. Although the load value attainable by the press is much lower, it is enough to test the non-linear mechanical behaviour of the coil and to verify the response to loads of the FEM.

The coil sample tested in the press includes inner and outer layers as in the nominal dipole design. Filling layers between the coil and the collar and between internal and external layers are assembled in the press, thus allowing a realistic modeling of the interfaces in the dipole. A steel support is fixed to the lower part
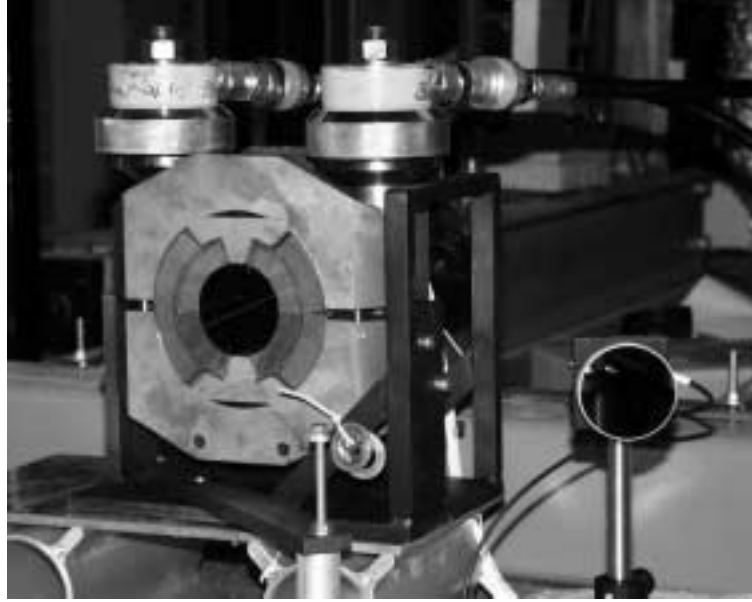
Figure 4.2: The press.

of the press, on both the lateral sides.

Loads are measured at the top and bottom arcs of the coils by eight capacitive force transducers (see Sect. 3.4.2): the sensitivity of the force transducers allows sensitivity in pressure of $1\,\mathrm{MPa}$.

The optical system

An optical configuration for measuring displacements along the horizontal (x) and vertical (y) direction is implemented using electronic speckle pattern interferometry (see Fig. 4.3). The equipment for optical measurements is positioned on a table whose vibrations are damped by oleo-pneumatic shock absorbers. The specimen is illuminated by two beams inclined at equal and opposite angles θ with respect to the surface normal z; the observation of the CCD camera is carried out along the z direction.

If a_1 and a_2 are the fields diffusely reflected from the specimen surface, the resulting intensity observed at a point in the observation plane before the object is deformed can be expressed as in:

$$I\left(x,y\right) = I_1 + I_2 + 2\sqrt{I_1 I_2}\cos\phi \tag{4.1}$$

where $I_1 = a_1 a_1^*$, $I_2 = a_2 a_2^*$ and ϕ is the speckle phase randomly changing over the image.
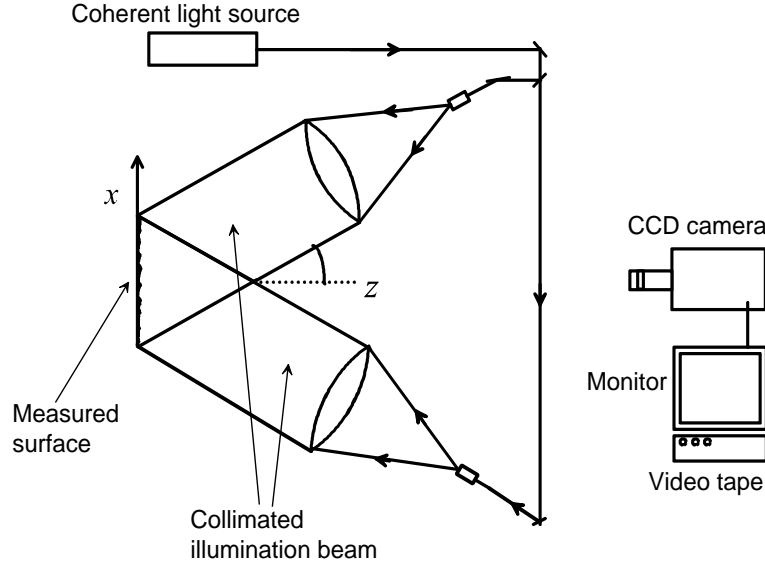
Figure 4.3: The optical system.

A CCD camera pointing along the z axis acquires two speckle images before and after object deformation. The subtraction between the two images is performed electronically by using a digital frame store. The resulting intensity distribution is representative of an interferogram in which the in-plane displacement (i.e. the displacement on the plane x, y) between two successive fringes is given by:

$$\frac{\lambda}{2 \sin \theta} \qquad (4.2)$$

where λ is the wavelength of the illumination beam. In our setting, we have $\lambda = 5145\,\text{Å}$ and $\theta = 10°$, so that we obtain a sensitivity of $1.5\,\mu\text{m}$.

4.2.3   Finite element model of the mechanical tool

The finite element code ANSYS^{TM} [6]has been used to develop the model of our experimental apparatus. The press model (see Fig. 4.4) represents one half of the tested coils. The press in fact features asymmetries between the top and the bottom boundary conditions but a perfect symmetry with respect to the vertical axis. Boundary conditions have been put on all the nodes along the y axis to block any displacement along the x axis. Since the deformations in the cross-section plane must be evaluated, we used a two dimensional model. All the areas have been represented with the same structural solid elements, i.e. PLANE42. The plane strain option has been imposed to these elements. Surface loads are applied to the top of the upper half and to the bottom of the lower half, in order to simulate the piston

load effect. The lower-left part of the press has boundary conditions representing the steel support. Material properties for the press areas are those of a typical steel, i.e. an elastic modulus of 190000 MPa and a Poisson's ratio of 0.3. The coils are modelled as in the model of the total dipole (see Sect. 4.1.1). The finite element model calculations give back stress-strain distribution as result of different load cases. For our purposes, we used the evaluated stresses to set the working point equal to the loading configuration of the experimental measurements. Then, displacements have been analysed and compared with the speckle interferometry images.
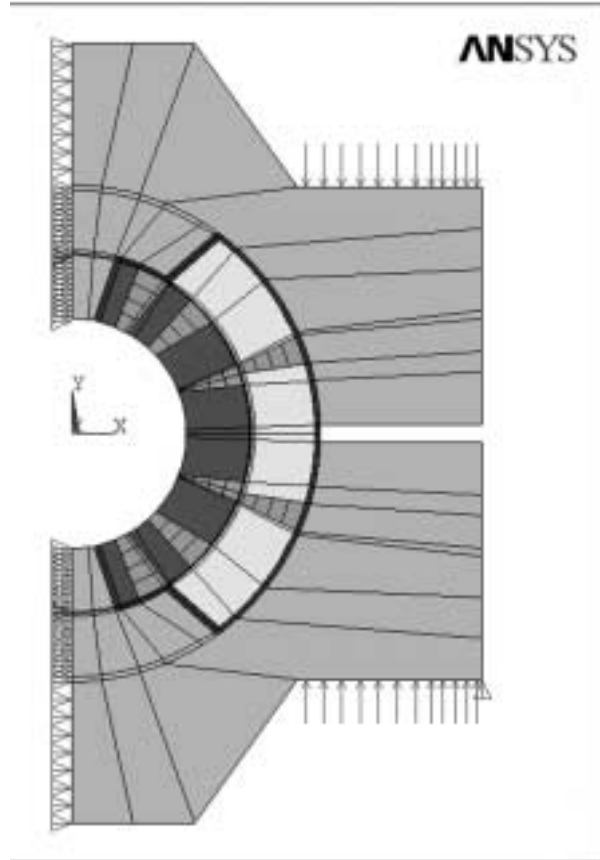
Figure 4.4: The finite element model of the press: area plot.

4.2.4   Test procedure

Initially, a short series of preliminary tests were made to obtain the desired resolution in optical measurements and to verify the behaviour of the mechanical apparatus. Regarding the optical system, a reduction of sensitivity was done. Speckle Interferometry usually detects displacements in fractions of a micrometer. This case,

displacements of a few micrometers were of interest. A coarse sensitivity was obtained by changing the magnification and varying the amount of shear introduced during the imaging process [55].

Once the press is positioned with the mechanical axis of the coil approximately parallel to the optical axis of the camera, a first loading-unloading cycle was made to stabilise the coil. Speckle Interferometry images show equal displacement fringes calculated as the difference between the deformed configurations of two different load cases.

First, the press is loaded and the gauges acquire the data relative to the stress at the top and at the bottom arcs of the coils. At the same time, a first acquisition is made with the optical system and a picture is stored. Afterwards, the load applied by the pistons is increased to a certain value, and a new acquisition is made both for the gauges and for the Speckle image. The increments of the stress are measured by the manometer, which is more sensitive than the gauges, and are typically $0.7\,$MPa for measurements of displacements along the y axis. The two images acquired before and after deformation are post-processed by a dedicated software and a new image is made, showing curves of equal displacements. Two consecutive fringes correspond to a difference in displacements of $1.5\,\mu$m.

To verify the modeling of the non-linear behavior of the coils, different measurements have to be done at different load steps. The same test procedure is repeated for four different cases: the starting load is increased from $10\,$MPa to $40\,$MPa. This way, a significant range of variation of the coil rigidity is covered. In order to check the results of the optical measurements against the FEM, two different calculations have to be done. The first computation provides the displacements at the starting. In the second computation the load is slightly increased. The differential displacements between the two situations are the computed and a comparison with the optical measurements is performed.

4.2.5   Results: model vs measurements

To compare pictures produced by the Speckle Interferometry and by the ANSYS^{TM} calculations, one has to plot the FEM results taking into account the optical measurements sensitivity. Since the optical apparatus has been calibrated to show equal displacement fringes spaced by $1.5\,\mu$m, the finite element results are plotted using the same scale.

In Fig. 4.5, Fig. 4.6, Fig. 4.7 and Fig. 4.8 results relative to the load cases along the y axis are shown. ANSYS^{TM} results, on the right part of the figures, show a certain number of equal displacement lines, whose distribution has to be compared with the fringes of the Speckle Interferometry picture, on the left.

As shown in Tab. 4.2, there is a good agreement between the number of equal displacement lines on the ANSYS^{TM} graphics and the number of fringes on the optical measurement picture. Fringe distribution is symmetric with respect to the vertical
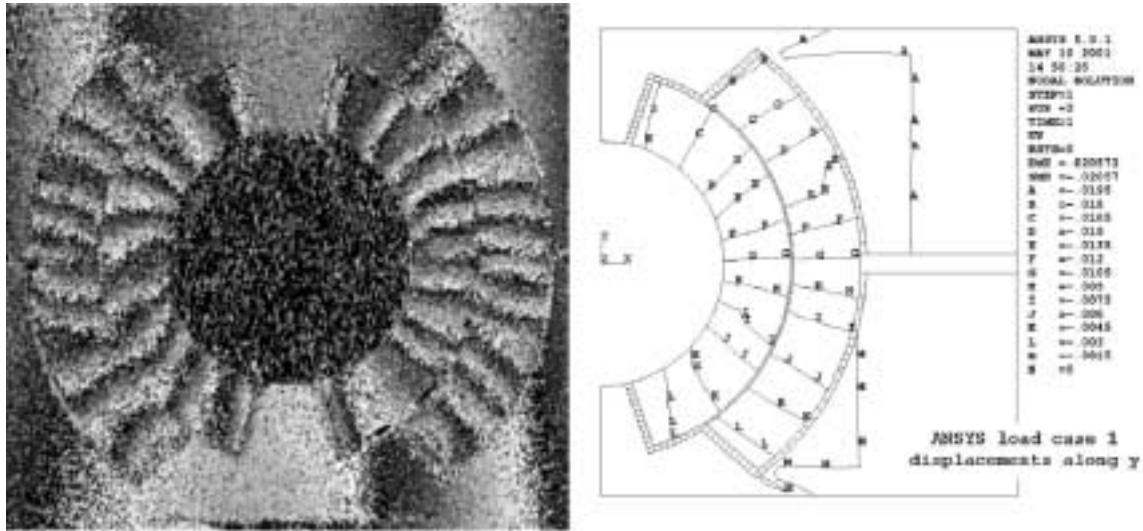
Figure 4.5: Speckle Interferometry image and ANSYS^{TM} displacements for the first load case.
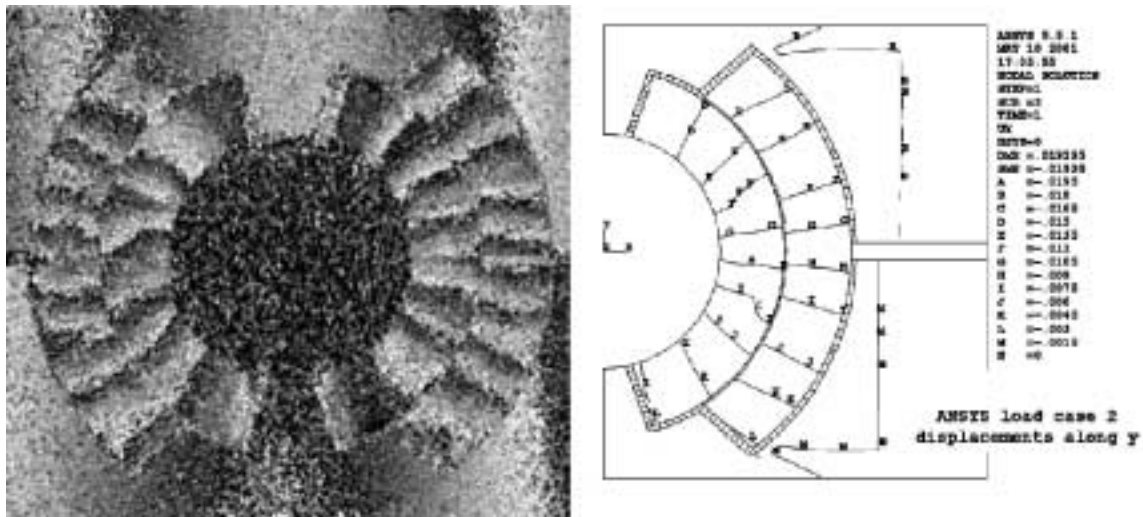
Figure 4.6: Speckle Interferometry image and ANSYS^{TM} displacements for the second load case.
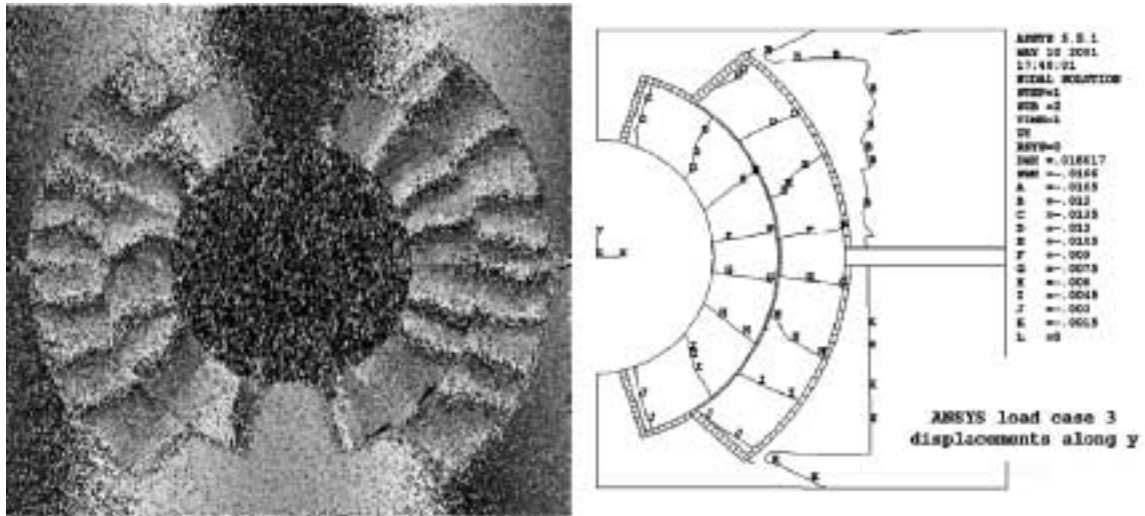
Figure 4.7: Speckle Interferometry image and ANSYS^{TM} displacements for the third load case.
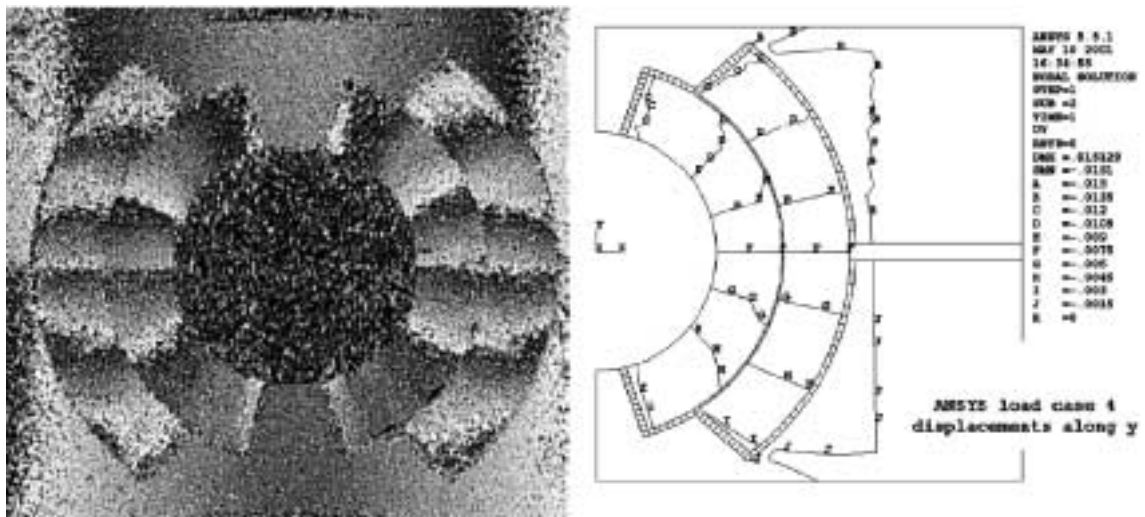
Figure 4.8: Speckle Interferometry image and ANSYS^{TM} displacements for the fourth load case.

and horizontal planes on both the images (ANSYS^{TM} and Speckle Interferometry results), verifying the assumption of symmetry.

Focusing on fringe distribution on the right half of the press, it is shown that fringes are not continuous between inner and outer coils. This depends on the gliding of the coils. Contact elements, used into the FEM model to represent these layers, reproduce this kind of behavior, even if the possible friction effect is neglected. A gliding between the coils and the press is observed by Speckle Interferometry, in agreement with FEM results.

Coil relative displacements are up to 17 mm (11 fringes), whilst on the corresponding press surface a relative displacement of the order of 1.5 mm only is observed.

It can be also pointed out that the total number of fringes decreases as the applied load increases from 10 MPa (Fig. 4.5) to 40 MPa (Fig. 4.8). Since the load step applied during optical measurements is the same for each case, one should expect for a linear behavior material a constant number of fringes. Indeed, the decrease in the number of fringes proves that the coil has a non-linear behavior, as it is found in mechanical tests.

Further considerations about the conductor displacements along the x axis and about the friction between coil and collars are presented in details in Ref. [45].

Table 4.2: Speckle Interferometry fringes and equal displacement lines from the FEM.

Load case	Inner coil fringes		Outer coil fringes	
(MPa)	Speckle	ANSYS^{TM}	Speckle	ANSYS^{TM}
10-11	10	11	11	11
20-21	8	9	9	9
30-31	6	8	8	8
40-41	5	7	5	7

Chapter 5

Mechanical behaviour of the dipole at 293 K

Here we evaluate the mechanical behaviour of the LHC dipole with the finite element model and we compare the results of the numerical computations with the experimental measurements. We focus our attention on the stresses and the deformations of the coil at ambient temperature after the collaring and at the end of the magnet assembling.

5.1 The collaring procedure

As already mentioned, the coil is clamped by austenitic steel collars. The collaring can be defined as the procedure to position, under a given azimuthal pre-stress, the coils into the collar cavities. This procedure requires that the coils, surrounded by the collars, are compressed in a press to a peak pressure in order to insert the locking rods. After the insertion of the rods, the press is released and only a fraction of this peak pressure is left. We define as *relaxation* [38] the ratio k between the remaining coil azimuthal stress after the collaring and the maximum coil azimuthal stress reached during the collaring phase.

The relaxation results from the combination of different effects. It is mainly due to the elasticity of the collars. In fact, the collars are not infinitely stiff: when the collaring press is released they are pushed up and vertically deformed by the coil pre-stress. We define as *spring-back* of the collars the ratio between the residual coil stress after collaring and the stress that a coil sees in a collar cavity infinitely stiff. Another contribution to the relaxation is given by the collar holes: to insert the collaring rods one needs some clearance between the holes and the rods that provokes a loss of pressure. Moreover the holes are plastically deformed under stress and this determines a further decrease of the stress. The last effect that must be considered is the the creeping of the poliymide, which contributes as well to the reduction of the remaining coil azimuthal stress after the collaring.

Stress measurements made with capacitive gauges [41] placed on the coil poles have been taken on the 1 m long dipoles prototypes (single aperture and double aperture) and on 15 m long dipole prototypes (see Tab. C.1, Tab. C.2 and Tab. C.3). In Fig. 5.1 we plot the values of the peak pre-stress and the remaining pre-stress given in Tab. C.1, Tab. C.2 and Tab. C.3: by fitting the data with a straight line we obtain a relaxation equal to 0.63 for the single aperture short dipoles, 0.7 for the double aperture short dipoles and 0.52 for the long prototypes.
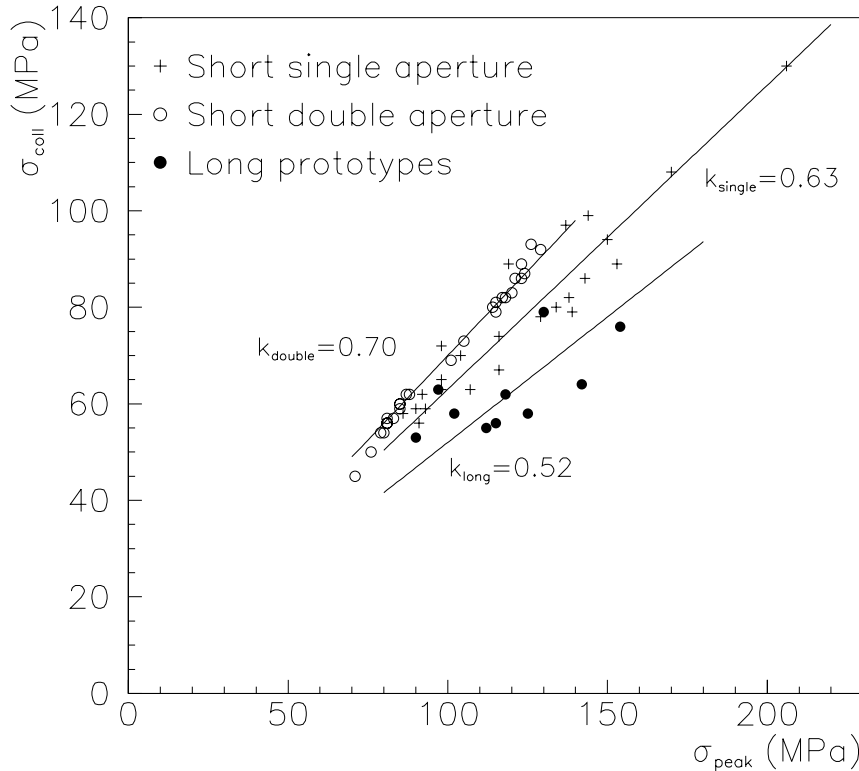
Figure 5.1: Measured relaxation: experimental data (markers) and linear fit (solid lines).

With respect to the short prototypes, a smaller value of the relaxation is observed for the long prototypes. In fact, in the 15 m long dipole a higher peak stress is reached during collaring, while the residual stress is comparable with the 1 m long dipole. This can be explained by pointing out that the residual stress is mainly due to the dimension of the coil and of the pole shim. On the other hand, the peak stress is choose during collaring in order to insert the locking rods. With the long prototypes it has been noticed that a higher peak stress must be reached for the insertion of the 15 m long locking rods along all the length of the magnet [38].

5.2 Modeling coil elasticity at 293 K

The relaxation k defined in the previous Section is a parameter which provides the "stress path" followed by the coil during the collaring. In our finite element model the collaring procedure is not explicitly modelled and loads are applied through interferences of contact elements: therefore the mechanical properties of the coil implemented in the model must include informations on the path followed during the collaring.

Moreover, one has to take into account that the stress-displacement curve of the coil is characterised by an hysteresis whose width depends on the peak stresses reached during the compression cycle (see Sect. 3.2). This means that if the coil azimuthal length is larger then the design value or if the pole shims are larger than the nominal value, during the collaring a higher peak pre-stress will be reached, and the unloading will take place along a different branch of the hysteresis (see Fig. 5.2).
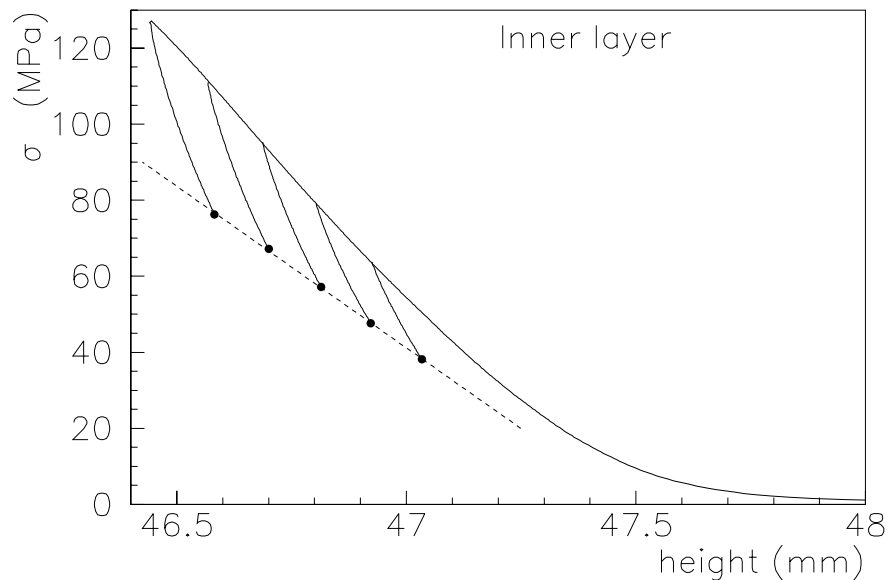
Figure 5.2: Equivalent stress-displacement curve (dashed line) for the coil inner layer.

Therefore, the elastic modulus of the coil to be input in the model is neither the loading nor the unloading, but an "equivalent" modulus that takes into account the peak pre-stress [57]. The equivalent stress-displacement curve, evaluated assuming a relaxation k of 0.6 between the residual pre-stress after collaring and the peak pre-stress during collaring, is shown for the inner coil in Fig. 5.2 (dashed line): its slope, smaller than both the unloading and the loading curves, provides the equivalent elastic modulus.

It must be point out that this equivalent model cannot be used to analyse the mechanical behaviour of a single coil which follows a single stress path during collaring. Indeed, it refers both to a multitude of coils and to a multitude of collarings of a single coil. The latter situation, which occurs when a same dipole is assembled several times with different pole shims, will be studied in the next Section.

5.3   Stresses and deformations of the collared coil

In order to verify the reliability of the finite element model of the collared coil and in particular the modeling of the collaring procedure by the definition of an equivalent elastic modulus, we compare the results of the numerical computations with the measurements performed on a dedicated experiment on a $1\,\mathrm{m}$ long prototype [57].

5.3.1   Experimental set-up

A $1\,\mathrm{m}$ long dipole magnet has been re-assembled five times with different pole shims. The shim thickness has been changed by $\pm\,0.15\,\mathrm{mm}$, for both layers. This variation has been done in the two apertures at the same time, keeping the left-right and top-bottom symmetries. Firstly, the nominal configuration with nominal shims has been assembled and measured. Then, the inner shims have been changed keeping the outer ones to the nominal value; finally, the same has been done for the outer layer, keeping nominal inner shims. For each of the five cases, the magnet has been assembled without the iron yoke and the shrinking cylinder; just the collared coil at ambient temperature has been studied.

Table 5.1: Shim thickness variation (mm) and corresponding pre-stress (MPa) for the inner and the outer layer, experimental data.

Δ shim		Pre-stress Ap. 1		Pre-stress Ap. 2	
(mm)		(MPa)		(MPa)	
Inner	Outer	Inner	Outer	Inner	Outer
+0.00	+0.00	49	51	44	60
+0.15	+0.00	67	49	62	60
−0.15	+0.00	30	51	28	60
+0.00	+0.15	50	72	46	79
+0.00	−0.15	52	32	49	39

The pre-stress during the collaring and the final pre-stress have been measured for the two apertures by mean of capacitive gauges located at coil poles. At the end of the collaring, also the vertical diameter of the collar has been measured.
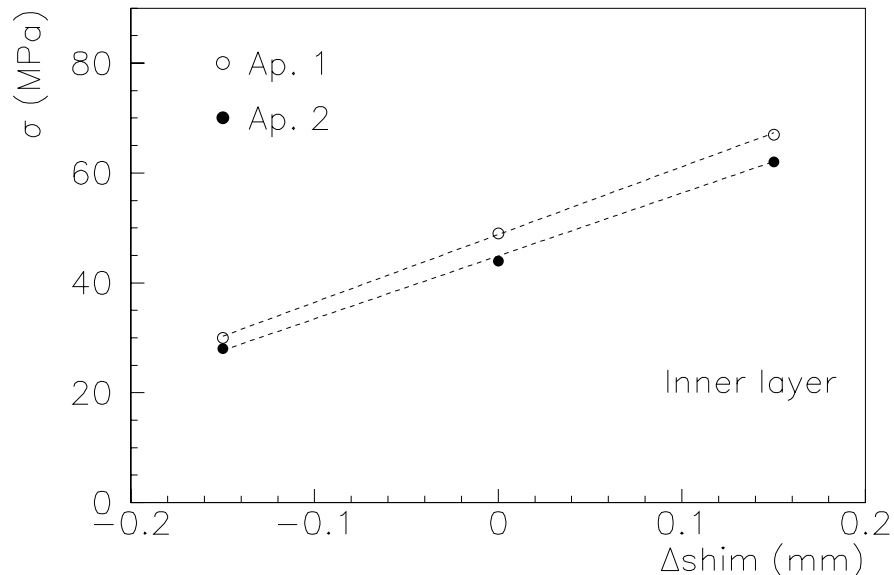
Figure 5.3: Pre-stress σ (MPa) versus shim thickness variation (mm) for the inner layer and for the two apertures (Ap. 1 and Ap. 2), experimental data and linear fit.

5.3.2 Results: model vs measurements

Correlation between pre-stress and shim thickness

In Tab. 5.1 we give the shim thickness variations and the measured azimuthal pre-stress of the collared coil in the two apertures. A variation of the shim dimension mainly affects the pre-stress of the corresponding layer: in fact a pre-stress variation of about 40 MPa in one layer determines a variation of the pre-stress in the other layer within 3 MPa. The same mechanical decoupling of the two layers is found in the finite elements model (cross-talk between the two layers lower than 10 %).

Pre-stress variations versus shim thickness of the same layer are linear, with similar slopes in the two apertures (see Fig. 5.3 and Fig. 5.4). From linear best fits one can see that a shim change of 0.1 mm induces a variation of the pre-stress of 12 to 13 MPa (see Tab. 5.2, row "Measurements").

As explained in Sect. 5.2, if we want to model the variation of the pre-stress induced by the modification of the shim thickness, we have to consider the complete stress path followed by the coil during collaring. In Fig 5.5 the values of the peak pre-stress and of the remaining pre-stress on the coil during the five collarings are plotted.

By analysing the data, it can be pointed out some dependence of the relaxation k on the peak stress. In fact, by fitting the stress measurements plotted in Fig 5.5,
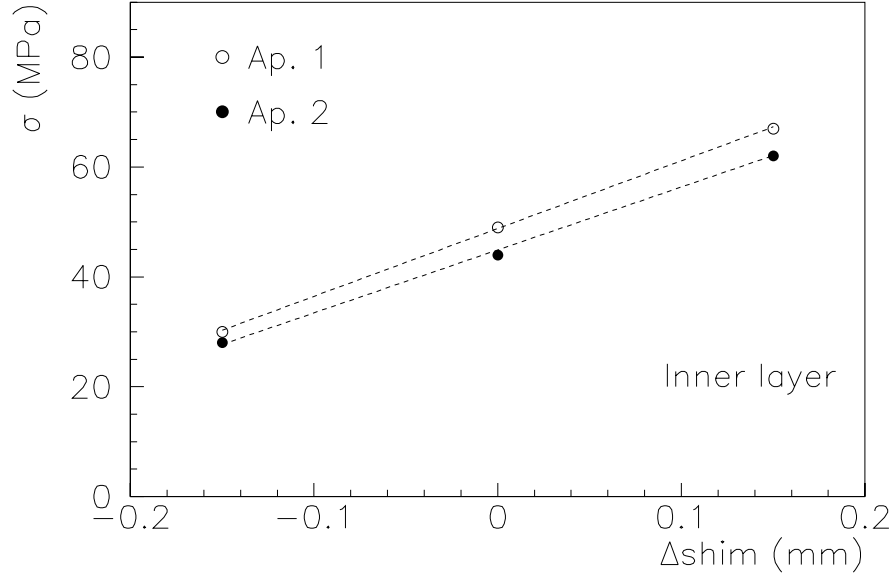
Figure 5.4: Pre-stress σ (MPa) versus shim thickness variation (mm) for the outer layer and for the two apertures (Ap. 1 and Ap. 2), experimental data and linear fit.

one obtains

$$\frac{\sigma_{coll}^{in}}{\sigma_{peak}^{in}} = k^{in} = 0.002\,\sigma_{peak}^{in} + 0.54 \tag{5.1}$$

and

$$\frac{\sigma_{coll}^{ou}}{\sigma_{peak}^{ou}} = k^{ou} = 0.002\,\sigma_{peak}^{ou} + 0.48 \tag{5.2}$$

where k^{in} and k^{ou} are the relaxations for the inner and the outer layer and σ_{peak}^{in} and σ_{peak}^{ou} the peak stresses in MPa reached during the collaring on the inner and the outer layer.

Table 5.2: Effect of a 0.1 mm thicker shim on the azimuthal pre-stress (MPa).

	Inner layer	Outer layer
Measurements	12 ± 1	13 ± 1
Finite element model (E_{eq})	12	10
Finite element model (E_{un})	25	25

Using the relaxations k^{in} and k^{ou} an equivalent elastic modulus E_{eq} can be derived from the post-processing of the stress-displacement curves of the coil (see Sect. 5.2 and we obtain
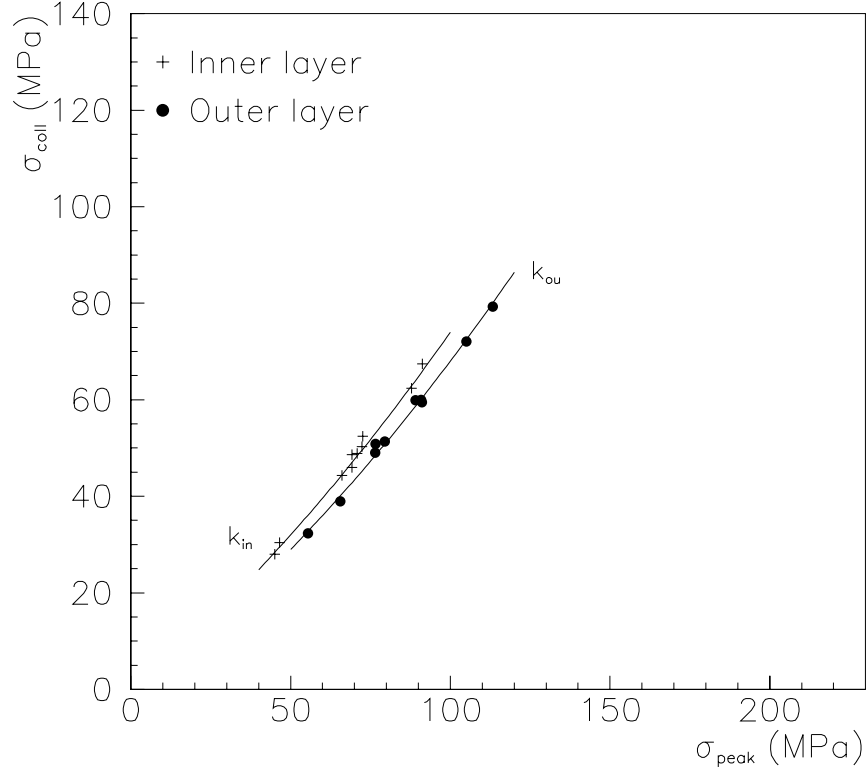
Figure 5.5: Measured relaxation during five collarings of the 1 m long prototype: experimental data (markers) and fit (solid lines).

$$E_{eq}^{in} = 5500 \quad \text{MPa} \qquad E_{eq}^{ou} = 5100 \quad \text{MPa} \tag{5.3}$$

respectively for the inner and the outer layer.

We implemented these coil equivalent elastic moduli in the finite element model and we computed the effect of a 0.1 m thicker shim. The model provides the same result for the inner layer, whilst underestimates the outer layer of about 3 MPa (see Tab. 5.2). This may be due to a slightly different mechanical behaviour between conductor stacks, that have been used to work out equivalent elastic modulus, and conductor arcs. Most likely, the outer layer is more sensitive to this effect, since it features blocks with a higher number of conductors.

Indeed, one can point out that if the unloading elastic modulus E_{un} at 70 MPa (around 12 GPa) had been used, we would have obtained a sensitivity of 25 MPa. This proves that the approach of the equivalent elastic moduli is necessary for a correct modeling of the stresses in the collared coil.
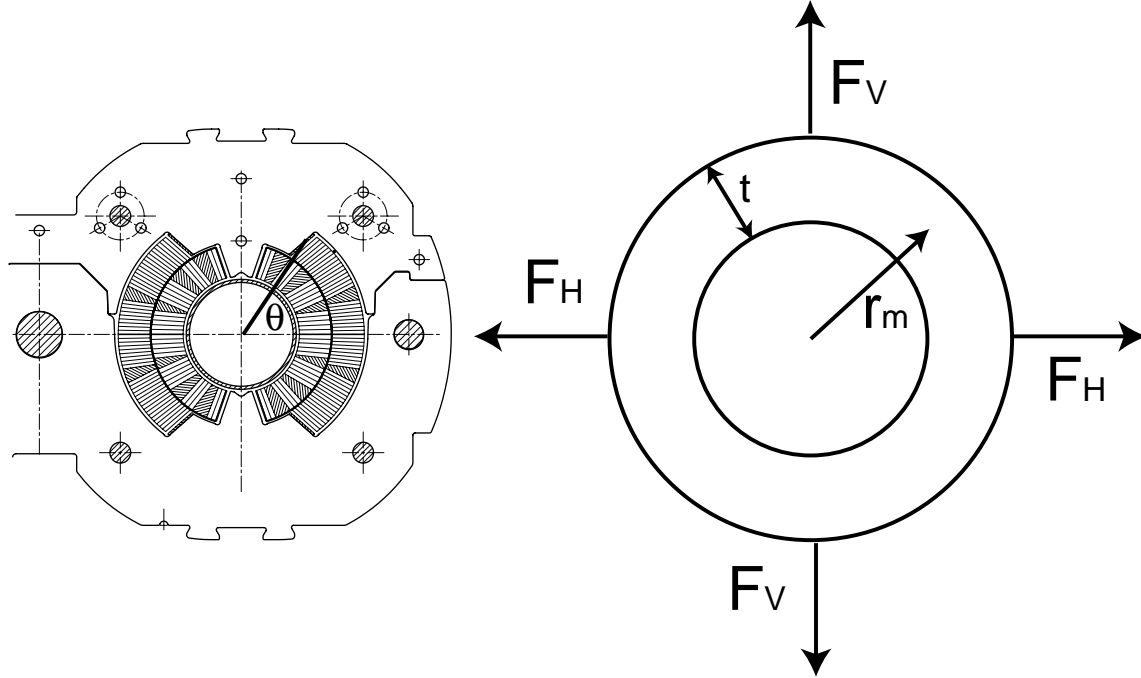
Figure 5.6: Simplified model of the collar (right) and collared coil (left).

Correlation between pre-stress and collar deformation

The pre-stress that compresses the coil has also the effect of deforming the collars. The impact of the pre-stress on the collar cavity can be described in a first approximation by a vertical deflection (*ovalisation*), which increases the vertical diameter of the collar cavity keeping unchanged the horizontal one. This variation of the vertical diameter is linked to the rigidity of the collars, that is a combined effect of the collar material (stainless steel) and of its geometry.

   The vertical deflection of the collars has been measured in the five collared coils, obtaining a estimation of the correlation between pre-stress and collar deformation. In this Section we compare the experimental data with the results of a simplified analytical model and of the finite element model.

   We want to evaluate with a simple analytical computation the variation of the vertical dimension of the collar induced by an increase of the pre-stress of 10 MPa. We assume that the collar behaves as a ring (see Fig. 5.6) of a medium radius $r_m = 81.1$ mm, a thickness $t = 40.2$ mm, a width $b = 1$ mm and an elastic modulus $E = 195000$ MPa. As explained in [58], the increase of the vertical diameter δ_1 determined by a vertical force F_V is given by

$$\delta_1 = \left(\frac{\pi}{4} - \frac{2}{\pi}\right) \frac{F_V r_m^3 12}{E t^3 b}. \tag{5.4}$$

On the other hand, the decrease of the vertical diameter δ_2 determined by a horizontal force F_H is given by

$$\delta_1 = \left(\frac{2}{\pi} - \frac{1}{2}\right) \frac{F_H r_m^3 12}{Et^3 b}. \tag{5.5}$$

In our case, the vertical force is

$$F_V = \Delta\sigma_\theta n_c s_c b = 620 \quad \text{N}, \tag{5.6}$$

where $\Delta\sigma_\theta = 10$ MPa is the increase of azimuthal pre-stress, $n_c = 4$ is the number of coil layers and $s_c = 15.4$ mm is the coil layer thickness. The horizontal force instead is given by

$$F_H = 2\left(\Delta\sigma_r r_i \theta b\right) = 370 \quad \text{N}, \tag{5.7}$$

where we assumed that the increase of the radial stress of the coil on the collar is

$$\Delta\sigma_r = 0.3\Delta\sigma_\theta = 3.3 \quad \text{MPa}, \tag{5.8}$$

while $r_i = 61$ mm is the collar inner radius and $\theta = 0.91$ rad is the angle of the coil outer layer. By adding Eq. (5.4) and Eq. (5.5) we obtain the total variation of the diameter

$$\delta = \delta_1 - \delta_2 = \frac{F_V}{K} \tag{5.9}$$

being

$$K = \frac{Et^3 b}{0.81 r_m^3} = 29300 \quad \frac{\text{N}}{\text{mm}} \tag{5.10}$$

the vertical rigidity of the collars.

Table 5.3: Effect of an increase of 10 MPa of the average pre-stress on the collar vertical dimension.

	Δ diameter (mm)
Measurements	0.036 ± 0.006
Analytical model	0.042
Finite element model	0.037

If now we compute the vertical deflection of the collar we have to take into account the fact that the vertical force is exerted only on the long collar: therefore the variation of the vertical diameter of the collar due to an increase of 10 MPa of pre-stress is

$$\delta = \frac{2F_V}{K} = 0.042 \quad \text{mm}. \tag{5.11}$$

The results of the analytical model have been compared with the numerical computation obtained by the finite element model, where the complete geometry of the collar has been implemented, and with the experimental measurements of the vertical dimension of the collars performed on the short dipole after the five collarings (see Tab. 5.3).

It can be noticed that both the simplified analytical model and the finite element model provide an evaluation of the collar deflection consistent with the experimental measurements.

5.4   Stresses and deformations of the assembled cold mass

The *yoking* is the procedure by which the two halves of the yoke are closed around the collared coil (see Sect. 2.2.5). This operation consists in the welding of the shrinking cylinder with a tangential stress of about 150 MPa in order to close the gap between the yoke halves.
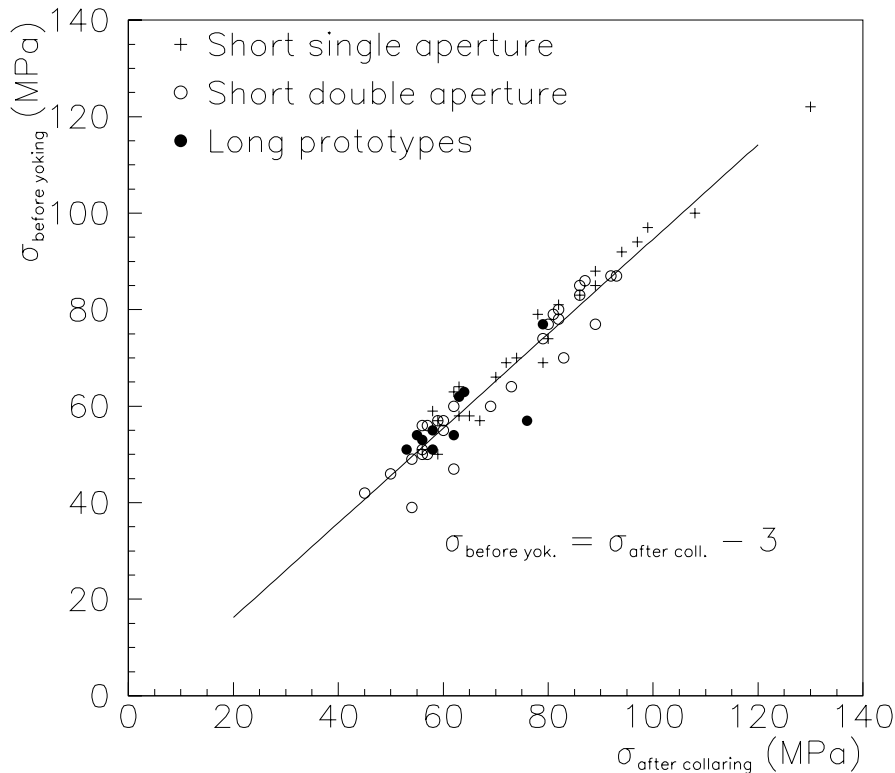
Figure 5.7: Coil pre-stress before yoking vs coil pre-stress after collaring: experimental data (markers) and linear fit (solid line).

The yoking procedure follows the collaring procedure with a delay which varied from several day for the short dipoles [59] to about one month for the long prototypes and the pre-series dipoles [60]. During this period, a small reduction of the coil pre-stress due to coil insulation creep is observed. In Fig 5.7 we plot the pre-stress measured just before the yoking versus the pre-stress measured after the collaring (see Tab. C.1, Tab. C.2 and Tab. C.3 for the data): the experimental measurements can be fitted by the straight line and show a decrease of pre-stress of $3 \pm 5\,\mathrm{MPa}$ (error of $2 \times$ the standard deviation).
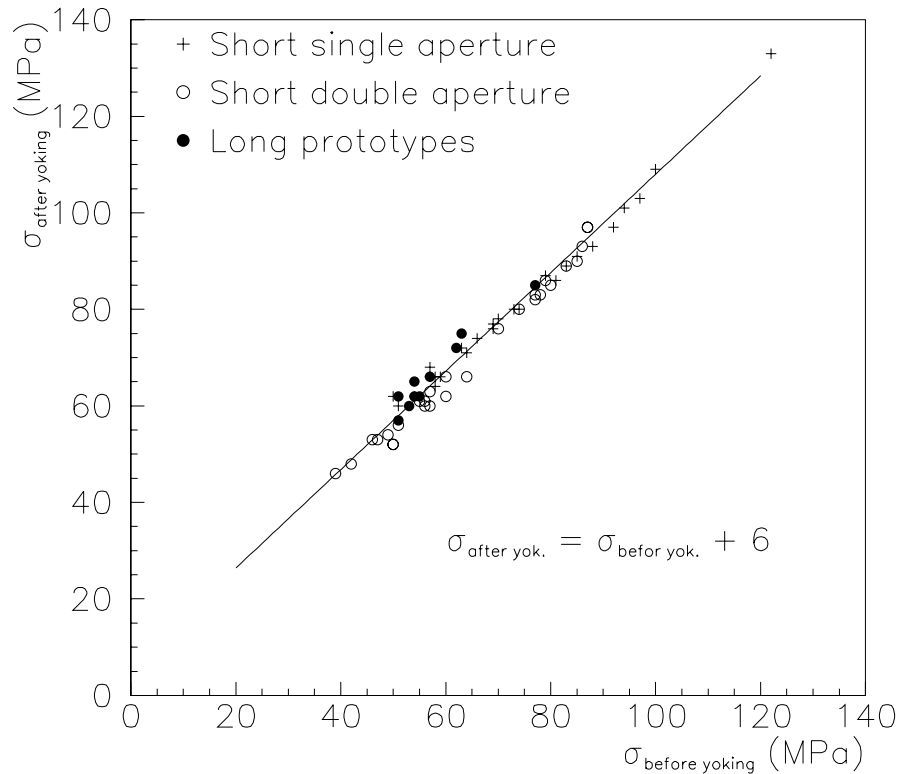
Figure 5.8: Measured increase of pre-stress during yoking: experimental data (markers) and linear fit (solid line).

The assembling of the yoke determines an increase of the pre-stress: in Fig 5.8 we plot the pre-stress measured after the yoking versus the pre-stress measured before the yoking (see Tab. C.1, Tab. C.2 and Tab. C.3 for the data). Also in this case the data are well fitted by a straight line and show an increase of the pre-stress of $6 \pm 3\,\mathrm{MPa}$ (error of $2 \times$ the standard deviation).

5.4.1   Results: model vs measurements

The effect of the yoke has been studied by the finite element model: the yoke and the cylinder have been added to the model of the collared coil and a stress of 150 MPa has been imposed to the cylinder. In this case it has been implemented the coil elastic modulus measured on the unloading curve, that is 13 GPa for the inner layer and 12 GPa for the outer layer (see Sect. 3.2.4). In fact the coil, as explained in Sect. 3.2.2, when compressed until a peak pressure and then partially unloaded, follows during the re-loading cycle the unloading curve until it reaches the peak pressure of the previous loading phase. The computed increase of the pre-stress during yoking is of 4 MPa, in agreement with the experimental measurements.

Table 5.4: Increase of coil pre-stress (MPa) during yoking.

	Δ pre-stress (MPa)
Measurements	6 ± 3
Finite element model	4

Chapter 6

Mechanical behaviour of the dipole at 1.9 K

We now study the mechanical behaviour of the dipole at 1.9 K. In particular we analyse the coil pre-stress losses that occur during cool-down from ambient temperature to the nominal temperature of 1.9 K.

6.1 Pre-stress loss experimental data

In Fig. 6.1 we plot the pre-stress losses measured from the collared coils at 293 K to the assembled cold mass at 1.9 K just before the ramp-up of the magnet (see Tab. C.1, Tab. C.2 and Tab. C.3 for the data). We do not consider the pre-stress at 293 K in the assembled cold mass. In fact during the cool-down the yoke shrinks more than the collars because of the higher thermal contraction coefficient; hence the small additional effect on the pre-stress induced by the yoke at ambient temperature is expected to disappear at 1.9 K.

The pre-stress loss, measured in several 1 m long prototypes and 15 m long prototypes, can be fitted by a linear equation

$$\sigma_c = 0.5\,\sigma_w - 9 \qquad \text{MPa} \tag{6.1}$$

where σ_c and σ_w are respectively the pre-stress of the collared coils at 293 K and the pre-stress of the assembled cold mass at 1.9 K. The experimental data are within a range of ± 5 MPa with respect to the linear fit, with a level of confidence of 95 %.

The similarity of the pre-stress losses observed in both long and short models, and both single and double aperture magnets, suggests that this effect should be mainly due to the thermo-mechanical properties of the coil and of the collars.
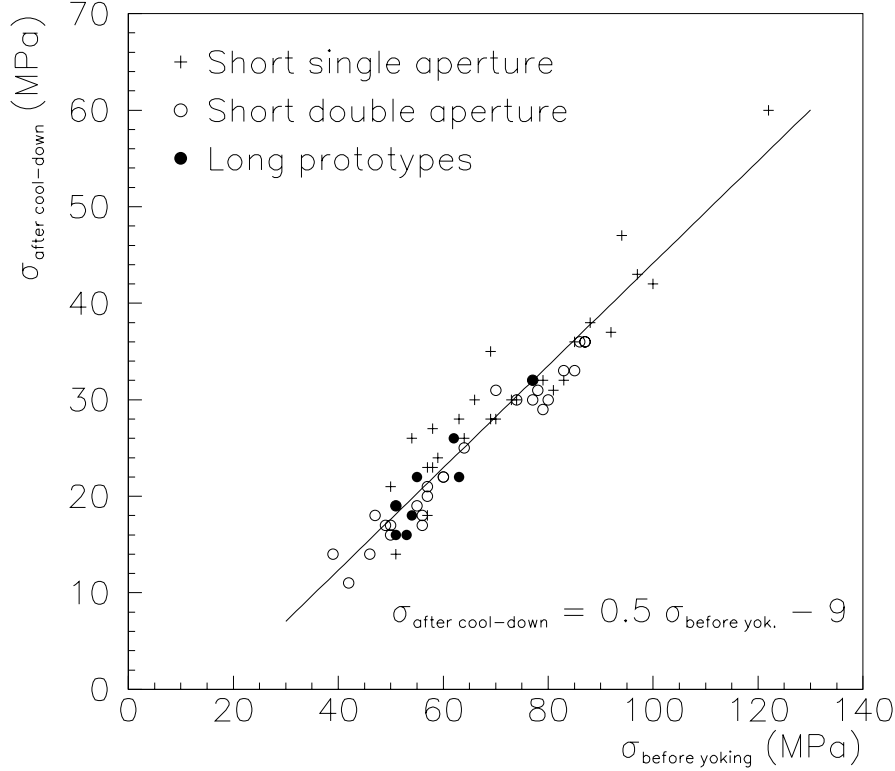
Figure 6.1: Coil pre-stress after cool-down vs coil pre-stress before yoking: experimental data (markers) and linear fit (solid line).

6.2   Pre-stress loss equation

The pre-stress loss from ambient to cryogenic temperature can be studied with the equation used to evaluate the thermal contraction coefficient of the conductor stack (see Sect 3.4.1).

Let us consider the coil closed in a infinitely rigid collar, under a pre-stress σ_w at 293 K. If the whole system is cooled down at 1.9 K, the difference in the coil deformation $\epsilon_w - \epsilon_c$ between 293 K and 1.9 K is equal to the difference in the integrated thermal contraction coefficients of the coil α_b and of the collar α_c:

$$\epsilon_w - \epsilon_c = \alpha_b - \alpha_c. \tag{6.2}$$

Using a linear relation between deformation and stress of the coil, that is $\epsilon_{wb} = \sigma_w/E_{wb}$ and $\epsilon_{cb} = \sigma_c/E_{cb}$, where E_{wb} and E_{cb} are the elastic moduli of the coil at 293 K and 1.9 K respectively, we obtain

$$\frac{\sigma_w}{E_{wb}} - \frac{\sigma_c}{E_{cb}} = \alpha_b - \alpha_c. \tag{6.3}$$

which gives the well-known [19, 62] equation for the pre-stress loss

$$\sigma_c = \frac{E_{cb}}{E_{wb}} \left[\sigma_w - E_{wb}(\alpha_b - \alpha_c) \right]. \tag{6.4}$$

If we consider also the deformation of the collars, Eq. (6.3) becomes

$$\frac{\sigma_w}{E_{wb}} + \frac{\sigma_w}{E_{wc}} - \frac{\sigma_c}{E_{cb}} - \frac{\sigma_c}{E_{cc}} = \alpha_b - \alpha_c. \tag{6.5}$$

where E_{wc} and E_{cc} are the elastic moduli of the collar cavity at warm and cold temperature respectively. The Eq (6.4) can thereafter be generalised in

$$\sigma_c = \frac{\dfrac{1}{E_{wb}} + \dfrac{1}{E_{wc}}}{\dfrac{1}{E_{cb}} + \dfrac{1}{E_{cc}}} \sigma_w - \frac{\alpha_b - \alpha_c}{\dfrac{1}{E_{cb}} + \dfrac{1}{E_{cc}}}. \tag{6.6}$$

6.2.1 Elastic modulus of the collar cavity

We refer to the analytical evaluation of the vertical rigidity of the collar presented in Sect. 5.3.2 in order to define the elastic moduli of the collar cavity E_{wc} and E_{cc}. We found that the vertical rigidity of the collar submitted the vertical and horizontal forces resulting from the coil azimuthal pre-stress is $K = 29300$ N. Moreover we computed analytically that an increase of pre-stress of $\Delta\sigma_w = 10$ MPa determines a variation of the vertical radius of the collar of $\Delta l = 0.021$ mm.

The deformation of the collar cavity can be expressed as

$$\epsilon_{wc} = \frac{\Delta l}{l} = \frac{\Delta l}{r_i \theta} \tag{6.7}$$

being $r_i = 61$ mm is the collar inner radius and $\theta = 0.91$ rad is the angle of the coil outer layer. The elastic modulus of the collar cavity can be computed as

$$E_{wc} = \frac{\Delta\sigma_w}{\epsilon_{wc}} \approx 26400 \qquad \text{MPa}. \tag{6.8}$$

Since the austenitic steel features a negligible increase of the elastic modulus from 293 K to 1.9 K, we assume $E_{wc} = E_{cc}$.

6.2.2 Elastic modulus and thermal contraction coefficient of the coil

In Sect. 3.4.3, we described the measurement of the pre-stress losses of the inner and outer layer stacks closed in steel mould, induced by a cool-down from ambient temperature to 77 K. Pre-stress losses (σ_c, σ_w) provide through Eq.(6.6) the integrated thermal contraction α_b for a given choice of the elastic moduli E_{wb} and E_{cb}.
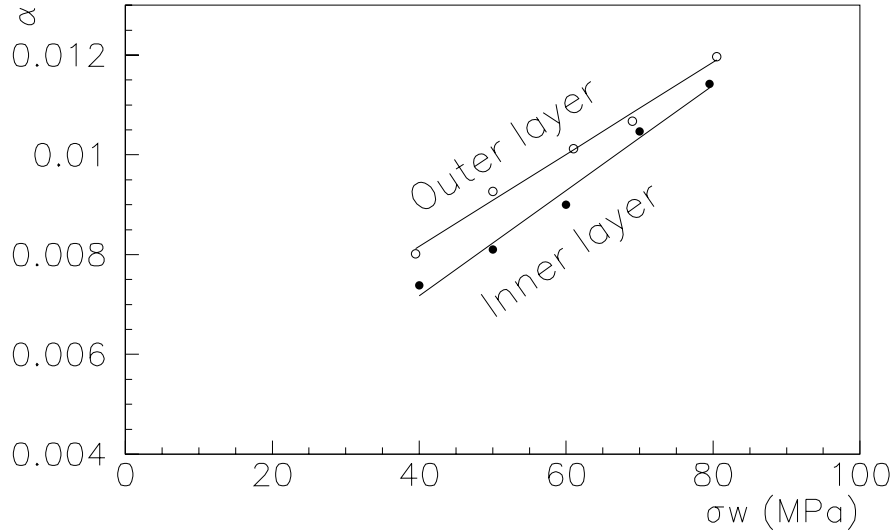
Figure 6.2: Integrated thermal contraction coefficient α versus stress σ_w at 293 K for the inner and outer layer stack.

In the case of the stacks, we implemented in the pre-stress loss equation the strain of the stack at ambient temperature ϵ_{ws} as the difference between the stack height at 0.4 MPa on the loading curve and the height on the unloading curve at σ_w. At cryogenic temperature the strain ϵ_{cs} was computed in the same way.

In this Section instead, we are interested in the modeling of the pre-stress losses of all the measured dipoles (see Fig. 6.1). During collaring each dipole followed a different stress path. As explained in Sect. 5.2, when we consider a multitude of dipoles the mechanical behaviour at 293 K must be described by the equivalent elastic modulus at 293 K E_{weq}. Therefore, this equivalent modulus must substitute E_{wb} in Eq.(6.6).

Concerning E_{cb}, since the elastic modulus at 77 K depends on the pressure (see Sect. 3.3.3) we decided to use the elastic modulus at $\sigma_c = 37$ MPa, that is the pre-stress reached at 77 K by the stack with a pre-stress of $\sigma_w = 70$ MPa at ambient temperature (see Tab. 3.5). In fact, we will use the average between loading and unloading elastic modulus, choosing $E_{cb} = 6.5$ GPa for both stacks.

Using these elastic moduli, we can evaluate the integrated thermal contraction factor α_b through Eq. (6.6). We find a linear dependence of α_b on the stress σ_w, obtaining values of α_b that range from 0.006 to 0.011 (see Fig. 6.2). The experimental data are fitted by

$$\alpha_b(\sigma_w) = \alpha_{b0} + \alpha_{b1}\sigma_w. \tag{6.9}$$

The coefficients of the linear fit for the inner and the outer layer are given in Tab. 6.1. An increase of 10 % in α_b has been applied to extrapolate these measurements from

77 K to 1.9 K.

Table 6.1: Coefficients of the linear fit of Eq. (6.9) for the inner and outer layer.

	α_{b0}	α_{b1}
Inner layer	3.00	0.09
Outer layer	4.50	0.09

6.3   Finite element modeling of the pre-stress loss

We present now the computation of the pre-stress loss performed by the finite element model of the dipole cross-section. A problem met during the modeling consisted in the dependence of the thermal contraction factor on the pre-stress expressed by Eq. (6.9), that cannot be included in the finite element code ANSYS^{TM}. Nevertheless, the dependence of the thermal contraction on the pre-stress can be included in the pre-stress loss equation. If we consider the simplified case of an infinitely rigid collar, we obtain

$$\sigma_c = \frac{E_{cb}}{E_{weq}} \left[\sigma_w - E_{weq}(\alpha_{b0} + \alpha_{b1}\sigma_w - \alpha_c) \right]. \tag{6.10}$$

One can group the dependence of α_b on σ_w to the term that accounts for coil elasticity at cold

$$\sigma_c = \frac{E_{cb}}{E_{weq}} \left[\sigma_w(1 - \alpha_{b1}E_{weq}) - (\alpha_{b0} - \alpha_c)E_{weq} \right]. \tag{6.11}$$

The above equation can be cast in the form

$$\sigma_c = \frac{E_{ceq}}{E_{weq}} \left[\sigma_w - (\alpha_{eq} - \alpha_c)E_{weq} \right] \tag{6.12}$$

where we defined a coil equivalent elastic modulus at 77 K E_{ceq} according to

$$E_{ceq} = E_{cb}(1 - \alpha_{b1}E_{weq}) \tag{6.13}$$

and an equivalent thermal contraction coefficient α_{eq} according to

$$\alpha_b^e = \alpha_c + \frac{\alpha_{b0} - \alpha_c}{1 - \alpha_{b1}E_{weq}}. \tag{6.14}$$

Now, the thermal contraction of the coil does not depend on the pressure and therefore can be used in the finite element code. The same formalism can be used without assuming an infinitely rigid collar cavity: numerical values derived for α_{eq} and E_{ceq} are given in Tab. 6.2. The analytical model with a stress-dependent $\alpha_b(\sigma_w)$ has been compared to the implementation in a finite element model using these equivalent properties, finding an excellent agreement.
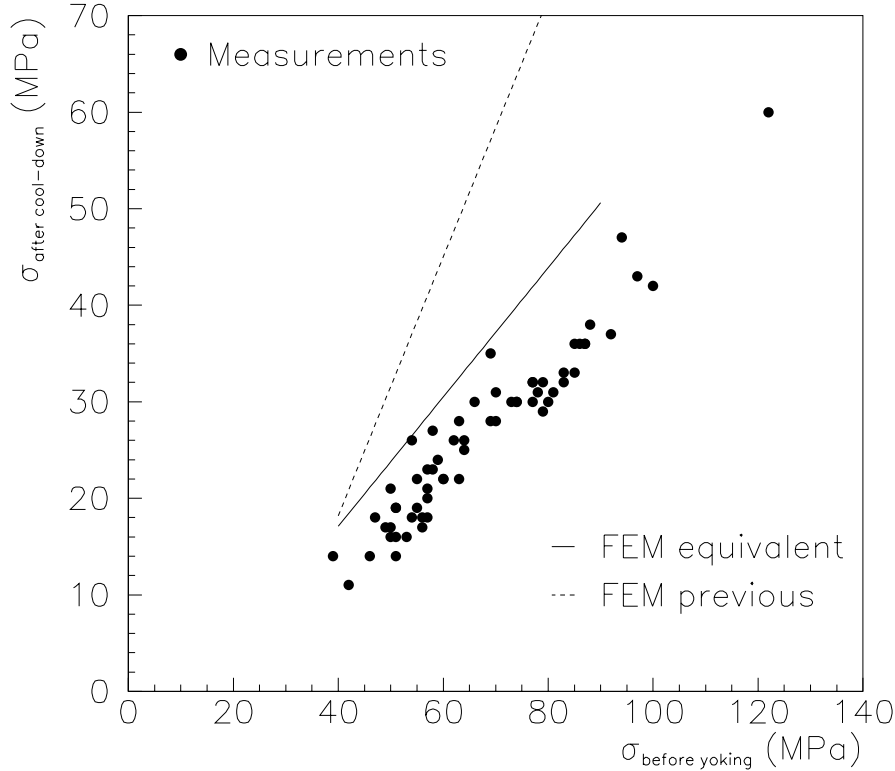
Figure 6.3: Pre-stress (MPa) loss evaluated by the FEM with equivalent coil properties (solid line) and with the previous model (dashed line): comparison with experimental measurements.

6.3.1   Results: model vs measurements

In Fig. 6.1 we compare the experimental measurements of the pre-stress loss (markers) with the results of the FEM where we have been implemented the coil equivalent material properties α_{eq} and E_{ceq} (solid line). The model overestimates the pre-stress at 1.9 K of 3 to 8 MPa in the validity range of our linear approximation (40 to 80 MPa at 293 K). This can be compared to a dispersion of the data around the best fit of 5 MPa (2 × the standard deviation) in σ_c. This agreement can be considered satisfactory for numerical predictions. We point out that a model that simply assumes a ratio E_c/E_w equal to 1.5 (i.e., the usual hardening ratio) and a coil integrated thermal contraction coefficient of about $6 \cdot 10^{-3}$ [13] (the dashed line in Fig. 6.1) would predict a slope of the (σ_c, σ_w) line of about 1.3 against a measured value of 0.53. On the other hand, the slope obtained by the finite element model with the equivalent material properties is consistent with the experimental data. We conclude that the difficulty of modeling the pre-stress loss in the dipole (the same difficuly was found in the SSC dipole [16]) can be overcome taking into account the particular behaviour

Table 6.2: Equivalent thermal contraction and equivalent elastic modulus (GPa) for the inner and outer layer.

	Inner	Outer
E_{cb}^e	2.9	3.0
α_b^e	0.0038	0.0066

of the coil during the cool-down. The result obtained by the FEM with equivalent properties represents a step ahead in the comprehension of the old problem of the coil pre-stress losses.

Chapter 7

Magnetic behaviour of the dipole at 293 K

As the last step of the prototype phase for the finalisation of the LHC main dipole design, 5 full-scale dipole prototype collared coils with austenitic steel collars were built by three European firms and then assembled into cryo-dipole at CERN. This prototype program started in 1998 and was completed in 2000 [64]. In November 1999, CERN has placed a first order of 3×30 dipole cold masses. These so-called pre-series dipoles will be installed in the LHC tunnel. At this moment (November 2001), 15 collared coil have been build and tested at ambient temperature. Among them, 6 complete cold masses have been assembled and measured at warm temperature.

Here we focus our analysis on the effect of the coil deformations at ambient temperature (discussed in Chapt.5) on the magnetic field produced by the dipole. We start describing how we implement in the magnetic model the deformations computed by the finite element model. Then we present an analysis of the effect on the field harmonics of the mechanical tolerances and of the collar shape. Finally we present the magnetic measurements performed on the collared coil at 293 K and we explain the differences between the expected field harmonics and the experimental data from the prototypes and from the pre-series magnets. Possible corrective strategies for the field errors are discussed. We also discuss the effect of the coil deformations induced by the yoking on field harmonics at ambient temperature.

7.1 Modeling of the effect of coil deformations on magnetic field

In order to study the magnetic effect of the mechanical deformations, we use the following tools:

- a finite element model to compute the field of deformations on the superconducting coil;

- a Fortran code (ANSIA [63]) to provide the displaced coordinates for each conductor of the dipole coil;

- a magneto-static model of the dipole coil, implemented in the code ROXIE [7], to evaluate the magnetic field and its multipolar expansion.

Since the finite element model only considers one quarter of the dipole cross-section, i.e. half coil, the displacements implemented in the magneto-static code present an up-down symmetry that only allows normal multipole (see Sect. 2.2.3).

7.1.1   Effect of the shape of the collar cavity on magnetic field

A typical analysis that can be performed with this mechanical-magnetic model regards the effect on the magnetic field of the collar cavity shape [65]. This analysis is aimed to explore the change of the collar cavity or the insertion of shims between the collars and the coil as possible corrective strategy for the field quality. Moreover, it allows investigating how the fabrication tolerance of the collars affects the field harmonics. These are not trivial tasks, since any variation of the components which surround the coil has an impact on the stresses and the deformations of the conductor blocks. In particular, the pre-stress of the coil must be controlled: one has to avoid pre-stress variations larger than ± 15 MPa with respect to the nominal value of 75 MPa, in order to preserve the optimal stress.
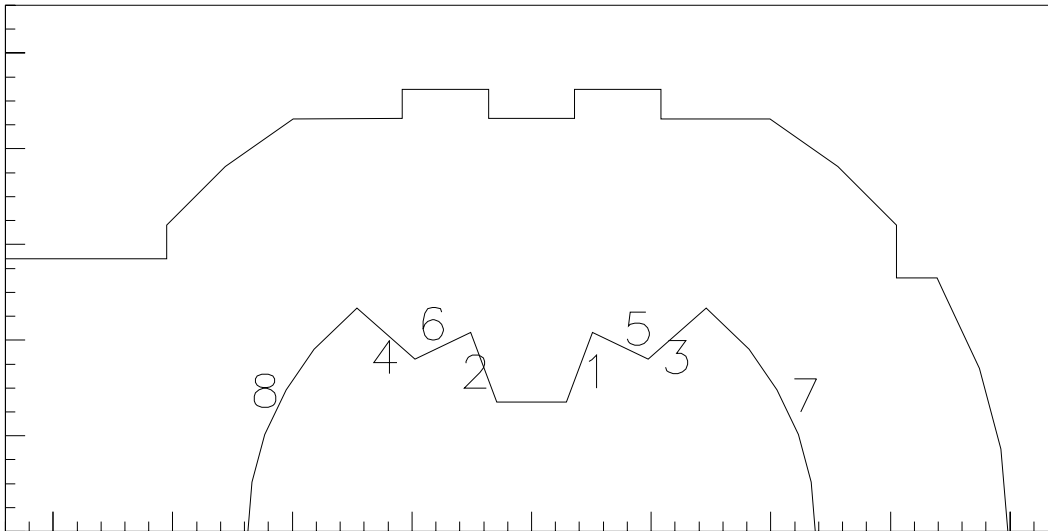
Figure 7.1: Schematic representation of the one-half collar: the numbers indicate the area changed in the sensitivity analysis.
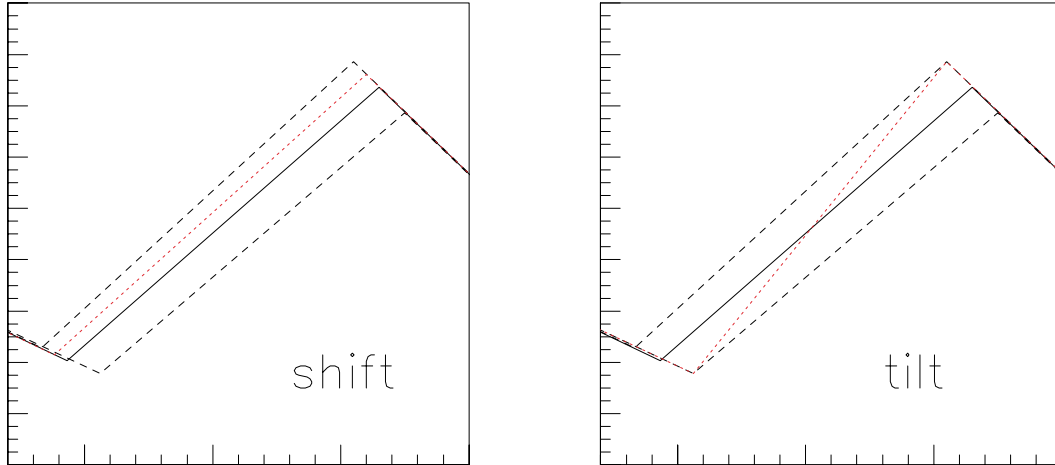
Figure 7.2: Positive collar shift and positive collar tilt.

We applied the modifications in the regions indicated in Fig. 7.1 in the following way:

- we assume that straight lines of the design are preserved and only the end-points of each segment can be displaced in the same direction (line shift) or in opposite direction (line tilt), see Fig. 7.2;

- when arcs of circumference are considered, we assume that the circular shape is preserved and that only the arc end-points can move in the same direction (shift) or in the opposite direction (tilt);

- shifts are considered positive when in this way components to which shift is applied result smaller, while tilts are considered positive when the rotation is counter clockwise on the right part of the aperture and clockwise on the left part.

An estimate of the sensitivity to these modifications is give in Tab. 7.1 and in Tab. 7.2 where the variation of the field harmonics, from the b_2 to the b_9, and of the pre-stress are quoted for a shift or a tilt of 0.1 mm respectively, in the appropriate area. For example, we can see that an increase of the pole shim of 0.1 mm in the right and left side of the inner layer (Region 1 and Region 2) determines a variation of the sextupole respectively of $+0.90$ units and $+0.98$ units, with an increase of the pre-stress of 12 MPa on both layers.

Tab. 7.1 and Tab. 7.2 constitute a powerful tool to study how manufacturing errors affect the field quality. Moreover, they can be used to predict the corrective action on field harmonics induced by collar shape modification or by change of shim dimension.

Table 7.1: Effect of a shift and of a tilt of 0.1 mm of the collar cavity on field harmonics (10^{-4} units, $R_{ref} = 17$ mm) for the collared coil at ambient temperature.

	Shift							
Region	Δb_2	Δb_3	Δb_4	Δb_5	Δb_6	Δb_7	Δb_8	Δb_9
1	+2.35	+0.90	−0.16	−0.15	+0.05	+0.06	−0.01	−0.03
2	−2.33	+0.98	+0.16	−0.14	−0.05	+0.06	+0.01	−0.02
3	+1.65	+0.70	+0.12	−0.03	−0.03	−0.01	+0.00	+0.00
4	−1.61	+0.76	−0.12	−0.02	+0.03	−0.01	+0.00	+0.00
5	+0.24	+0.62	+0.17	−0.13	−0.10	+0.01	+0.03	+0.00
6	−0.25	+0.58	−0.17	−0.13	+0.09	+0.01	−0.03	+0.00
7	−3.69	−0.61	+0.17	+0.10	+0.02	+0.00	−0.01	−0.01
8	+3.61	−0.68	−0.17	+0.08	−0.01	−0.01	+0.01	−0.01
	Tilt							
Region	Δb_2	Δb_3	Δb_4	Δb_5	Δb_6	Δb_7	Δb_8	Δb_9
1	−0.66	−0.58	−0.07	+0.20	+0.12	−0.02	−0.05	−0.01
2	+0.57	−0.56	+0.06	+0.21	−0.12	−0.02	+0.05	−0.01
3	−0.28	−0.25	−0.08	+0.02	+0.03	+0.00	−0.01	+0.00
4	+0.21	−0.23	+0.07	+0.03	−0.03	+0.00	+0.00	+0.00
5	+0.18	+0.47	+0.14	−0.10	−0.07	+0.01	+0.02	+0.00
6	−0.19	+0.45	−0.13	−0.10	+0.07	+0.01	−0.02	+0.00
7	−1.37	−1.56	−0.84	−0.24	−0.05	−0.04	−0.03	−0.01
8	+1.49	−1.65	+0.86	−0.24	+0.05	−0.04	+0.04	−0.02

7.1.2 Effect of the mechanical tolerances on magnetic field

Another analysis that can be performed is a MonteCarlo analysis of the effect of the coil and collar tolerances of fabrication on multipoles [19]. We evaluated 100 different mechanical structures within tolerances (collars and coils randomly varied) using the finite element model. We generate 100 different geometries, considering error realisations with a Gaussian distribution truncated at $3 \times \sigma$, where $3 \times \sigma$ is set as the nominal tolerances. For each geometry we evaluate the stresses and the deformations of the coil and we transfer the conductor displacements to the magnetic model in order to compute the multipoles.

Results: model vs measurements

In Fig. 7.3, the computed standard deviation σ of the normal harmonic b_n is drawn in a semilogarithmic scale as a function of the normal harmonic number n. In the same plot there are also the standard deviations of the normal harmonics measured along the axis of the 15 m long dipole prototype MBP2N1. A good agreement between the

Table 7.2: Effect of a shift and of a tilt of 0.1 mm of the collar cavity on on the coil pre-stress (MPa) for the collared coil at ambient temperature.

	Shift			
Region	In right	In left	Out right	Out left
1	+12	+0	−1	+0
2	+0	+12	+0	−1
3	+0	+0	+10	+0
4	+0	−1	+0	+10
5	−3	+0	+1	+0
6	+0	−3	+0	+1
7	−12	+0	−8	+1
8	+0	−12	+1	−7
	Tilt			
Region	In right	In left	Out right	Out left
1	−1	+0	+0	+0
2	+0	−1	+0	+0
3	+0	+0	−1	+0
4	+0	+1	+0	−1
5	−2	+0	+0	+0
6	+0	−2	+0	+1
7	+3	+0	−1	+0
8	+0	+3	+0	−1

measured values and the estimates through the MonteCarlo is obtained: we conclude that the spread of multipoles along the axis of one dipole is mainly determined by the mechanical tolerances of the dipole components. A detailed analysis of the variation of the field harmonics along the magnet axis can be found in Ref. [61].

7.2   Magnetic measurements of the collared coil

We analyse the magnetic measurements performed at 293 K on the collared coil of the 5 prototypes and of 15 dipoles of the pre-series production. Measurements are carried out in both the apertures at 293 K with a low current (12 A). In Tab. D.1 and Tab. D.3 we give the averages along the straight part: 20 measurements are kept along the magnet axis, but the first and the last ones are discarded because of the effect of the coil ends. Data are given in units of 10^{-4} with respect to the main field at a reference radius of 17 mm. For the prototypes the average over the two apertures is presented.

Before analysing the magnetic measurements, we must take into account the
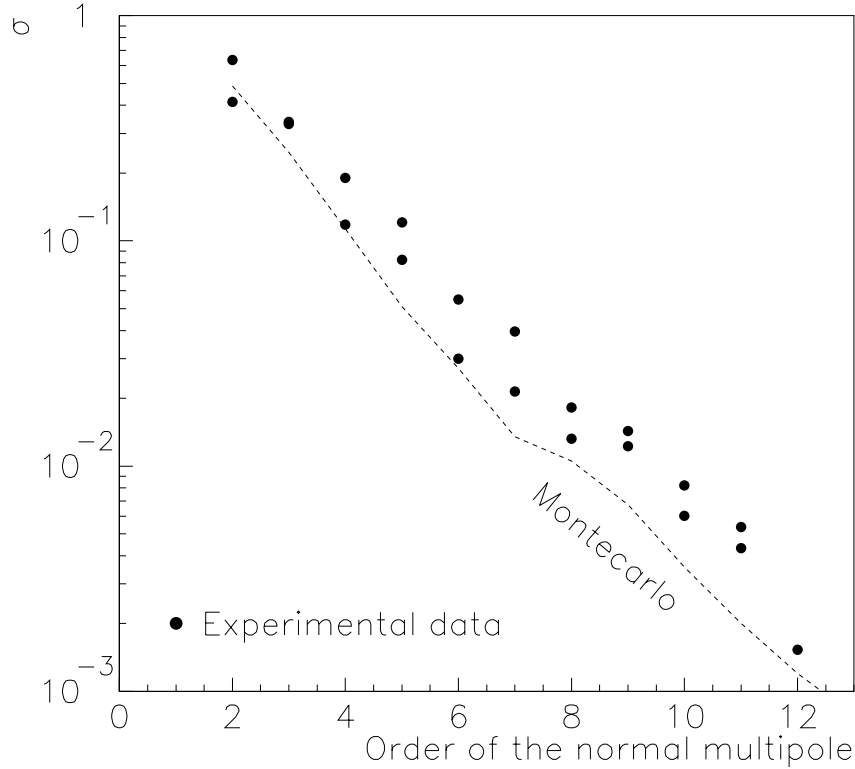
Figure 7.3: Experimental standard deviation of normal multipoles σ_n versus multipole order n for the dipole prototype MBP2N1 (dots) and MonteCarlo estimates (dashed line).

mechanical difference among the dipoles and in particular the pole shim thickness and the pre-stress.

7.2.1 Correlation between field harmonics and pole shim thickness

The five prototypes and some of the pre-series dipole have been built with pole shims with a thickness different from the nominal, in order to optimise the azimuthal pre-stress that is imposed to the coil during manufacturing. Different pole shim thicknesses have therefore given rise to different azimuthal coil lengths and to a variation of the odd multipoles. We computed with the magneto-static code the correlation between the multipoles and the coil azimuthal length (see Tab. 7.3), for a given collar cavity, i.e. for a given pre-stress, and at ambient temperature.

Table 7.3: Effect of a reduction of 0.1 mm of the azimuthal coil length on odd multiples (10^{-4} units, $R_{ref} = 17$ mm) computed with the magneto-static model for the collared coil at ambient temperature.

	Inner layer	Outer layer
Δb_3	+2.18	+1.62
Δb_5	−0.40	−0.08
Δb_7	+0.15	−0.02

7.2.2 Correlation between field harmonics and pre-stress

Another parameter to be considered is the coil azimuthal pre-stress, which may vary from magnet to magnet. The pre-stress imposed on the coil deforms the cavity of the collars and therefore modifies the coil shape and its multipolar content. Dipole with the same pole shim but with different coil size feature different pre-stress. Therefore, for a given pole shim thickness, collar cavities can be differently deformed.

The effect of collar deformations on field quality has been evaluated using the finite element code and the magneto-static code. In Tab. 7.4 we give the effect of a given azimuthal pre-stress on the multipoles for the collared coil at ambient temperature, keeping constant the pole shim thickness. One can see that the effect of deformations is non-negligible mainly for the b_3 and the b_5. From the b_9 onwards the effect is less than 0.1 units. Explicit dependence can be worked out through a linear fit:

$$\Delta b_3 = -0.0457 \, \sigma_w \tag{7.1}$$

$$\Delta b_5 = +0.0114 \, \sigma_w \tag{7.2}$$

$$\Delta b_7 = -0.0018 \, \sigma_w \tag{7.3}$$

7.2.3 Experimental data

To compare the experimental data of the prototypes and of the pre-series dipole we subtract from the measurements the multipole variation due to pole shims different from the nominal ones (see Tab. D.1 and Tab. D.3) according to our sensitivity estimate. At the moment no data concerning the pre-stress on the prototypes and on the pre-series magnets are available: we therefore assume rather arbitrarily a nominal pre-stress. In Fig. 7.4 we plot the measurements of the b_3 and of the b_5: dipoles are built by three different firms whose tooling does not show a specific effect on field quality.

The solid lines in Fig. 7.4 represent the averages over the pre-series and over the prototypes, that are also given in Tab. 7.5 (row "Prototypes" and "Pre-series").

Table 7.4: Effect of a collar deformation due to an azimuthal pre-stress σ_w (MPa) at ambient temperature on odd multipoles (10^{-4} units, $R_{ref} = 17\,\text{mm}$) for the collared coil.

σ_w	Δb_3	Δb_5	Δb_7
0	−0.00	+0.00	−0.00
10	−0.46	+0.11	−0.02
20	−0.91	+0.23	−0.04
30	−1.37	+0.34	−0.05
40	−1.83	+0.45	−0.07
50	−2.29	+0.57	−0.09
60	−2.74	+0.68	−0.11
70	−3.20	+0.80	−0.12
80	−3.66	+0.91	−0.14
90	−4.11	+1.02	−0.16

A statistical error of $2\times$ the standard deviation of the average σ_{av} has been associated to these values, being

$$\sigma_{av} = \frac{\sigma}{\sqrt{N}}. \tag{7.4}$$

and N the number of measured dipoles. Some difference is observed between prototypes and pre-series dipoles: this is due to a change of the inner collar profile, introduced in the design of the pre-series to compensate the ovalisation of the collars. In the next Section we evaluate with the finite element model the impact of this modification on the field quality, comparing simulations with the experimental data.

Table 7.5: Measured average with $2 \times \sigma_{av}$ of uncertainty at 293 K and design odd multipoles, in units 10^{-4} of the main field at $R_{ref} = 17\,\text{mm}$.

	b_3	b_5	b_7
5 Prototypes	+1.49 ± 1.11	+0.49 ± 0.39	+0.81 ± 0.06
15 Pre-series	−0.25 ± 0.97	+1.17 ± 0.23	+0.66 ± 0.05
Nominal coil	+3.91	−1.04	+0.75
Steel collars	−1.36	+0.37	−0.09
Design	+2.55	−0.67	+0.66

In Tab. 7.5 the measured multipoles are compared with the design values of the collared coil (given in row "Design"), i.e., with the multipoles expected for a coil in
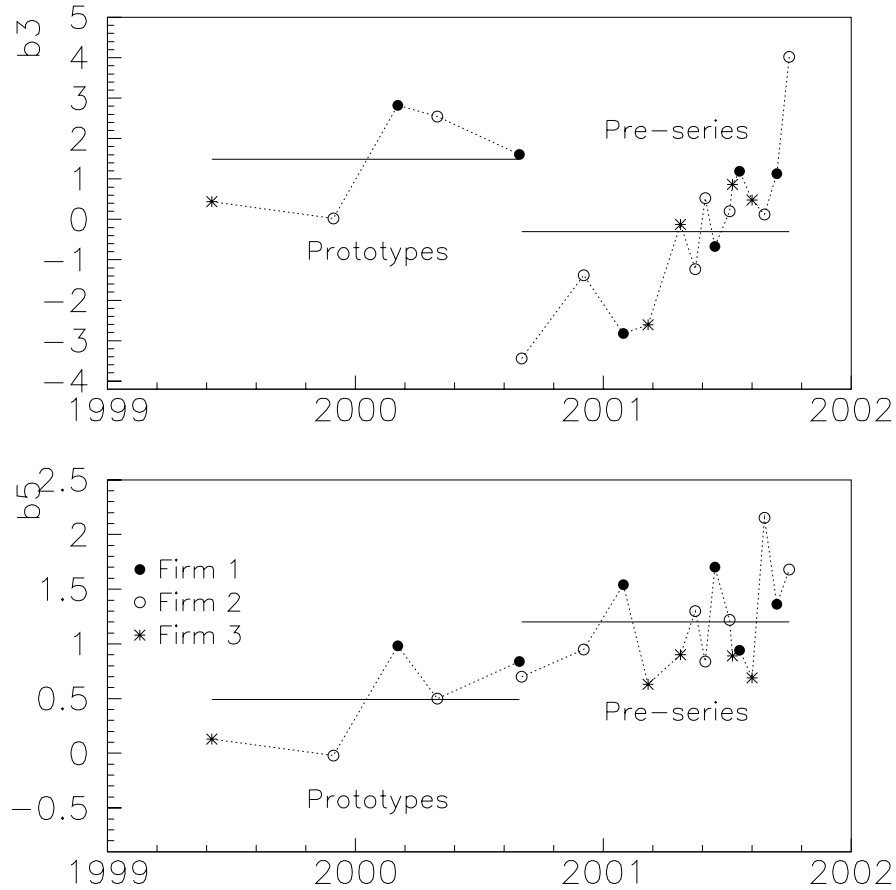
Figure 7.4: Sextupole and decapole measured in collared coils of the prototypes and the pre-series dipoles (markers) and averages (solid lines) versus the test date, in units 10^{-4} of the main field at 17 mm.

a circular cavity, under an azimuthal compression of 75 MPa. Both the prototypes and the pre-series dipoles feature a discrepancy with respect to the expected values: this is particularly important for the b_5. In Sect. 7.2.5 we trace back the origin of these discrepancies between the design and measured harmonics.

This design values is given by two contributions: the nominal coil cross-section contribution (row "Nominal coil" in Tab. 7.5) and the austenitic steel collar contribution (row "Steel collars" in Tab. 7.5)

Nominal coil cross-section contribution

The nominal coil cross-section presented in Fig. 2.6 has been chosen to generate a non-zero value of the low order odd multipoles which partially compensates the effect of the persistent currents [66]. These currents are induced inside the superconducting

cables by field variations occurring during the ramp-up of the magnet. They give rise to a strand magnetisation that considerably affects the field pattern. In the LHC dipole, the effect of the persistent currents is of about -8.0 units for the b_3, about $+1.0$ units for the b_5 and about -0.4 units for the b_7 at the injection and it almost disappears at nominal field.

The coil cross-section has been designed in order to reduce the field harmonics due to the persistent currents at low field and to avoid too high harmonics at nominal conditions.

Austenitic steel collar contribution

The stainless steel used for the collars is paramagnetic, with a relative magnetic permeability μ_r slightly larger than 1. For the steel of the main dipole series production (made by Nippon Steel, Japan), one has $\mu_r = 1.0021$. Although the steel magnetisation is quite small and does not affect the main dipolar component of the field, it must be accounted because it has an impact on the field-shape harmonics. The effect of the austenitic steel collars has been computed with ROXIE [67].

The steel magnetisation influences the low order allowed harmonics only, namely on the b_3, the b_5 and the b_7: in these cases, variations of -1.36, $+0.37$ and -0.09 units are induced, respectively.

7.2.4   Differences between pre-series and prototype field harmonics

To avoid detrimental consequences induced by the deformation of the collar shape under pre-stress, the collar cavity in the pre-series dipole magnet has been modified.

The effect of the pre-stress on the collar cavity can be described in a first approximation by a vertical deflection (*ovalisation*), which increases the vertical diameter of the collars keeping unchanged the horizontal one. This deflection has been corrected by shifting downward of 0.1 mm the centre of the collar cavity (see Fig 7.5): the idea was to design a collar cavity that becomes circular under the effect of the coil pre-stress.

Table 7.6: Differences between pre-series and prototypes magnets: measurements with $2 \times \sigma_{av}$ of uncertainty and model results, in units 10^{-4} of the main field at $R_{ref} = 17$ mm.

	Δb_3	Δb_5	Δb_7
Measur.	-1.74 ± 2.08	$+0.68 \pm 0.62$	-0.15 ± 0.11
Model	-1.47	$+0.00$	-0.03

Center of the collar
cavity →
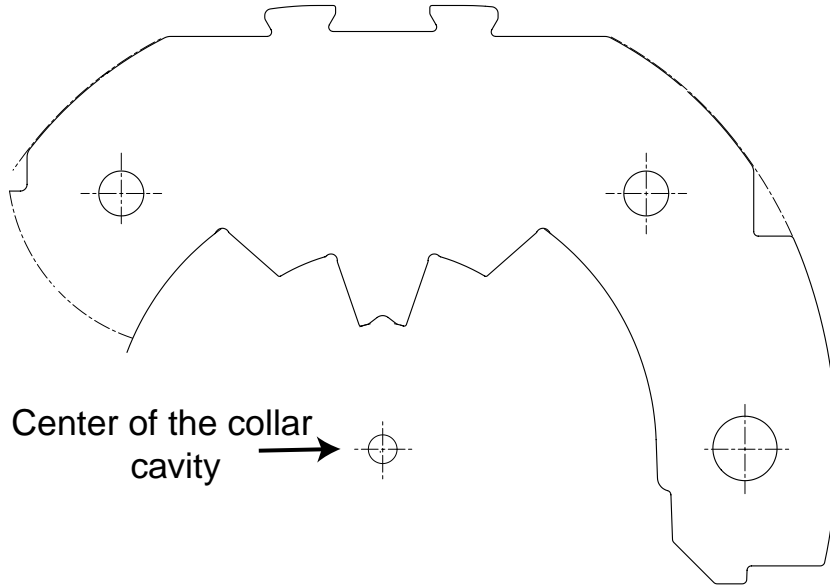
Figure 7.5: The collar cavity.

We used the finite element model, reproducing the new collar profile in our code, to compute the modification of the magnetic field with respect to the previous configuration. In Tab. 7.6 we compare the results of simulation with the differences of the average multipoles measured in the pre-series and in the prototypes. The results of the numerical computation are consistent with the experimental data.

7.2.5 Differences between pre-series and design field harmonics

The design values of the collared coil presented in Tab. 7.5 take into account the geometry of the current distribution in the design coil and the non-negligible contribution of the permeability of the stainless steel collars (see Sect. 7.2.3 for a definition of design values). These expected harmonics are considerably different from the measured ones in the pre-series dipoles. In Tab. 7.5 (row "Measur.") we give the differences between the pre-series measured harmonics and the design values. An offset of -2.80 units and $+1.84$ units respectively for the b_3 and the b_5 is observed.

To trace back the origin of these discrepancies, we remind that the design values neglect the effect of the azimuthal pre-stress on the shape of collar cavity, which gives rise to important conductor displacements (a few tenths of mm). We evaluate this contribution with the finite element model: we add the computed effect of the collar shape modification of the pre-series magnet (see Tab. 7.6) to the computed effect of the pre-stress (see Tab. 7.4). The results of the numerical computations are given in

Tab. 7.5 (row "Model"). One observes an important reduction of the sextupole and a strong increase of the decapole. These trends are clearly confirmed by experimental data. Even though the estimates do not agree with the measured values within the associated error, these data show that deformations modelled through finite element methods account for a large part of the discrepancy between nominal and measured values.

Table 7.7: Differences between pre-series and design: measurements with $2 \times \sigma_{av}$ of uncertainty and model results, in units 10^{-4} of the main field at $R_{ref} = 17$ mm.

	Δb_3	Δb_5	Δb_7
Measur.	-2.80 ± 0.97	$+1.84 \pm 0.23$	$+0.00 \pm 0.05$
Model	-4.90	$+0.85$	-0.16

The offset between nominal and measured multipoles can be compared to the constraints on systematics multipoles given by beam dynamics. Recent work [68] shows that the allowed range for the systematic b_3 and b_5 is 6 units and 0.6 units respectively. Therefore, the discrepancy with respect to the nominal design is half window width for the b_3, and three times the window width for the b_5: this shows that in the LHC main dipole these effects cannot be neglected [69].

7.3 Corrective strategy: variation of the pole shim thickness

Among the possible corrective strategies that can be implemented during magnet production to fine tune the magnetic field, the pole shim thickness modification represent an easy and effective way. As already explained in Sect. 2.2.4, a variation in the pole shim dimension allows to change the total azimuthal coil length, thus modifying the multipolar contents of the superconducting coil.

Indeed, it must be pointed out again that any variation of the pole shim size also determines a modification of the coil and collar loads and deformations. In a first approximation, an increase in the pole shim size can be modelled as a uniform azimuthal compression of the coil. Indeed, the change in the load patterns implies that the impact of a larger pole shim on coil geometry can be more complicated. In this Section we compare results of a dedicated experiment with numerical simulations.

7.3.1 Experimental measurements

During the experiment described in Sect. 5.3.1 the magnetic field of the five collared coils has also been measured at ambient temperature. It must be pointed out that,
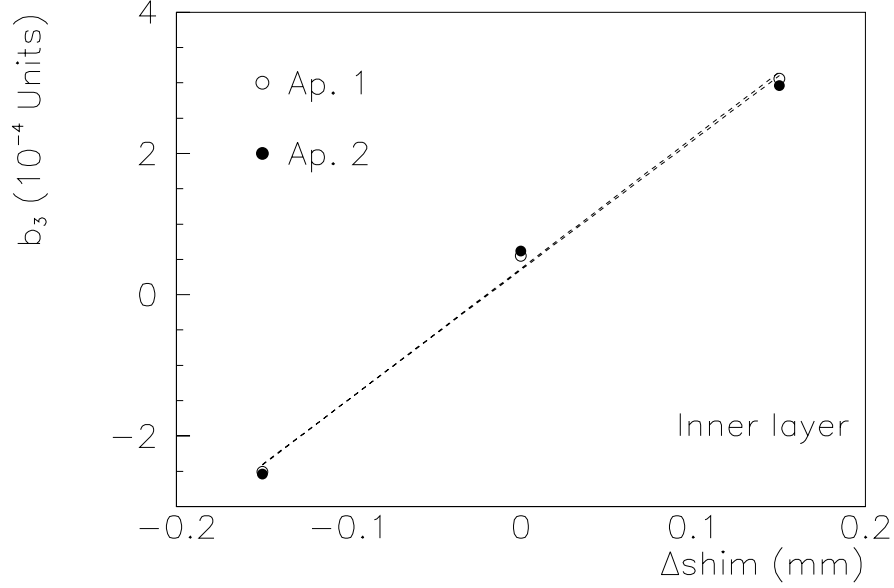
Figure 7.6: b_3 (10^{-4} units) versus pole shim thickness variation (mm) for the inner layer and for the two apertures (Ap. 1 and Ap. 2), experimental data and linear fit.

since the top-bottom and left-right symmetries of the azimuthal coil length have been kept, only the sensitivity of the shim thickness on the odd multipoles has been studied.

The magnetic measurements of the b_3 and the b_5 in the collared coil versus the pole shim thickness are shown in Fig. 7.6, Fig. 7.7, Fig. 7.8 and Fig. 7.9. Also in this case, as for the pre-stress, one finds a good linearity and a similar slope for both apertures. Best fits with a straight line provide the sensitivities.

In Tab. 7.8 we give (row "Measur.") the sensitivity on the pole shim thickness measured for the b_3, the b_5 and the b_7 (the higher order multipoles are almost unaffected by the pole shim size) with an error of $2 \times$ the standard deviation σ: we point out that the values of the sextupole strongly depend on the azimuthal coil length. An additional pole shim of 0.1 mm respectively in the inner and in the outer layer determines an increase of b_3 of 1.85 units and 1.36 units. On the other hand, the b_5 and the b_7 are mostly affected by the inner layer pole shim, as expected.

Since the maximum admissible variation of pole shim thickness is ± 0.12 mm, due to the ± 15 MPa limitation in the azimuthal pre-stress, the maximum range of tunability provided by pole shim thickness is ± 3.3 units for the b_3, whilst one has ± 0.35 units and ± 0.15 units for the b_5 and b_7 respectively.
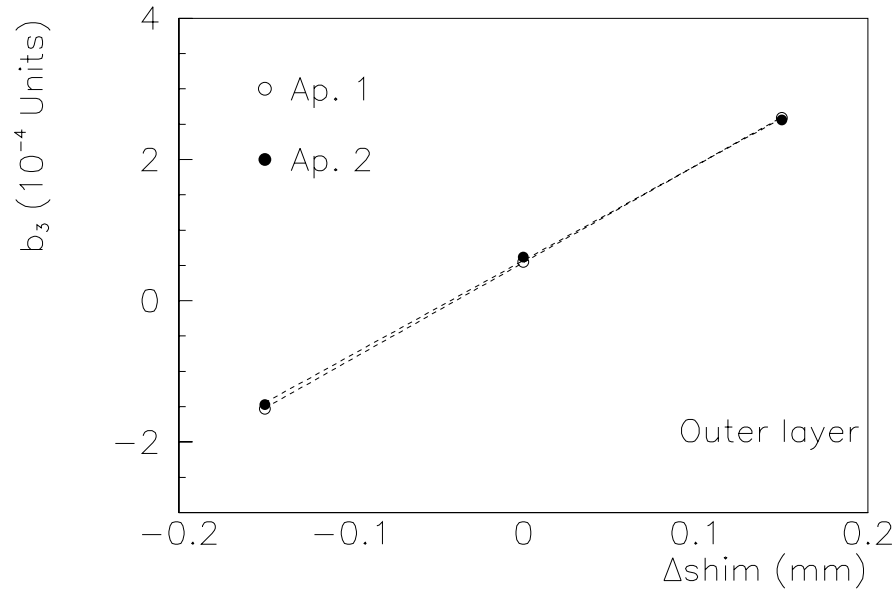
Figure 7.7: b_3 (10^{-4} units) versus pole shim thickness variation (mm) for the outer layer and for the two apertures (Ap. 1 and Ap. 2), experimental data and linear fit.
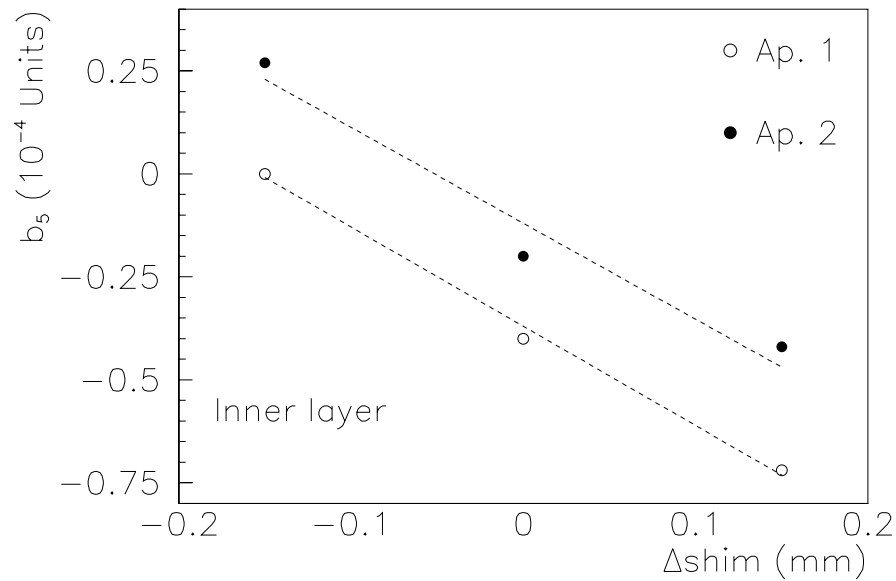
Figure 7.8: b_5 (10^{-4} units) versus pole shim thickness variation (mm) for the inner layer and for the two apertures (Ap. 1 and Ap. 2), experimental data and linear fit.
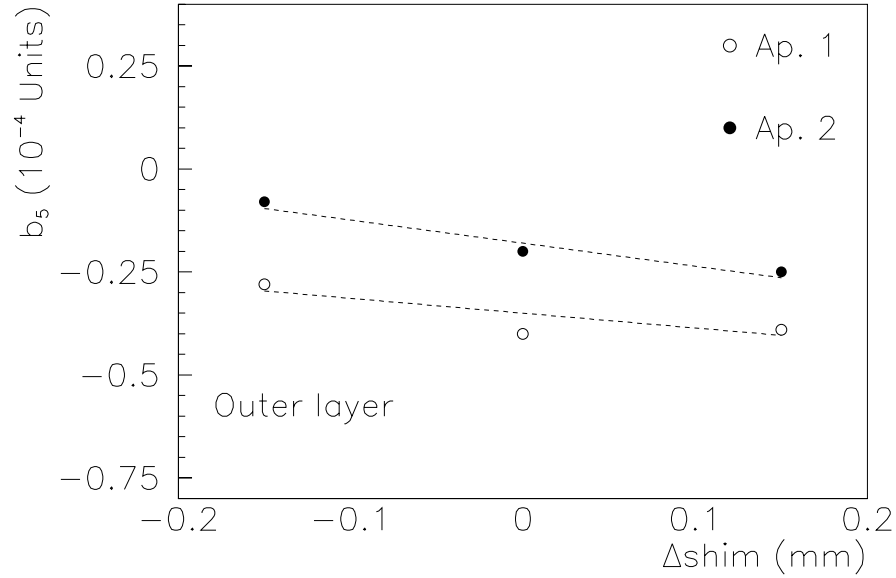
Figure 7.9: b_5 (10^{-4} units) versus pole shim thickness variation (mm) for the outer layer and for the two apertures (Ap. 1 and Ap. 2), experimental data and linear fit.

7.3.2   Results: model vs measurements

The dependence of field quality on pole shim thickness can be modelled by a uniform compression of the conductors along the azimuthal direction. With this approximation, a difference in the pole shim thickness provokes an equal reduction of the azimuthal coil length. This is based on the assumption that both the copper wedges and the collar cavity are infinitely rigid. Results of this model overestimate the sensitivity experimentally measured (see Tab. 7.8, row "Uniform compression"): in particular the decapole differs by 60 % with respect to the experimental data.

To better model the effect of the pole shim size one has to take into account that the collars are not infinitely rigid. This means that an increase of the pole shim thickness is partially compensated by the collar vertical deformation. In Ref. [20] it has been proposed that the coil azimuthal length should be varied by the additional pole shim thickness minus the induced vertical deformation of the collars: geometric measurements (see Sect. 5.3.2) show that a 0.1 mm thicker pole shim on one layer increases the collar vertical radius of 0.01 mm. Therefore one should obtain a 10 % lower sensitivity (see Tab. 7.8, row "Compens. compression"). This second approximation shows agreement with experimental data for the b_3 and the b_7, but one still has a large discrepancy in the b_5. We perform thereafter a mechanical computation with the finite element model to evaluate the complete map of deformations determined by a change of the pole shim size. The finite element model provides the deformations induced by the variation in the pole shim thickness.
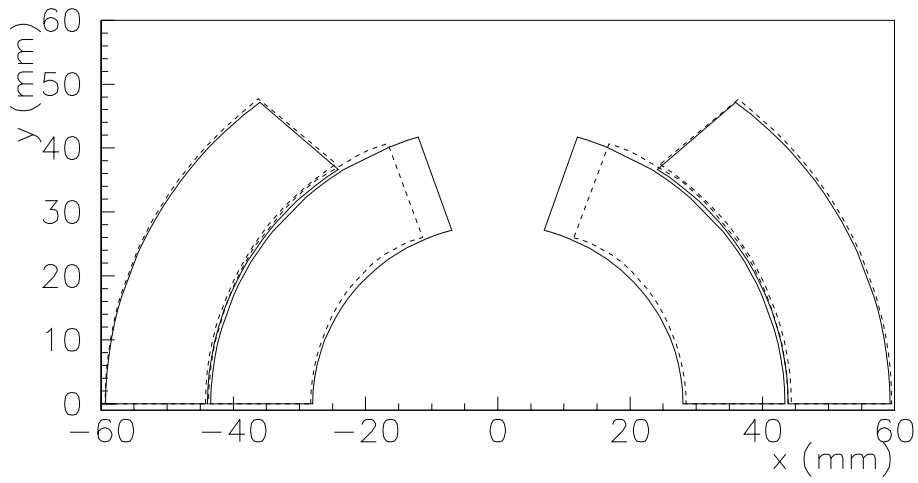
Figure 7.10: Nominal coil geometry (solid line) and deformed geometry (dashed line) induced by a 0.1 mm thicker shim in the inner coil. Deformations are magnified by a factor 50.
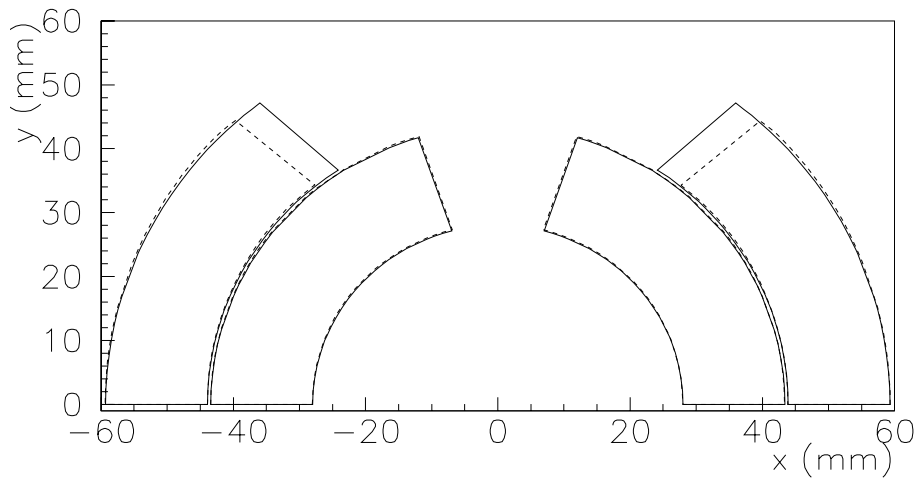
Figure 7.11: Nominal coil geometry (solid line) and deformed geometry (dashed line) induced by a 0.1 mm thicker pole shim in the outer coil. Deformations are magnified by a factor 50.

Table 7.8: Effect on an additional pole shim of 0.1 mm: measurements with an error of $2 \times \sigma$ and model results, in units 10^{-4} of the main field at 17 mm.

Δb_3	Inner layer	Outer layer
Uniform compression	+2.18	+1.62
Compens. compression	+1.96	+1.46
Finite element model	+1.88	+1.46
Measur.	$+1.85 \pm 0.26$	$+1.36 \pm 0.10$
Δb_5	Inner layer	Outer layer
Uniform compression	−0.40	−0.08
Compens. compression	−0.36	−0.07
Finite element model	−0.29	−0.05
Measur.	-0.24 ± 0.06	-0.05 ± 0.04
Δb_7	Inner layer	Outer layer
Uniform compression	+0.15	−0.02
Compens. compression	+0.14	−0.02
Finite element model	+0.12	−0.02
Measur.	$+0.13 \pm 0.04$	-0.01 ± 0.00

In Fig. 7.10 and Fig. 7.11 we plot the nominal geometry of the coils (solid lines), and the displacements induced by a pole shim variation of 0.1 mm on the inner and on the outer layer respectively (dashed lines). Displacements are magnified by a factor 50 to make the figure easier to read and to interpret.

The first graph shows that the variation on the inner layer pole shim provokes a inner coil azimuthal compression, but also radial deformations. The azimuthal displacement of the inner coil is around 0.095 mm, i.e., 5 % less than the additional pole shim thickness. The inner coil is also radially shifted in the outward direction up to 0.017 mm; the maximum amplitude of this radial movement is reached in correspondence of the pole of the outer layer (around 55 degrees). A reduction of this amplitude is then observed on the last block of the inner layer (at around 75 degrees), close to the pole. Therefore, this shows that coil deformations cannot be described by a simple elliptic mode, i.e. a deformation whose radial amplitude linearly increases with the angle, reaching a maximum at 90 degrees. This importance of high order modes in radial displacements has been already observed in the analysis of coil deformations for the main LHC dipoles [70].

The outer coil has a very small increase of the azimuthal length (0.003 mm) due to the weak cross-talk between the two layers. It also features a radial displacement of around 0.010 mm. A similar situation holds for the left part of the coil (i.e., towards the centre of the magnet), the only difference being a smaller radial displacement in the coil mid-plane, due to the two-in-one collar geometry.
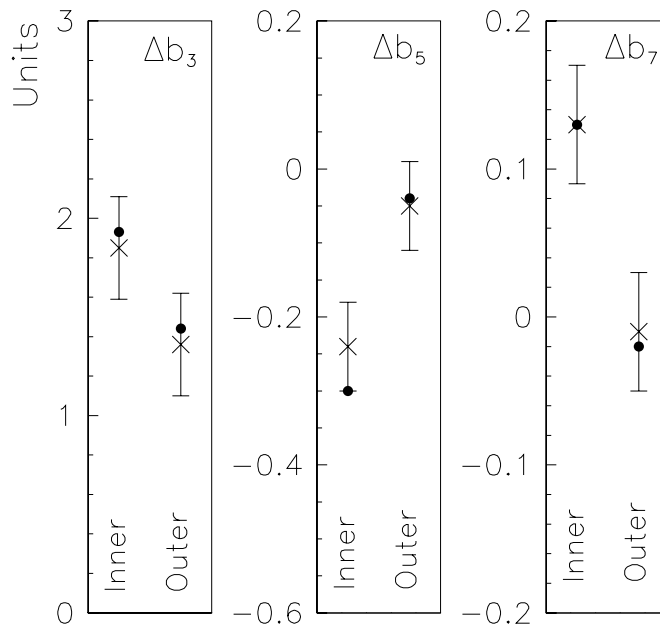
Figure 7.12: Effect on an additional pole shim of 0.1 mm: measurements (cross markers) with an error of $2 \times \sigma$ and finite element model results (dot markers), in units 10^{-4} of the main field at 17 mm.

A 0.1 mm thicker outer pole shim provokes an azimuthal displacement of the outer coil pole of around 0.090 mm (see Fig. 7.11). Radial displacements of the outer coil are around 0.005 mm on the pole, whilst practically no displacements are observed in the inner coil (less than 0.003 mm).

In conclusion, the deformation of the coil cannot be described by a simple elliptic mode, but also by higher order modes in the radial displacements. When the complete map of deformations is transferred to the magneto-static code, one gets a sensitivity of -0.30 units for the b_5 (see Tab. 7.8, row "Finite element model"). Thereafter the results of the finite element model are within the $2 \times \sigma$ error bar of the experimental measurements for all the low order odd multipoles (see Fig. 7.12) .

7.4   Magnetic measurements of the cold mass

In Sect.5.4 we studied the effect of the yoking from a mechanical point of view, focusing on the variation of the coil pre-stress between the collared coil and the assembled cold mass at ambient temperature. We consider now the magnetic effect of the yoke by analysing the measurements performed at 293 K on the assembled cold mass of 6 dipoles of the pre-series production. Also in this case measurements

are carried out in both the apertures at $293\,$K with a low current ($12\,$A). In Tab. E.1 and we give the averages along the straight part.

7.4.1 Correlation between field harmonics and shim thickness

The cold mass features somewhat different sensitivities of the field on the pole shim size. This is due to the magnetic influence of the iron yoke. In Tab. 7.9 we estimate this effect using the magneto-static model. If we compare to the sensitivity values obtained for the collared coil (see Tab. 7.3) we observe that the cold mass has a 20 % lower sensitivity: this is due to a scale-down of the multipoles since the main field is enhanced by the iron yoke of about 20 %.

Table 7.9: Effect of a reduction of $0.1\,$mm of the azimuthal coil length on odd multiples ($10^{-4}\,$units, $R_{ref} = 17\,$mm) computed with the magneto-static model for the assembled cold mass at $293\,$K.

	Inner layer	Outer layer
Δb_3	+1.82	+1.35
Δb_5	−0.33	−0.07
Δb_7	+0.13	−0.02

7.4.2 Differences between cold mass and collared coil field harmonics

The magnetic functions of the iron yoke is to enhance the dipole field in the two apertures and to confine the field flux inside the cold mass. In the LHC dipole the increase of the field due to the iron yoke is of about the 20 %.

At high field, the yoke starts saturating in a non-uniform way: this has an influence on the low order allowed harmonics (namely b_3 and b_5); the yoke shape is thereafter designed in order to keep the saturation effects as small as possible [71].

We want now to study the magnetic effect of the yoke at low field and at ambient temperature. Since all the multipole coefficients are normalised to the main field, when iron is placed around the magnet they will be decreased by a factor 1.20. Moreover, the yoke contributes to an additional offset to the multipoles. The relation between cold mass and collared coil coefficients is therefore:

$$b_n^y = b_n^c/1.20 + b_n^{off} \qquad (7.5)$$

where b_n^y and b_n^c are respectively the coefficients in the cold mass and in the collared coil, while b_n^{off} is the additional offset produced by the yoke.
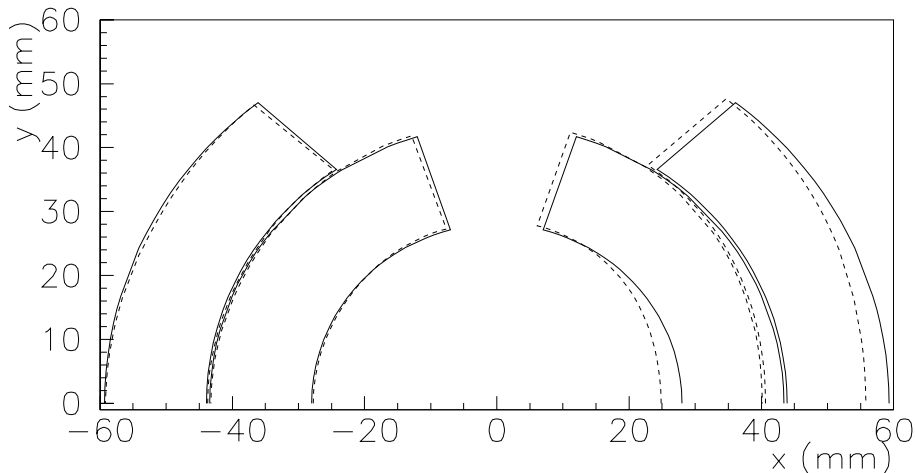
Figure 7.13: Nominal coil geometry (solid line) and deformed geometry (dashed line) induced by the yoking. Deformations are magnified by a factor 50.

In Tab. 7.10 we give the b_n^{off} measured between the the cold mass at ambient temperature (see Tab. E.1) and the collared coil (see Tab. D.3): the contribution of the yoke is of $+4.57$ units for the b_3, while the b_5 and the the b_7 remain almost unchanged. This contribution can be explained by two effects: the effects of the yoke magnetisation on the field-shape and the effect of the additional coil deformation induce by the yoking.

Table 7.10: Differences between cold mass at 293 K and collared coil at 293 K: measurements with $2 \times \sigma$ of uncertainty and model results, in units 10^{-4} of the main field at $R_{ref} = 17$ mm.

	Δb_3	Δb_5	Δb_7
Measur.	$+4.57 \pm 0.56$	$+0.05 \pm 0.05$	-0.01 ± 0.05
Yoke magn.	$+3.23$	$+0.00$	$+0.03$
Deform. model	$+1.46$	$+0.01$	$+0.00$
Total model	$+4.69$	$+0.01$	$+0.03$

The effects of the yoke magnetisation has been calculated with the magnetic code ROXIE [67] and is given in Tab. 7.9, row "Yoke magn.": the results of the magnetic model confirm the measurement data, giving more than 3 units for the b_3 and no effect on the b_5 and on the b_7.

The magnetic code does not consider the change of the deformation of the coil from the situation after collaring to the assembled cold mass. In Sect.5.4 we observed

with the finite element model that the yoke induces on the coil pre-stress an increase of about 4 MPa, in agreement with the measured variation of about 6 ± 3 MPa. We want now to evaluate with the mechanical model if this change of stress determines a significant modification of the coil shape and consequently of the coil multipolar content.

We compute the field generated by the coil after the yoking and after the collaring: the difference between the harmonics gives the contribution on the field quality of the coil mechanical deformation induced by the yoke. In Tab. 7.10 (row "Deform. model") we notice that this effect, represented graphically in Fig. 7.13, contributes to approach for the b_3 the results of the magnetic model (row "Yoke model") to the experimental data.

Nevertheless, we must point out that the mechanical effect of the yoke at ambient temperature is almost negligible, both from the point of view of the coil pre-stress, with an increase lower than the 10 % with respect to the collared coil, and from the point of view of the coil shape modification. In fact, in Sect. 7.2.5 we presented the the discrepancies observed between the design harmonics and the collared coil harmonics. These discrepancies were partially explained by the deformations of the collar cavity due to the coil pre-stress. Now, the assembly of the yoke does not compensate the field errors observed in the collared coil.

We conclude the the effect of the coil deformations on the field quality must be taken into account already in the phase of the coil cross-section design.

Chapter 8

Magnetic behaviour of the dipole at $1.9\,\mathrm{K}$

In Chapt.6 we analysed how the coil pre-stress changes during the cool-down from ambient temperature to $1.9\,\mathrm{K}$. In this Chapter we consider the magnetic effect of the cool-down by comparing the magnetic measurements performed at $293\,\mathrm{K}$ and at $1.9\,\mathrm{K}$.

8.1 Magnetic measurements of the cold mass

We analyse the measurements performed at $1.9\,\mathrm{K}$ on the assembled cold mass of 5 pre-series dipoles. The measurements are carried out in both the apertures at $1.9\,\mathrm{K}$ with a current of $5000\,\mathrm{A}$. At this current, the field quality is dominated by the coil geometry: the persistent current effect is already negligible, while the deformations of the coil induced by the electro-magnetic forces are not yet too significant. In Tab. F.1 we give the multipole averages along the dipole straight part.

8.1.1 Correlation between field harmonics and shim thickness

In Tab. 8.1 we give the correlation between field harmonics and shim thickness estimated by the magneto-static model at $1.9\,\mathrm{K}$ and with a current of $5000\,\mathrm{A}$: the sensitivity values are the same as the ones computed for the assembled cold mass at $293\,\mathrm{K}$.

8.1.2 Difference between magnetic field at ambient temperature and at $1.9\,\mathrm{K}$

If we compute the differences between the harmonics measured on the cold mass at $1.9\,\mathrm{K}$ (see Tab. F.1) and the harmonics measured on the cold mass at $293\,\mathrm{K}$ (see

Table 8.1: Effect of a reduction of 0.1 mm of the azimuthal coil length on odd multiples (10^{-4} units, $R_{ref} = 17$ mm) computed with the magnetic model for the assembled cold mass at 1.9 K.

	Inner layer	Outer layer
Δb_3	+1.82	+1.35
Δb_5	−0.33	−0.07
Δb_7	+0.13	−0.02

Tab. E.1) we notice that the contribution of the cool-down is of −0.24 units for the b_3 and −0.22 units for the b_5, while the b_7 remains almost unchanged (see Tab. 8.2, row "Measur."). Despite a great change of pre-stress from ambient to 1.9 K, during cool-down a negligible effect is observed on the low order odd harmonics.

We study this particular behaviour with the finite element model: in Fig. 8.1 and Fig. 8.2 we plot the variation of the sextupole and the decapole with respect to the coil pre-stress. The computation has been performed considering the case of the collared coil at ambient temperature and of the cold mass at 1.9 K. As already explained in Sect. 7.2.2, a variation of the pre-stress induces a modification of the shape of the collar cavity, thus yielding a change in the magnetic field. This change of the field quality with respect to the pre-stress is almost linear.

If we perform the same analysis at 1.9 K we obtain a very similar dependence of the sextupole and the decapole on the pre-stress, but an offset occurs between the two situations. If one takes into account the change of pre-stress from 75 MPa at ambient temperature to 35 MPa at 1.9 K, the offset of the b_3 and of the b_5 is partially compensated.

Table 8.2: Differences between cold mass at 1.9 K and cold mass at 293 K: measurements with $2 \times \sigma$ of uncertainty and model results, in units 10^{-4} of the main field at $R_{ref} = 17$ mm.

	Δb_3	Δb_5	Δb_7
Measur.	−0.24 ± 1.17	−0.22 ± 0.32	+0.03 ± 0.07
Cold mass - coll. model	+0.64	+0.04	−0.01
Yoking model	+0.86	+0.13	−0.12
Total model	−0.22	−0.09	+0.11

We can explain this compensation reminding that the coil and the collars feature a significant difference in the thermal contraction coefficient, that determines both a reduction of the pre-stress and a change in the coil shape (see Fig. 8.3).
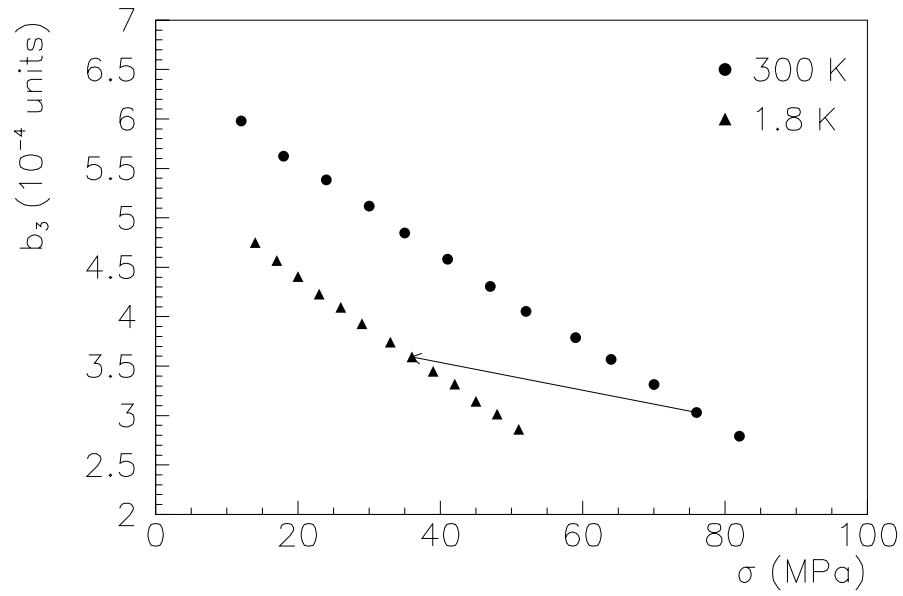
Figure 8.1: b_3 (10^{-4} units) versus pre-stress (MPa) at $293\,\mathrm{K}$ and at $1.9\,\mathrm{K}$: results of the finite element model.
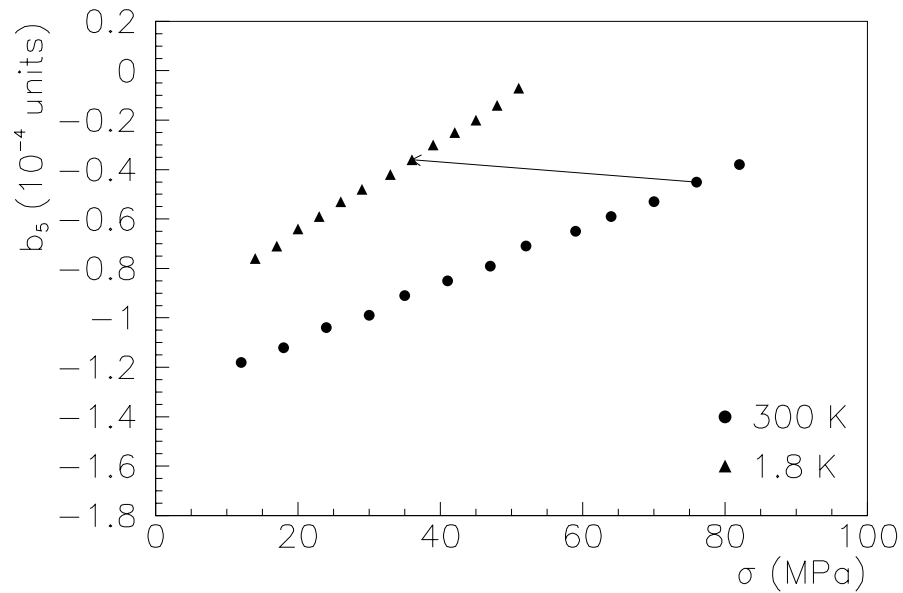
Figure 8.2: b_5 (10^{-4} units) versus pre-stress (MPa) at $293\,\mathrm{K}$ and at $1.9\,\mathrm{K}$: results of the finite element model.
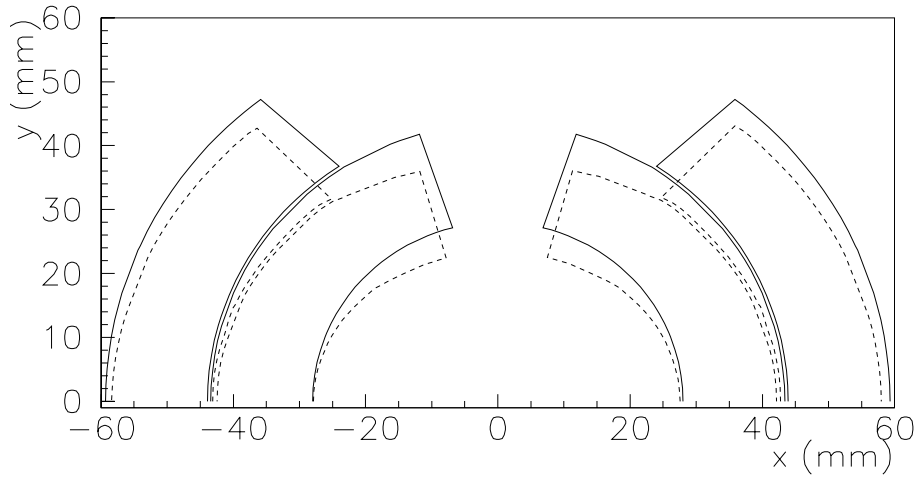
Figure 8.3: Nominal coil geometry (solid line) and deformed geometry (dashed line) induced by the cool-down from collared coil at 293 K to cold mass at 1.9 K. Deformations are magnified by a factor 50.

In Tab. 8.2 we give the computed effect of the cool-down between the cold mass at 1.9 K and the collared coil at ambient temperature (row "Cold mass - coll. model"). If we subtract from this effect the difference between the collared coil and the cold mass at ambient temperature (row "Yoking model") evaluated in Sect. 7.2.5, we obtain a very good agreement between the experimental data and the results of the numerical computation (row "Total mode").

Chapter 9

Conclusions

The mechanical and magnetic behaviour of the main superconducting dipole for the Large Hadron Collider has been modelled and analysed. The dipole was studied during the phase of the assembly and the cool-down from ambient temperature to $1.9\,\text{K}$.

We performed measurements of the thermo-mechanical properties of dipole coil. We measured the stress-displacement curves at $293\,\text{K}$ and at $77\,\text{K}$ of two stacks of conductors [34]. The curves are non-linear and feature a strong hysteresis between the loading and the unloading phase of the compression cycle. The shape of the unloading is shown to depend on the peak stress attained during the cycle. The elastic moduli were evaluated as the derivatives of stress-displacement curves. At $293\,\text{K}$ the elastic modulus in the loading phase is around $6.5\,\text{GPa}$ for stresses above $70\,\text{MPa}$ and goes to zero for decreasing loads. At $77\,\text{K}$ a $50\,\%$ increase of the elastic modulus is observed in the loading phase. In the unloading phases, elastic moduli are the same at $293\,\text{K}$ and at $77\,\text{K}$; they feature a roughly linear dependence on the stress.

We pointed out severe difficulties in defining strains for the stacks, due to the lack of precision of coil size in the unloaded state. This has no effect on the evaluation of the elastic modulus, but strongly affects the measurement of the thermal contraction coefficient [35]. We evaluated the thermal contraction coefficient measuring stress losses from five different stresses at $293\,\text{K}$ and different cool-down configurations, obtaining results that range from 0.004 to 0.012. Different assumptions on the trajectory in the stress-strain plane followed during cool-down lead to additional variations of around 0.001. We showed that different cut-stresses and linear or non-linear approximation for the stress-strain relation also lead to significant variations in the thermal contraction coefficient derived from stress losses. We conclude that the thermal contraction coefficient strongly depends on the scheme used to derive it from measurements [33]. This explains the rather wide range of results that can be found in the literature.

We implemented the thermo-mechanical properties of the coil in a finite element model of the dipole cross-section. The model were validated by means of an exper-

imental apparatus based on the speckle interferometry. In particular the modeling of the coil non-linear behaviour and of the interfaces between the magnet components were successfully compared to experimental measurements [45, 46]. We found a good quantitative agreement between the displacements measured with our experimental apparatus and the finite element results. The contact elements used to model the interfaces between the coil and the collars provided correct estimates of the gliding between the two materials. The patterns of displacements of the FEM and of the experimental measurements well agreed in the analysed cases. Moreover, we observed an increased rigidity of the coil for higher loads, that agreed with the experimental curve used to model the coil into the finite element code.

The finite element model was then used to study the stresses and the deformations of the dipole components at ambient temperature. A new approach was implemented with respect to previous models: we included the collaring procedure in the numerical code through the definition of equivalent elastic moduli [72]. The model has been used to analyse the effect on the coil pre-stress of the pole shim dimension. This effect has been measured in a dedicated experiment where a dipole magnet has been re-assembled five times with different pole shims [57]. The FEM with the equivalent elastic moduli provided values of the sensitivity of the coil pre-stress on the shim thickness consistent with the experimental data. A great improvement has been therefore obtained in the modeling of the effect of the shims; in fact, the model with the standard approach gave a discrepancy with the measurements of about a factor two.

A study of the mechanical deformations of the collars has been carried out. The aim was to evaluate how their deflection affects the coil shape. In particular, the vertical deformation of the collars at the end of the collaring procedure was analysed. Measurements of the collar deflection shown that a coil pre-stress increase of 10 MPa provokes an increase of the collar vertical diameter of 0.036 mm. These values were recovered by the finite element model and by a simplified analytical model, proving that our modeling of the collar behaviour is correct. To conclude the mechanical analysis at ambient temperature, the effect of the yoke on the coil pre-stress was studied. An increase of the coil pre-stress after the yoking of 6 MPa was measured, in agreement with the results of the numerical computations.

For the modeling of the coil pre-stress losses measured during the cool-down, we proposed an equivalent elastic modulus at 1.9 K and an equivalent thermal contraction coefficient based on the measured stress-dependence of the coil thermal shrinkage. With these new models, we explained the large coil pre-stress loss during cool-down [72]. This loss was already observed in the superconducting magnet for the SSC in 1992, but it could not be recovered by a model with the standard approach.

The magnetic analysis was based on the implementation of the results of the mechanical analysis performed by the finite element model in the magneto-static model of the dipole coil. The aim was the evaluation of the effect of the coil de-

formations on the field quality. We explored the impact of the modification of the collar shape on the magnetic field as a possible corrective action of the field errors. Then, we explained how the variations of the magnetic field along the dipole axis are correlated to the fabrication tolerances of the components [19, 61].

The magnetic measurements performed at ambient temperature were analysed. The differences between prototypes and pre-series magnet were justified by the collar anti-ovalisation implemented in the pre-series production. Moreover, a large part of the discrepancies of the measured field harmonics with respect to the expected design values were explained by evaluating the effect of the coil deformations [73].

We analysed the variation of the pole shim size as a corrective action for the odd multipoles. We presented the measurements of the dependence of the field quality on the shim thickness performed on a dipole. Then we compared the experimental data with the results of the finite element model where the equivalent material properties was implemented. With respect to the previous modeling, the FEM provided values consistent with the measurements for all the low-order odd harmonics [57].

Finally, the magnetic measurements performed at 1.9 K were analysed. By means of the FEM we pointed out the modification of the coil shape during cool-down. This shape variation is due to the different thermal contractions of the coil and of the collars. The change of the coil geometry was then transfered to the magneto-static model. A good agreement was found between the computed and the measured effect of the cool-down on field harmonics.

Appendix A

Calibration of the experimental apparatus

The measurements of the elastic modulus at $293\,\mathrm{K}$ and $77\,\mathrm{K}$ performed by the electro-mechanical apparatus have been checked with four $100\,\mathrm{mm}$ height metallic samples (aluminium 6082 T6, copper, invar and steel 316 LN). No measurable hysteresis has been observed. In Table A.1 we give the results of the measurements with an error of two sigmas. A good agreement with the reference values is found.

Table A.1: Measurements of the sample elastic modulus (GPa) at $293\,\mathrm{K}$, at $77\,\mathrm{K}$ and of the integral thermal contraction coefficient α (10^{-3}) from $293\,\mathrm{K}$ to $77\,\mathrm{K}$ evaluated by the stress losses: comparison with reference values.

	E ($293\,\mathrm{K}$)		E ($77\,\mathrm{K}$)		α (10^{-3})	
	Measure	Reference	Measure	Reference	Measure	Reference
Aluminium	73 ± 1	70	78 ± 3	77	3.9 ± 0.3	3.9
Copper	125 ± 1	120	128 ± 6	138	3.2 ± 0.3	3.0
Invar	151 ± 1	150	129 ± 9	150	0.4 ± 0.1	0.5
Steel	200 ± 8	195	206 ± 15	209		

Thermal contraction coefficient measurements have been calibrated by measuring stress losses of three different materials (aluminium 6082 T6, invar and copper) in our mould, shown in Fig A.1. In Table A.1 we show the measurement results, that are in good agreement with the literature.
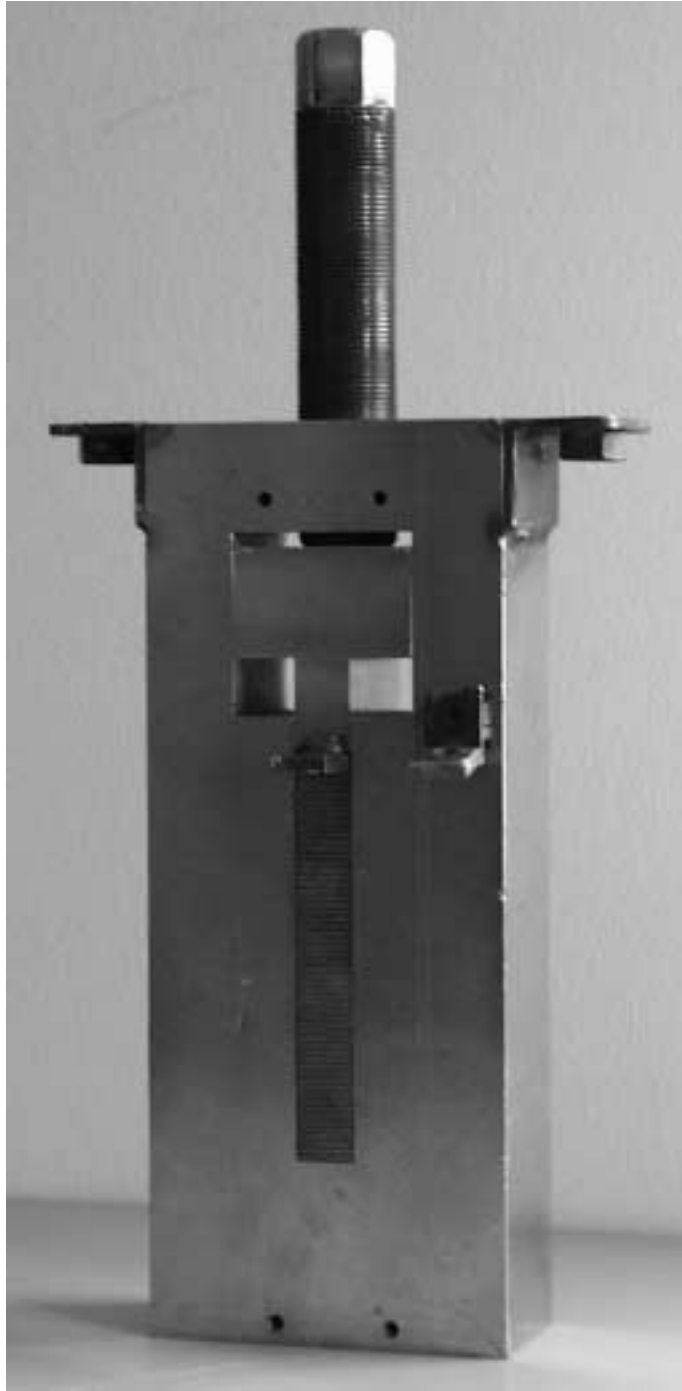
Figure A.1: The mould for the evaluation of the thermal contraction coefficient.

Appendix B

Dependences of coil integrated thermal contraction

We analysed the effect of the stress chosen to define the unloaded stack height on the strains and on the integrated thermal contraction coefficient measured with stress loss method. We define l_{w0} and l_{c0} as the height of the stack at three different cut-stresses $0.4\,\mathrm{MPa}$, $1\,\mathrm{MPa}$ and $3\,\mathrm{MPa}$. We then evaluate the strain of the stack at $293\,\mathrm{K}$ and at $77\,\mathrm{K}$ on the loading curve, and we compute the thermal contraction. In Tab. B.1 we can see that strains strongly depend on the cut-stress (up to a factor two). Integral thermal contraction also shows significant variations (about $15\,\%$ with respect to the analysed range of cut-stresses).

Table B.1: Strains (in 10^{-3} units) and integral thermal contraction coefficient α (in 10^{-3} units) of the inner layer evaluated from 3 different cut-stresses (MPa).

		Inner layer			
σ_w	σ_c	cut-stress	ϵ_w	ϵ_{cl}	α_l
80	45	0.4	35.9	26.0	12.0
80	45	1.0	28.9	17.7	13.2
80	45	3.0	23.3	11.6	14.0

Then, we study the impact of the stress-strain modeling of the stack on the integral thermal contraction. We consider a linear behaviour and we compute the strain before and after the cool-down assuming a constant elastic modulus. We assume that the strain at $75\,\mathrm{MPa}$ at room temperature is given by stress divided by the elastic modulus of the unloaded curve ($12900\,\mathrm{MPa}$ for the inner layer). We performed the same computation at cryogenic temperature considering the elastic modulus of the unloading curve at $45\,\mathrm{MPa}$ ($9400\,\mathrm{MPa}$ for the inner layer) and we compare the results with the approach followed in the main text. The aim of this

analysis is to evaluate what happens if we assume a linear stress-strain relation instead of the non-linear one. One finds a very large difference between the two values (see Tab. B.2).

Table B.2: Strains (in 10^{-3} units) and integral thermal contraction coefficient α (in 10^{-3} units) of the inner layer evaluated with different $\sigma - \epsilon$ relation (MPa).

σ_w	σ_c	$\sigma - \epsilon$ relation	ϵ_w	ϵ_{cu}	α_u
		Inner layer			
80	45	non-linear	35.9	27.0	10.9
80	45	linear	6.2	4.8	3.4

Appendix C

Measurements of pre-stress

We give here the pre-stress measured[1] on single aperture 1 m long dipoles prototypes MBSMS (see Tab. C.1), on double aperture 1 m long dipoles MBSMT prototypes (see Tab. C.2) and on long prototypes MBP2 (see Tab. C.3). Pre-stress measurements have been taken during collaring (peak stress), after collaring, before yoking, after yoking and after cool-down.

Table C.1: Pre-stress (MPa) measured on single aperture short dipoles (MBSMS).

Magn.	Peak		After coll.		Before yok.		After yok.		1.9 K	
MBSMS	In	Out	In	Out	In	Out	In	Out	In	Out
3v4	170	206	108	130	100	122	109	133	42	60
15v2	98	137	72	97	69	94	77	101	28	47
15v3	86	107	58	63	59	64	66	71	24	26
15v4	119	144	89	99	88	97	93	103	38	43
19v1	98	134	65	80	58	74	66	80	23	30
19v2	98	139	63	79	58	69	64	76	27	35
19v3	92	129	62	78	63	79	72	87	28	32
21v2	104	150	70	94	66	92	74	97	30	37
22v1	90	116	59	67	50	57	62	68	21	23
23v1	93	138	59	82	57	81	66	86	18	31
23v3	91	143	56	86	51	83	60	89	14	32
23v4	116	153	74	89	70	85	78	91	28	36
19v4	-	-	-	-	54	73	62	80	26	30

---

[1]Pre-stress measurements performed by I. Vanenkov (LHC-MMS Group, CERN).

Table C.2: Pre-stress (MPa) measured on double aperture short dipoles (MBSMT), aperture 1 and 2.

Magn.		Peak		After coll.		Before yok.		After yok.		1.9 K	
MBSMT	Apert.	In	Out	In	Out	In	Out	In	Out	In	Out
4v1	1	81	121	56	86	56	85	61	90	17	33
4v1	2	81	118	57	82	56	80	60	85	18	30
4v2	1	79	117	54	82	49	78	54	83	17	31
4v2	2	81	115	56	79	51	74	56	80	19	30
5v1	1	83	101	57	69	50	60	52	62	17	22
5v1	2	81	105	56	73	50	64	52	66	16	25
6v1	1	76	126	50	93	46	87	53	97	14	36
6v1	2	71	129	45	92	42	87	48	97	11	36
7v1	1	85	124	59	87	57	86	63	93	21	36
7v1	2	87	115	62	81	60	79	66	86	22	29
7v2	1	85	123	60	86	55	83	61	89	19	33
7v2	2	85	114	60	80	57	77	60	83	20	30
8v1	1	88	123	62	89	47	77	53	82	18	32
8v1	2	80	120	54	83	39	70	46	76	14	31

Table C.3: Pre-stress (MPa) during collaring measured on long prototypes (MBP2).

Magn.	Peak		After coll.		Before yok.		After yok.		1.9 K	
MBP2	In	Out	In	Out	In	Out	In	Out	In	Out
N2	97	130	63	79	62	77	72	85	26	32
O1	102	125	58	58	51	55	62	62	19	22
O2	112	142	55	64	54	63	65	75	18	22
A1	118	154	62	76	54	57	62	66	-	-
A2	90	115	53	56	51	53	57	60	16	16

Appendix D

Magnetic measurements at 293 K: collared coil

In Tab. D.1 and Tab. D.3 we give the magnetic measurements[1] carried out at 300 K on the collared coils of the five prototypes made with stainless steel collars and of the first 15 pre-series magnets.

Averages along the straight part (first and last measurements are discarded because of end effects, 18 positions along the axis are kept) are given in the usual units of 10^{-4} at a reference radius of 17 mm. For the prototypes the average over the two apertures is presented. Magnetic measurements are taken at low current (12 A).

We give also the variation of the shim thickness with respect to nominal values (0.4 mm in the inner layer and 1 mm in the outer layer for the prototypes and 0.2 mm in the inner layer and 0.8 mm in the outer layer for the pre-series dipoles).

In Tab. D.2 and Tab. D.4 we give the same magnetic measurements after subtracting the effect of non-nominal shims, according to Tab. 7.3.

---

[1]Magnetic measurements performed by O. Pagano and V. Remondino (LHC-MMS Group, CERN)

Table D.1: Field-shape harmonics measured at room temperature of the five prototypes, collared coils, straight part, in units 10^{-4} of dipole field at 17 mm and differences of shim thickness (mm) with respect to nominal values.

Magn.	Harmonics			Δshim	
	b_3	b_5	b_7	In	Out
MBP2 N2	+3.04	−0.09	+0.81	+0.03	+0.12
MBP2 O1	−2.06	+0.32	+0.68	−0.08	−0.02
MBP2 O2	+5.83	+0.63	+0.99	+0.07	+0.09
MBP2 A2	−1.81	+1.30	+0.54	−0.20	+0.00
MBP2 A1	+3.27	+0.90	+0.62	−0.05	+0.16

Table D.2: Field-shape harmonics measured at room temperature of the five prototypes, collared coils, straight part, in units 10^{-4} of dipole field at 17 mm (effect of non-nominal shims subtracted).

Magn.	Harmonics			Δshim	
	b_3	b_5	b_7	In	Out
MBP2 N2	+0.44	+0.13	+0.79	0.00	0.00
MBP2 O1	+0.02	−0.02	+0.80	0.00	0.00
MBP2 O2	+2.82	+0.98	+0.91	0.00	0.00
MBP2 A2	+2.55	+0.50	+0.84	0.00	0.00
MBP2 A1	+1.61	+0.84	+0.73	0.00	0.00

Table D.3: Field-shape harmonics measured at room temperature of the pre-series dipoles, collared coils, straight part, in units 10^{-4} of dipole field at $17\,\text{mm}$ and differences of shim thickness (mm) with respect to nominal values.

Magn.	Ap.	Harmonics			Δshim	
		b_3	b_5	b_7	In	Out
HCMBB A001-01000001	1	+8.27	−0.84	+1.08	+0.35	+0.27
HCMBB A001-01000001	2	+8.87	−0.99	+1.13	+0.35	+0.27
HCMBB A001-01000002	1	+5.92	−0.10	+0.94	+0.25	+0.10
HCMBB A001-01000002	2	+5.61	−0.09	+0.94	+0.22	+0.15
HCMBB A001-01000003	1	+4.59	+0.31	+0.87	+0.15	+0.15
HCMBB A001-01000003	2	+4.35	+0.84	+0.86	+0.15	+0.15
HCMBB A001-01000004	1	+0.52	+0.78	+0.80	+0.00	+0.00
HCMBB A001-01000004	2	+0.53	+0.90	+0.70	+0.00	+0.00
HCMBB A001-01000005	1	+1.12	+1.12	+0.74	+0.00	+0.00
HCMBB A001-01000005	2	−0.72	+1.31	+0.76	+0.00	+0.00
HCMBB A001-01000006	1	+0.15	+2.29	+0.85	+0.00	+0.00
HCMBB A001-01000006	2	+0.08	+2.01	+0.88	+0.00	+0.00
HCMBB A001-01000007	1	+4.19	+1.58	+0.74	+0.00	+0.00
HCMBB A001-01000007	2	+3.84	+1.78	+0.77	+0.00	+0.00
HCMBB A001-02000001	1	+0.29	+1.46	+0.74	+0.05	+0.10
HCMBB A001-02000001	2	−0.53	+1.06	+0.62	+0.05	+0.10
HCMBB A001-02000002	1	−0.77	+1.68	+0.57	+0.00	+0.00
HCMBB A001-02000002	2	−0.57	+1.72	+0.57	+0.00	+0.00
HCMBB A001-02000003	1	+1.05	+0.95	+0.59	+0.00	+0.00
HCMBB A001-02000003	2	+1.33	+0.94	+0.61	+0.00	+0.00
HCMBB A001-02000005	1	+0.98	+1.33	+0.37	+0.00	+0.00
HCMBB A001-02000005	2	+1.28	+1.39	+0.47	+0.00	+0.00
HCMBB A001-03000001	1	−0.77	+0.75	+0.54	−0.06	+0.17
HCMBB A001-03000001	2	−1.56	+0.72	+0.64	−0.06	+0.17
HCMBB A001-03000002	1	+1.51	+0.90	+0.56	−0.05	+0.17
HCMBB A001-03000002	2	+1.58	+1.03	+0.57	−0.05	+0.17
HCMBB A001-03000003	1	+2.89	+0.95	+0.58	−0.05	+0.20
HCMBB A001-03000003	2	+3.12	+0.92	+0.57	−0.05	+0.20
HCMBB A001-03000004	1	+2.73	+0.63	+0.62	+0.00	+0.15
HCMBB A001-03000004	2	+3.10	+0.51	+0.57	+0.00	+0.15

Table D.4: Field-shape harmonics measured at room temperature of the pre-series dipole, collared coils, straight part, in units 10^{-4} of dipole field at $17\,\mathrm{mm}$ (effect of non-nominal shims subtracted).

| Magn. | Ap. | Harmonics | | | Δshim | |
		b_3	b_5	b_7	In	Out
HCMBB A001-01000001	1	-3.73	$+0.78$	$+0.61$	0.00	0.00
HCMBB A001-01000001	2	-3.14	$+0.62$	$+0.66$	0.00	0.00
HCMBB A001-01000002	1	-1.07	$+0.97$	$+0.59$	0.00	0.00
HCMBB A001-01000002	2	-1.69	$+0.92$	$+0.64$	0.00	0.00
HCMBB A001-01000003	1	-1.11	$+1.03$	$+0.67$	0.00	0.00
HCMBB A001-01000003	2	-1.35	$+1.56$	$+0.67$	0.00	0.00
HCMBB A001-01000004	1	$+0.52$	$+0.78$	$+0.80$	0.00	0.00
HCMBB A001-01000004	2	$+0.53$	$+0.90$	$+0.70$	0.00	0.00
HCMBB A001-01000005	1	$+1.12$	$+1.12$	$+0.74$	0.00	0.00
HCMBB A001-01000005	2	-0.72	$+1.31$	$+0.76$	0.00	0.00
HCMBB A001-01000006	1	$+0.15$	$+2.29$	$+0.85$	0.00	0.00
HCMBB A001-01000006	2	$+0.08$	$+2.01$	$+0.88$	0.00	0.00
HCMBB A001-01000007	1	$+4.19$	$+1.58$	$+0.74$	0.00	0.00
HCMBB A001-01000007	2	$+3.84$	$+1.78$	$+0.77$	0.00	0.00
HCMBB A001-02000001	1	-2.42	$+1.74$	$+0.69$	0.00	0.00
HCMBB A001-02000001	2	-3.24	$+1.34$	$+0.56$	0.00	0.00
HCMBB A001-02000002	1	-0.77	$+1.68$	$+0.57$	0.00	0.00
HCMBB A001-02000002	2	-0.57	$+1.72$	$+0.57$	0.00	0.00
HCMBB A001-02000003	1	$+1.05$	$+0.95$	$+0.59$	0.00	0.00
HCMBB A001-02000003	2	$+1.33$	$+0.94$	$+0.61$	0.00	0.00
HCMBB A001-02000005	1	$+0.98$	$+1.33$	$+0.37$	0.00	0.00
HCMBB A001-02000005	2	$+1.28$	$+1.39$	$+0.47$	0.00	0.00
HCMBB A001-03000001	1	-2.22	$+0.64$	$+0.66$	0.00	0.00
HCMBB A001-03000001	2	-3.01	$+0.62$	$+0.76$	0.00	0.00
HCMBB A001-03000002	1	-0.15	$+0.83$	$+0.67$	0.00	0.00
HCMBB A001-03000002	2	-0.08	$+0.96$	$+0.68$	0.00	0.00
HCMBB A001-03000003	1	$+0.74$	$+0.91$	$+0.70$	0.00	0.00
HCMBB A001-03000003	2	$+0.97$	$+0.88$	$+0.69$	0.00	0.00
HCMBB A001-03000004	1	$+0.30$	$+0.75$	$+0.65$	0.00	0.00
HCMBB A001-03000004	2	$+0.67$	$+0.63$	$+0.60$	0.00	0.00

Appendix E

Magnetic measurements at 293 K: cold mass

Table E.1: Field-shape harmonics measured at room temperature of the pre-series dipoles, assembled cold mass, straight part, in units 10^{-4} of dipole field at $17\,\mathrm{mm}$ and differences of shim thickness (mm).

Magn.	Ap.	Harmonics			Δshim	
		b_3	b_5	b_7	In	Out
HCMBB A001-01000001	1	+11.47	−0.67	+0.90	+0.35	+0.27
HCMBB A001-01000001	2	+12.09	−0.79	+0.94	+0.35	+0.27
HCMBB A001-01000002	1	+9.75	−0.05	+0.77	+0.25	+0.10
HCMBB A001-01000002	2	+8.78	−0.02	+0.69	+0.22	+0.15
HCMBB A001-01000003	1	+8.87	+0.30	+0.71	+0.15	+0.15
HCMBB A001-01000003	2	+8.58	+0.75	+0.71	+0.15	+0.15
HCMBB A001-02000001	1	+4.57	+1.32	+0.60	+0.05	+0.10
HCMBB A001-02000001	2	+3.93	+0.99	+0.51	+0.05	+0.10
HCMBB A001-03000001	1	+3.74	+0.67	+0.44	−0.06	+0.17
HCMBB A001-03000001	2	+3.05	+0.66	+0.53	−0.06	+0.17
HCMBB A001-03000002	1	+5.87	+0.78	+0.47	−0.05	+0.17
HCMBB A001-03000002	2	+5.91	+0.89	+0.48	−0.05	+0.17

In Tab. E.1 we give the magnetic measurements[1] carried out at $300\,\mathrm{K}$ on the cold mass of 5 pre-series magnets. Averages along the straight part (first and last measurements are discarded because of end effects, 18 positions along the axis are

---

[1] Magnetic measurements performed by O. Pagano and V. Remondino (LHC-MMS Group, CERN)

kept) are given in the usual units of 10^{-4} at a reference radius of $17\,\mathrm{mm}$. Magnetic measurements are taken at low current ($12\,\mathrm{A}$).

We give also the variation of the shim thickness with respect to nominal values (and $0.2\,\mathrm{mm}$ in the inner layer and $0.8\,\mathrm{mm}$ in the outer layer for the pre-series dipoles).

In Tab. E.2 we give the same magnetic measurements after subtracting the effect of non-nominal shims, according to Tab. 7.9.

Table E.2: Field-shape harmonics measured at room temperature of the pre-series dipoles, assembled cold mass, straight part, in units 10^{-4} of dipole field at $17\,\mathrm{mm}$ (effect of non-nominal shims subtracted).

Magn.	Ap.	Harmonics			Δshim	
		b_3	b_5	b_7	In	Out
HCMBB A001-01000001	1	+1.45	+0.67	+0.49	0.00	0.00
HCMBB A001-01000001	2	+2.07	+0.55	+0.53	0.00	0.00
HCMBB A001-01000002	1	+3.92	+0.83	+0.47	0.00	0.00
HCMBB A001-01000002	2	+2.69	+0.82	+0.43	0.00	0.00
HCMBB A001-01000003	1	+4.11	+0.90	+0.54	0.00	0.00
HCMBB A001-01000003	2	+3.82	+1.35	+0.54	0.00	0.00
HCMBB A001-02000001	1	+2.31	+1.55	+0.55	0.00	0.00
HCMBB A001-02000001	2	+1.67	+1.23	+0.46	0.00	0.00
HCMBB A001-03000001	1	+2.54	+0.59	+0.55	0.00	0.00
HCMBB A001-03000001	2	+1.84	+0.58	+0.64	0.00	0.00
HCMBB A001-03000002	1	+4.49	+0.74	+0.57	0.00	0.00
HCMBB A001-03000002	2	+4.53	+0.84	+0.57	0.00	0.00

Appendix F

Magnetic measurements at 1.9 K

In Tab. F.1 we give the magnetic measurements[1] carried out at 1.9 K on the cold mass of 5 pre-series magnets.

Averages along the straight part (first and last measurements are discarded because of end effects, 18 positions along the axis are kept) are given in the usual units of 10^{-4} at a reference radius of 17 mm. Magnetic measurements are taken at a current of 5000 A.

Table F.1: Field-shape harmonics measured at 1.9 K of the pre-series dipoles, assembled cold mass, straight part, in units 10^{-4} of dipole field at 17 mm and differences of shim thickness (mm) with respect to nominal values.

Magn.	Ap.	Harmonics			Δshim	
		b_3	b_5	b_7	In	Out
HCMBB A001-01000001	1	+11.46	−0.84	+0.89	+0.35	+0.27
HCMBB A001-01000001	2	+12.11	−0.91	+0.93	+0.35	+0.27
HCMBB A001-01000002	1	+9.28	−0.19	+0.78	+0.25	+0.10
HCMBB A001-01000002	2	+9.15	−0.15	+0.80	+0.22	+0.15
HCMBB A001-02000001	1	+5.05	+0.83	+0.67	+0.05	+0.10
HCMBB A001-02000001	2	+4.28	+0.52	+0.57	+0.05	+0.10
HCMBB A001-03000001	1	+3.32	+0.38	+0.46	−0.06	+0.17
HCMBB A001-03000001	2	+2.61	+0.39	+0.56	−0.06	+0.17
HCMBB A001-03000002	1	+4.78	+0.74	+0.49	−0.05	+0.17
HCMBB A001-03000002	2	+4.75	+0.83	+0.50	−0.05	+0.17

We give also the variation of the shim thickness with respect to nominal values (0.2 mm in the inner layer and 0.8 mm in the outer layer for the pre-series dipoles).

---

[1]Magnetic measurements performed by S. Sanfilippo (LHC-MTA Group, CERN)

In Tab. F.2 we give the same magnetic measurements after subtracting the effect of non-nominal shims, according to Tab. 8.1.

Table F.2: Field-shape harmonics measured at 1.9 K of the pre-series dipoles, assembled cold mass, straight part, in units 10^{-4} of dipole field at 17 mm (effect of non-nominal shims subtracted).

Magn.	Ap.	Harmonics			Δshim	
		b_3	b_5	b_7	In	Out
HCMBB A001-01000001	1	+1.45	+0.50	+0.48	0.00	0.00
HCMBB A001-01000001	2	+2.09	+0.43	+0.52	0.00	0.00
HCMBB A001-01000002	1	+3.45	+0.69	+0.48	0.00	0.00
HCMBB A001-01000002	2	+3.06	+0.69	+0.53	0.00	0.00
HCMBB A001-02000001	1	+2.79	+1.07	+0.62	0.00	0.00
HCMBB A001-02000001	2	+2.02	+0.75	+0.52	0.00	0.00
HCMBB A001-03000001	1	+2.12	+0.30	+0.57	0.00	0.00
HCMBB A001-03000001	2	+1.40	+0.31	+0.66	0.00	0.00
HCMBB A001-03000002	1	+3.39	+0.69	+0.58	0.00	0.00
HCMBB A001-03000002	2	+3.37	+0.78	+0.59	0.00	0.00

Bibliography

[1] "Superconducting accelerator magnet", CD-ROM Tutorial, published by MJB Plus, Inc, 1998. For information see www.mjb-plus.com.

[2] H. Hirabayashi, et al., "A design proposal for high field dipole magnet", *KEK-81-1*, June 1981.

[3] "The Large Hadron Collider, Conceptual design", *CERN/AC/95-05*, October 1995.

[4] R. Gupta, "A common coil design for high-field 2-in-1 accelerator magnets", 1997 Particle Accelerator Conference, Vancouver, Canada.

[5] P. McIntyre, W. Shen, R. Scanlan, "16-Tesla block coil dipole for future Hadron Colliders", 1995 Particle Accelerator Conference, Dallas, USA.

[6] ANSYS User's Manual for Revision 5.5, Swanson Analysis System Inc., Houston.

[7] S. Russenschuck, *CERN-99-01*, 1999.

[8] F.W. Markley, J.S. Kerby, B. Sizemore, C. Khoun, T. King, "Investigation of the elastic modulus of SSC coils", *Supercollider 3*, Plenum Press, pp. 165-173, New York, 1991.

[9] N.I. Andreev, S.S. Kozub, V.V. Sytnik, A.T. Veshchikov, A.V. Zlobin, "Mechanical properties of the coil for the UNK superconducting magnets", *IHEP 93-61*, Protvino, 1993.

[10] Y. Chen, R. Jayakumar, K. Yu, "Experimental Young modulus calculations", *Supercollider 5*, Plenum Press, New York, 1994.

[11] R.B. Meuser, Shlomo Caspi, W.S. Gilbert, "Measured mechanical properties of superconducting coil materials and their influence on coil pre-stress", *IEEE Trans. Magn.*, vol. 17, no. 5, September 1981.

[12] M. Reytier, A. Devred, M. Durante, C. Gourdin, P. Vedrine, "Characterisation of the thermo-mechanical behaviour of insulated cable stacks representative of accelerator magnet coils", *DAPNIA-STCM-00-23*, December 2000.

[13] C. Goodzeit, "Thermal contraction measurements", *BNL-MDN-445-15*, July 1992.

[14] V.N. Gladky, S.S. Kozub, A.T. Veshchikov, U. Escher, "Thermal contraction of superconducting magnet materials", *Cryogenics*, vol. 35, no. 1, pp. 67-69, 1995.

[15] P. Vedrine, B. Gallet, C. Nouvel, "Measurement of thermo-mechanical properties of NiTi windings for accelerator magnet", *IEEE Trans. Appl. Superconduct.*, vol. 9, no. 2, pp. 236-239, June 1999.

[16] A. Devred, et al., "About the mechanics of SSC dipole magnet prototypes", *AIP Conf. Proc.*, 249, pp. 1309-1374.

[17] M. Bona, D. Perini, "Finite-element structural analysis of the 10 m long dipole prototype magnet for the LHC", *IEEE Trans. Magn.*, vol. 28, no. 1, pp. 358-361, 1992.

[18] M. Bajko, P. Fessia, D. Perini, "FEM Computations Concerning the Effect of Friction in Two LHC Main Dipole Structures", *IEEE Trans. Appl. Superconduct.*, vol 10, no. 1, pp.81-84, 2000.

[19] P. Ferracin, W. Scandale, E. Todesco, P. Tropea, I. Vanenkov, "Modeling thermo-mechanical structure of the LHC main dipole and influence on field quality", in *Seventh European Particle Accelerator Conference*, C. Petit-Jean Genaz, Ed. New York: IoP, 2000, pp. 330-2.

[20] Z. Ang, et al, "Coil Size and Geometric Field Quality in Short Model Dipoles for LHC", *IEEE Trans. Appl. Supercond.*, vol 10, 53-56, 1999.

[21] H. Wiedemann, "Particle Accelerator Physics I", Springer.

[22] K.-H. Mess, P. Schmuser, S. Wolff, "Superconducting Accelerator Magnets", World Scientific, 1996.

[23] D. Leroy, G. de Rijk, "The iron yoke and the quality of the magnetic field in twin-aperture LHC dipoles", *CERN-SPS-89-37*, also in *LHC-note-106*, 1989.

[24] P. Thompson, *et al.*, "Mechanical properties of Isabelle superconducting coil", *IEEE Trans. Nucl. Sci.*, vol. NS-28, no. 3, pp. 3303-3305, June 1981.

[25] E. Acerbi, L. Rossi, "Mechanical, thermal and electrical measurements on material and components of the main coils of the Milan superconducting cyclotron", *INFN/TC-88/16*, April 1988.

[26] F.W. Markley, J.S. Kerby, "Investigation of the mechanical properties of superconducting coils", *Supercollider 2*, Plenum Press, pp. 753-763, New York, 1990.

[27] I.R. Dixon, R.P. Walsh, W.D. Markiewicz, C.A. Swenson, "Mechanical properties of epoxy impregnated superconducting solenoids", *IEEE Trans. Magn.*, vol. 32, no. 4, July 1996.

[28] T. Saito, et al., "Investigation of the mechanical and electrical properties of superconducting coils", *Supercollider 5*, Plenum Press, pp. 225-228, New York, 1994.

[29] F. Zerobin, M. Painer, S. Eichberger, "Size and stiffness measurements on 9.5 m long LHC dipole coils", *IEEE Trans. Magn.*, vol. 30, no. 4, July 1994.

[30] R.E. Sims, "Tooling and process parameters improvements leading to improved dimensional control of the cured SSC dipole coils", *Supercollider 3*, Plenum Press, pp. 57-74, New York, 1991.

[31] C.A. Swenson, I.R. Dixon, W.D. Markiewicz, "Measurements of thermal contraction properties for NbTi and Nb$_3$Sn composites", *IEEE Trans. Appl. Superconduct.*, vol. 7, no. 2, pp. 408-411, June 1997.

[32] K.P. Chow, G.A. Millos, "Measurements of modulus of elasticity and thermal contraction of epoxy impregnated Niobium-Tin and Niobium-Titanium composites", *IEEE Trans. Appl. Superconduct.*, vol. 9, no. 2, pp. 213-215, June 1999.

[33] K. Couturier, P. Ferracin, W. Scandale, E. Todesco, D. Tommasini, "Thermo-mechanical properties of the coil of the superconducting magnets for the Large Hadron Collider", to be published in *IEEE Trans. Appl. Superconduct.*, 2002.

[34] K. Couturier, P. Ferracin, E. Todesco, D. Tommasini, and W. Scandale, "Elastic modulus measurements of the LHC dipole superconducting coil at 300 K and at 77 K", to be published in *Adv. Cryo. Eng.* 47-48, 2002, also in *CERN-LHC-Project-Report* 514, 2001.

[35] P. Ferracin, E. Todesco, D. Tommasini, and W. Scandale, "Thermal contraction measurements of the superconducting coil of the main magnets for the Large Hadron Collider", to be published in *Adv. Cryo. Eng.* 47-48, 2002, also in *CERN-LHC-Project-Report* 513, 2001.

[36] K. Artoos, et al., "Design, manufacturing status, first results of the LHC main dipole final prototypes and step towards series manufacture", *IEEE Trans. Appl. Superconduct.*, vol. 10, no. 1, pp. 98-102, December 1999.

[37] C. Meuris, B. Baudouy, D. Leroy, B. Szeless, "Heat transfer in electrical insulation of LHC cables cooled with superfluid helium", *Cryogenics*, vol. 39, pp. 921-931, November 1999.

[38] G. Spigo, Private communications.

[39] A. Devred, Private communications.

[40] Y.S. Touloukian, R.K. Kirby, R.E. Taylor, P.D. Desai, "THERMAL EXPAN-SION. Metallic Elementsand alloys", *Thermophysical properties of matter*, vol. 12, IFI/PLENUM, New York-Washington.

[41] N. Siegel, D. Tommasini, Y. Vanenkov, "Design and use of capacitive force transducers for superconducting magnet models for the LHC", *CERN-LHC-Project-Report-173*, May 1998.

[42] N. Andreev, et al., "Mechanical behaviour of the short models of LHC main dipole magnets", *CERN-LHC-Project-Report-179*, May 1998.

[43] D.R. Chichili, T.T Arkan, J.P. Ozelis, I. Terechkine, "Investigation of cable insulation and thermo-mechanical properties of epoxy impregnated Nb_3Sn composites", *IEEE Trans. Appl. Superconduct.*, vol. 10, no. 1, March 2000.

[44] D.R. Chichili, T.T Arkan, I. Terechkine, "Investigation of cable insulation and mechanical properties of Nb_3Sn composites", *FERMILAB-conf-99/052*, April 1999.

[45] P. Ferracin, P. Rastogi, W. Scandale, E. Todesco, P. Tropea, "Speckle interfer-ometry measurements of the conductor displacements in the CERN-LHC main dipole", to be published in *IEEE Trans. Appl. Superconduct*, 2002.

[46] P. Ferracin, P. Rastogi, W. Scandale, E. Todesco, P. Tropea, "Analysis of con-ductor displacements in the coil of the LHC main dipole by Speckle interferom-etry", to be published in *IEEE Trans. Appl. Superconduct*, 2002.

[47] M.S. Chapman, "A Finite Element analysis of an SSC dipole magnet (NC-9 cross-section)", *Supercollider 1*, Plenum Press, pp. 659-668, New York, 1989.

[48] D. Dell'Orco, "Finite Element analysis of the QC quadrupole for the Supercon-ducting Supercollider", *LBL-29600*, October 1989.

[49] M. Zaslawsky, "Nonlinear Finite Element analysis of the SSC superconductivity magnet: including the effects of cooldown, operation, quench, preassembly loads and Lorentz forces", *SSC-126*, April 1987.

[50] P. Ferracin, "Comportamento strutturale e qualita' di campo delle bobine dei dipole per LHC: studio e confronto con i risultati sperimentali", Tesi di Laurea, Politecnico di Torino, 1998.

[51] P. Tropea, "The CERN-LHC superconducting dipole: assembly and cool-down deformation influence on the magnetic field quality", Tesi di Laurea, Facolta' di Ingegneria, Universita' degli Studi di Genova, 2000.

[52] A. Devred, T. Ogitsu, K. Tsuchiya, "Investigation of wire motion in superconducting magnets", *IEEE Trans. Magn.*, vol. 27, pp. 2132-2135, 1991.

[53] D. Bein, J. Zbasnik, J. Bolger, B. Firey, B. Rice, B. Crane, G. Rabaey, J. Wesick and L. Morgan, "Utilization of gamma ray inspection system for tomographic imaging and dimensional analysis of complete model magnet cold masses and collared coil sections", *Supercollider 4*, Plenum Press, pp. 225-233, New York, 1992

[54] P. Ferracin, E. Todesco, P. Tropea, "Modeling of the nonlinear elasticity curve of the LHC dipole coils with the finite elements", *CERN LHC-MMS Internal Note* 2000-17 (2000).

[55] P. K. Rastogi, *Trends in optical non-destructive testing and inspection*, Amsterdam, Elsevier, 2000, pp. 171-178.

[56] P. K. Rastogi, *Optical measurements techniques and applications*, London, Artech House, 1997, pp. 111-150.

[57] P. Ferracin, E. Todesco, D. Tommasini, W. Scandale, "Azimuthal coil length and field quality in the main LHC dipoles", to be published in *Phys. Rev. STAB.*.

[58] S. Timoshenko, *Scienze delle costruzioni*, VIGLONGO, vol. 2, pp. 77-78, 1989.

[59] D. Tommasini, Private communications.

[60] D. Perini, Private communications.

[61] P. Ferracin, W. Scandale, E. Todesco, R. Wolf, "Modeling of random geometric errors in superconducting magnets with applications to the Large Hadron Collider", *Phys. Rev. ST-AB* 3 (2000) 122403, also in *CERN-LHC-Project-Report* 460, 2000.

[62] P. Ferracin, W. Scandale, E. Todesco, D. Tommasini, "Thermo-mechanical properties and azimuthal prestress loss of the LHC dipole coils" *CERN LHC-MMS Internal Note* 2000-14, (2000).

[63] E. Todesco, Private communications.

[64] M. Modena, et al., "Final Prototypes, First Pre-series Units and Steps Towards Series Production of the LHC Main Dipoles", in Particle Accelerator Conference, Chicago, IL, USA, 18-22 Jun 2001, also in *CERN-LHC-Project-Report* 487, 6 Aug 2001.

[65] W. Scandale, E. Todesco, P. Tropea, "Influence of mechanical tolerances on field quality in the LHC main dipoles", *IEEE Trans. Appl. Supercond.*, Vol. 10, pag. 73-76, 2000.

[66] P. Fessia, et al. "Selection of the Cross-Section Design for the LHC Main Dipole", *IEEE Trans. Appl. Superconduct.*, vol. 10, no. 1, pp. 65-68, 2000.

[67] S. Readelli, "Analysis of the magnetic field perturbations in dipoles and quadrupoles of the Large Hadron Collider (LHC)", Tesi di Laurea, Facolta' di Scienze Matematiche, Fisiche e Naturali, Universita' degli Studi di Milano, 2000.

[68] S. Fartoukh and O. Bruning, "Field quality specification for the LHC Main Dipole magnets", *CERN LHC Project Report* 501, October 2001.

[69] P. Ferracin, O. Pagano, S. Redaelli, W. Scandale, E. Todesco, "Control of field quality for the production of the main LHC dipoles", *CERN LHC Project Report* 467, 2001.

[70] P. Ferracin, W. Scandale, E. Todesco, P. Tropea, "A method to evaluate the field-shape multipoles induced by coil deformation" in: *1999 Particle Accelerator Conference*, edited by A. Luccio and W. MacKay (IEEE, New York, 1999) 3206-8, also in *CERN LHC Project Report* **287** (1999).

[71] C. Völlinger, "Estimate of saturation induced multipole errors in the LHC main dipoles", *CERN-99-01*, 1999.

[72] P. Ferracin, W. Scandale, E. Todesco, D. Tommasini, "Modeling of the coil prestress loss during cool-down in the main dipoles of the Large Hadron Collider", to be published in *IEEE Trans. Appl. Superconduct*, 2002.

[73] P. Ferracin, O. Pagano, V. Remondino, W. Scandale, E. Todesco, D. Tommasini, "Impact of coil deformations on field quality in the Large Hadron Collider main dipole", to be published in *IEEE Trans. Appl. Superconduct*, 2002.